IS-T-361

AMES LABORATORY

Iowa State University

Ames, Iowa

AEC Contract No. W-7405-eng-82

ELECTROLYTIC BEHAVIOR OF YTTRIA AND YTTRIA STABILIZED HAFNIA

by

Jon David Schieltz

Ph. D. Thesis, May 1970

LEGAL NOTICE

This report was prepared as an account of Government sponsored work. Neither the United States, nor the Commission, nor any person acting on behalf of the Commission:

A. Makes any warranty or representation, expressed or implied, with respect to the accuracy, completeness, or usefulness of the information contained in this report, or that the use of any information, apparatus, method, or process disclosed in this report may not infringe privately owned rights; or

B. Assumes any liabilities with respect to the use of, or for damages resulting from the use of any information, apparatus, method, or process disclosed in this report.

As used in the above, "person acting on behalf of the Commission" includes any employee or contractor of the Commission, or employee of such contractor, to the extent that such employee or contractor of the Commission, or employee of such contractor prepares, disseminates, or provides access to, any information pursuant to his employment or contract with the Commission, or his employment with such contractor.

fcg

DISCLAIMER

ELECTROLYTIC BEHAVIOR OF YTTRIA AND YTTRIA STABILIZED HAFNIA

by

Jon David Schieltz

An Abstract of

A Dissertation Submitted to the

Graduate Faculty in Partial Fulfillment of

The Requirements for the Degree of

DOCTOR OF PHILOSOPHY

Approved:

In Charge of Major Work

Head of Major Department

Dean of Graduate College

Iowa State University
Ames, Iowa

May 1970

ELECTROLYTIC BEHAVIOR OF YTTRIA AND YTTRIA STABILIZED HAFNIA*

Jon David Schieltz

Under the supervision of D. R. Wilder
From the Department of Ceramic Engineering
Iowa State University

The electrolytic behavior of undoped Y_2O_3 and yttria stabilized hafnia solid solutions was investigated. For undoped Y_2O_3 within the temperature range 700 to 1000°C, there was no electrolytic domain ($t_{ion} \geq 0.99$), however a small ionic domain ($t_{ion} \geq 0.5$) does exist and is defined within the following boundaries:

$$\log P_{\oplus} = \frac{11,030}{T(^{o}K)} - 15.84$$

and

$$\log P_{\ominus} = \frac{-35,300}{T(^{o}K)} + 15.59.$$

Undoped Y_2O_3 appears unsuitable as a solid electrolyte based on its small ionic domain and extremely low conductivity. It also exhibits positive hole conduction at high oxygen pressures.

---

*USAEC Report ISU-T-361. This work was performed under contract W-7405-eng-82 with the Atomic Energy Commission.

X-ray analysis and electrical conductivity measurements (800-1000°C) on yttria-hafnia solid solutions between 2 and 20 m/o Y_2O_3 were made to locate the cubic phase and select for further investigations the composition best suited as a solid electrolyte. The phase boundary is located near 7 m/o Y_2O_3. Total conductivities obtained from the cubic phase solid solutions appear to be ionic. The 8 m/o Y_2O_3-HfO_2 composition showed the highest conductivity (log σ_T = -1.57 at 1000°C), and lowest activation energy (16.9 kcal/mole), and was selected as the optimum composition for a solid electrolyte.

Open circuit emf, electrical conductivity, and Wagner d-c polarization measurements between 800 and 1000°C were made to determine the electrolytic domain of the 8 m/o Y_2O_3 composition. The electrolytic domain width at 1000°C extends from log P_{O_2}(atm) = -16.6 to +0.4. The 8 m/o yttria stabilized hafnia composition does appear suitable as a solid electrolyte. Its electrical properties are very similar to those of calcia stabilized zirconia.

ELECTROLYTIC BEHAVIOR OF YTTRIA AND YTTRIA STABILIZED HAFNIA

by

Jon David Schieltz

A Dissertation Submitted to the

Graduate Faculty in Partial Fulfillment of

The Requirements for the Degree of

DOCTOR OF PHILOSOPHY

Major Subject: Ceramic Engineering

Approved:

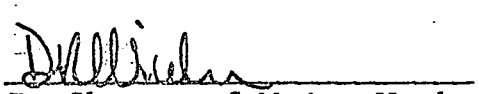

In Charge of Major Work

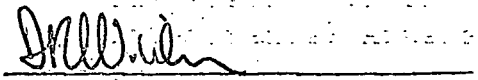

Head of Major Department

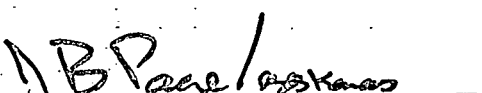

Dean of Graduate College

Iowa State University
Ames, Iowa

1970

TABLE OF CONTENTS

INTRODUCTION

Within the past decade interest has been focused on the electrolytic behavior of certain solid oxide ceramics with the objective of characterizing and utilizing solid oxide electrolytes in potential technological applications.

Nernst (1) carried out the first systematic investigation on the electrical conductivity of oxides in 1899. By applying an electrostatic potential across an oxide sample and investigating the reaction products occurring at the cathode and anode, he concluded that oxygen ions were primarily responsible for the electrical conduction through a zirconia-yttria solid solution.

In 1933 Wagner (2) published a theory pertinent to the application of solid oxide electrolytes when he considered the oxidation mechanisms for a metal covered with an oxide scale surrounded by an oxidizing atmosphere. The dramatic implication of Wagner's scaling rate theory is the existence of a measurable electrostatic potential difference across the scale. As an outcome of his analysis, Wagner derived an expression for the open circuit emf across a metal oxide mixed conductor scale.

Although Nernst had observed ionic conduction in oxide

ceramics and Wagner had derived the necessary equations for the utilization of solid electrolytes, interest in this area layed dormant until 1957 when Kiukkola and Wagner explained (3) and demonstrated (4) the usefulness of solid oxide electrolytes. In their work (4) they determined the standard free energy of formation of several simple binary oxides using calcia stabilized zirconia[1] as the solid electrolyte. Independently Peters and Mann (5) and Peters and Möbius (6) performed similar experiments employing thoria based electrolytes. These two pioneering pieces of work stimulated the revival of interest in high-temperature galvanic cells incorporating solid oxide electrolytes.

Solid state galvanic cells can be conveniently divided into two groups depending upon their particular application:

1. Cells in which information is extracted under open circuit conditions, such as those providing thermodynamic data.
2. Cells which are continuously operated under load conditions producing an external current, such as fuel cells.

---

[1]Calcia stabilized zirconia, yttria stabilized zirconia, yttria doped thoria, and yttria stabilized hafnia will be referred to throughout this thesis as CSZ, YSZ, YDT, and YSH respectively.

The electrolyte requirements for the two applications are not necessarily the same. Providing the electronic conductivity is significantly smaller than the ionic conductivity, the magnitude of the ionic conductivity should not be an important factor for cells of type 1. On the other hand since the electronic conductivity constitutes an oxygen leakage current within the electrolyte, leading to erroneous emf values; it is a critical factor in evaluating electrolytic properties of oxides for cells of type 1. In the case of oxygen fuel cells, they require the electrolyte to possess the highest possible oxygen ion conduction while being capable of withstanding a small electronic conductivity. In general the requirements for a good electrolyte are that it possesses a high ionic conductivity, a small hole or electron conductivity, a relatively stable structure, and an inert behavior toward most electrode materials. As an added convenience, it would be advantageous to control the mobile species. As can be imagined there are few materials that meet these requirements. The most popular electrolytes to date consist of fluorite solid solutions based on zirconia and thoria in which the dopant cations substitute directly on the cation sublattice and induce fully ionized oxygen vacancies as the compensating defect (7,8,9,10,11). The electrical transport is accomplished by the migration of

the mobile oxygen vacancies.

Unlike pure thoria which possesses a cubic structure, zirconia must be doped to completely stabilize the cubic fluorite structure eliminating the destructive monoclinic to tetragonal phase transformation which occurs around 1000°C. This leads to one of the main disadvantages of zirconia based electrolytes, since thermal cycling leads to destabilization (12). Also the zirconia based electrolytes exhibit a higher electronic conductivity (13,14) than thoria based electrolytes. The electrolytic domain of the thoria based electrolytes is located within a lower oxygen partial pressure range than the zirconia based electrolytes (15,16), consequently the application will define constraints on the oxygen partial pressure range which must be met by the proper electrolyte.

The investigation of new possible solid electrolytes has been influenced by the proven behavior of the fluorite solid solutions of zirconia and thoria. Fluorite solid solutions of hafnia appear as a logical choice and some limited studies (17,18,19) have been performed on such systems. The relationship between the cubic fluorite structure and the C-type rare-earth oxide structure (20-23) suggest possible electrolytic behavior for C type rare-earth oxides.

LITERATURE SURVEY

Applications of Solid Oxide Electrolytes

The employment of zirconia and thoria based electrolytes has led to advances in kinetic and thermodynamic experimentation producing impetus for new applications. High temperature galvanic cells involving solid oxide electrolytes have been used to investigate the nature of ionic and electronic defect structures, determine stoichiometry limits, monitor rate processes and oxygen contents of hot gases and liquid metals, and yield thermodynamic information concerning numerous systems. Rather than give an extensive review, only representative examples and unique applications will be covered to furnish the reader with the types of experiments being performed in the field of solid electrochemistry. Excellent reviews pertaining to solid electrolytes and their applications have been published by Alcock (24) and Raleigh (25).

Solid electrolytes possess the property of transporting electrical charge solely by ionic conduction, $t_{ion} \geq 0.99$. Applying this condition to Equation 16A (see Appendix A) a simplified equation now results.

$$E = - \frac{\mu_{O_2}(L) - \mu_{O_2}(0)}{nF} \qquad (1)$$

The number of charge equivalents carried by the mobile ionic species is represented by n. In the case of one mole of diatomic oxygen, n = 4. If all of the active condensed phases of the electrode materials are in their standard states, then Equation 1 can be rewritten as

$$E = - \frac{\Delta G^{o}_{cell}}{nF} . \qquad (2)$$

Where ΔG^{o}_{cell} is the standard Gibbs free energy change for the cell reaction.

Probably the most frequently employed solid oxide galvanic cell is the displacement cell.

A,AO/Electrolyte/B,BO I

The electrodes can be metal-metal oxide compacts (26) which are predominantly electronic conductors and for small currents of limited duration are reversible to oxygen ions. The electrode fixes a specific chemical potential of oxygen at the electrode/electrolyte interface so long as the two phase equilibrium is maintained. Since unlike electrodes fix different oxygen potentials, a diffusional flux of oxygen ions will proceed down the gradient. Since no electrons can flow under open circuit conditions to counter balance the oxygen ion flux, the steady state condition produces a space-charge which prohibits any further diffusion. The potential difference

created by the space-charge is the open-circuit emf.

The displacement cell is the simplest to construct, the electrolyte is sandwiched between two dissimilar metal-metal oxide electrodes and the cell arrangement placed within a high-temperature inert atmosphere. The cell emf is measured with a potentiometer.

The cell reaction for Cell I is

$$A + BO \rightleftarrows AO + B \ . \qquad (3)$$

The open circuit emf corresponds to the standard free energy change for the cell reaction given by Equation 2. The cell reaction is the combination of two formation reactions.

$$BO \rightleftarrows B + \tfrac{1}{2}O_2 \qquad (4)$$

$$A + \tfrac{1}{2}O_2 \rightleftarrows AO \qquad (5)$$

Providing good thermodynamic data is available for one of the above reactions 4 or 5, the electrode involving the thermodynamically defined compound is chosen as the reference electrode. The difference between the cell free energy and the reference electrode free energy is the standard free energy of formation of the desired compound in the opposite electrode, providing the products and reactants are in their standard states. If the left electrode of Cell I is chosen as the reference electrode, then

$$\Delta G^{o}_{BO} = \Delta G^{o}_{AO} - nFE \ . \qquad (6)$$

Displacement cells were used by Kiukkola and Wagner (4) to determine the molar free energy of formation of CoO, NiO, and Cu_2O using CSZ as the electrolyte and an iron-wüstite mixture as the reference electrode based on well established thermodynamic data (27). Rapp (28) measured the free energy of formation of MoO_2 using nickel-nickel oxide and iron-wüstite as the reference electrodes. Thoria based electrolytes have been employed in displacement cells to determine the free energies of formation of MnO (29), Ta_2O_5 (30,31), and various oxides of niobium (30-33).

Electrodes need not be confined to the solid state. The free energy of formation between a liquid metal and its oxide has been measured (34) with respect to Ni-NiO equilibrium. The liquid metal was contained in a crucible made with a CSZ bottom and silica side walls.

Gaseous electrodes have been used as reference electrodes in displacement cells to investigate gas phase equilibrium reactions involving carbon, carbon monoxide, and carbon dioxide (5,6). The employment of gas electrodes does offer a method for the direct determination of the free energy of formation of a compound from a simple formation cell in which

the compound is formed from its elements. Bidwell (35,36) determined the free energy of formation of cuprous oxide using the following cell.

$$Cu,Cu_2O/CSZ/O_2\ (1\ atm) \qquad II$$

The cell reaction is

$$4Cu + O_2 \rightleftarrows 2Cu_2O\ . \qquad (7)$$

The open circuit emf, owing to the simplicity of the cell, corresponds directly to the free energy of formation of cuprous oxide.

Cells using gas electrodes are more difficult to construct, since the electrode compartments must be separated by a gas tight seal to prevent interactions between the electrodes through the gas phase.

The free energies of formation of ternary compounds have been determined from their binary compounds. Schmalzried (37) employed the following cell

$$A,AO/CSZ/AB_2O_4,B_2O_3,A \qquad III$$

with the corresponding cell reaction

$$AO + B_2O_3 \rightleftarrows AB_2O_4 \qquad (8)$$

to study the free energy of formation of various spinels. Using similar cells, Benz and Wagner (38) studied the thermodynamics of calcium silicate compounds at 700°C. Levine and

Kolodney (39) determined the standard free energies of formation of the tantalum silicides from emf measurements on cells with YDT electrolytes. The dissociation pressures of numerous ferrite compositions have been measured by Carter (40) who used wüstite and cobalt oxide as the reference binary compounds and a CSZ electrolyte.

Modification of the non-reference electrode to incorporate a metal alloy in the simple displacement cell allows the determination of metal activities in solid solutions. A typical cell for this type of measurement is

$$\text{A,AO/Electrolyte/ABalloy,AO.} \qquad \text{IV}$$

Generally the activities of A and AO in the reference electrode are taken to be unity providing there is negligible oxygen solubility in the pure metal. The element B should be more noble than A or present at a low enough activity so as not to reduce the compound AO. The cell reaction is simply

$$\text{A(pure)} \rightleftarrows \text{A(alloy)}. \qquad (9)$$

Since AO of essentially the same chemical potential is present on both sides of the cell and the standard state of A(pure) and A(alloy) are identical, Equation 1 is reevaluated to give

$$E = -\frac{RT}{nF} \ln a_{A(alloy)}. \qquad (10)$$

The activity of the other alloying component is usually obtained by integrating the Gibbs-Duhem equation.

Use of this technique has lead to the determination of the activity of iron in the systems iron-gold, iron-palladium, and iron-platinum (41) and the activity of nickel in the nickel-palladium (42) and nickel-copper (26) alloys.

A practical application of the above described cells has been the development of an oxygen pressure gage. Weissbart and Ruka (43) developed such a gage which utilizes the following cell

$$Pt,O_2\ (P^*_{O_2})/CSZ/Pt,O_2\ (P'_{O_2}) \qquad V$$

and permits the measurement of oxygen pressures in a vacuum or gaseous media. The unknown oxygen pressure, P'_{O_2}, can be determined from Equation 11,

$$P'_{O_2} = P^*_{O_2} \exp(-4FE/RT) \qquad (11)$$

where $P^*_{O_2}$ is the oxygen pressure fixed by the reference electrode; the other symbols retain their normal definitions. Schmalzried (44) has described a similar cell using Ni-NiO equilibrium as the reference electrode. At the present time several oxygen pressure gages are commercially available which are based on the relationship expressed by Equation 11.

The obvious extension of the oxygen gage is the measure-

ment of oxygen activities in metal melts. Assuming that oxygen dissolution into the liquid metal obeys Sievert's Law, Equation 11 can be rewritten in terms of the activity of monatomic oxygen in the liquid metal,

$$a_O = K_s P^{*\,\frac{1}{2}}_{O_2} \exp(-2FE/RT) \qquad (12)$$

where $P^*_{O_2}$ again represents the oxygen pressure at the reference electrode. This technique is very appealing to the steel making industry and has prompted considerable research in this area (45-48).

The principles for determining metal activities in solid solutions can be used to determine the phase limits of nonstoichiometric compounds. Aronson and Belle (49) measured the oxygen activity in the UO_{2+x} system for $0 > x > 0.20$ between 1150 and 1350°C, their cell being

$$Fe,FeO/CSZ/UO_{2+x},Pt. \qquad VI$$

The increasing oxygen activity as shown by the decreasing open circuit emf with increasing x indicated a one phase composition within the range of x. Blumenthal *et al.* (33) used a similar cell to determine the compositional phase limits of nonstoichiometric Nb_2O_{5-x}. Markin *et al.* (50) used the cell

$$Ni,NiO/Electrolyte/UO_{2+x},U_4O_{9-y} \qquad VII$$

to determine the phase boundary between the two components of

the non reference electrode. Investigations in the one phase UO_{2+x} region were carried out by eliminating the second phase U_4O_{9-y} from Cell VII. A technique of coulometrically titrating oxygen ions from the reference electrode to the uranium oxide was used for the region close to stoichiometry. In this manner the composition was changed over a wide range by adding or removing oxygen electrochemically. Following each titration, the open circuit emf was measured as a function of temperature. Coulometric titration techniques have been used to investigate the nonstoichiometric oxides of TiO_2, VO_2, NbO_2, MoO_2 and UO_2 (51) and FeO (52).

The success of titration experiments suggested the possible application of solid oxide electrolytes as solid state oxygen ion pumps. An applied voltage across the electrolyte establishes an oxygen ion current which changes the oxygen potential at the non-reference electrode. Although the ion pump is still in its infancy, there have been several investigations which have shown promise. Yuan and Kröger (53) have removed oxygen from stationary and flowing gases using a CSZ electrolyte and an air reference electrode. While determining the lower electrolytic boundary for 8 m/o YDT, Tretyakov and Muan (54) coulometrically pumped oxygen from a gas tight com-

partment using an air reference electrode and a double electrolyte composed of a CSZ layer adjacent to a YDT layer.

The application of solid electrolytes which has received the most attention within the past decade has been the area of fuel cells. Weissbart and Ruka (55) reported the possibility of using CSZ in a fuel cell for converting the chemical energy of reaction between a carbonaceous fuel and an oxidant directly to electrical energy. Several laboratories are presently pursuing research along these lines.

Recently galvanic cells with solid oxide electrolytes have found application in kinetic studies involving diffusion-controlled and phase boundary reactions. Rickert (56) measured the oxygen diffusivity in silver by means of the following cell.

Fe,FeO/YSZ/Ag + O(dissolved) VIII

The open circuit emf yielded the initial oxygen concentration in silver. Once this had been established, oxygen was titrated by means of an external applied voltage from the silver electrode to the reference electrode. Since the oxygen diffusion through the silver was the rate limiting step, the measured electrical current is equivalent to the oxygen which is diffusing out of the silver. Thus the oxygen diffusion coef-

ficient can be calculated.

A slight modification of Cell VIII has allowed Tare and Schmalzried (57) to determine the phase boundary reaction rate constant for the oxidation of iron foils in various CO_2/CO atmospheres. A thin iron foil was sintered on a CSZ electrolyte tube. The reference electrode was maintained at one atmosphere of oxygen. Initially the CO_2/CO ratio was fixed to maintain the Fe metal. The ratio was then increased and the open circuit emf was recorded with time. By choosing a thin foil, the phase boundary reaction was the rate limiting step rather than the diffusional process through the foil, consequently the measured emf reflected the phase boundary reaction rate. It is interesting to note that in this way Tare and Schmalzried were able to measure the supersaturation necessary to nucleate the first wüstite nuclei on the iron foil.

Implicit in all of the applications for solid electrolytes is the assumption that the ionic transference number is unity. Therefore it is imperative when investigating a new material as a possible electrolyte to determine its electrolytic domain and if necessary take into account departures from $t_{ion} = 1$ by applying the rules of defect chemistry.

Previous Studies on Undoped Yttria

Yttrium does not belong in the lanthanide series, however owing to its external electronic configuration, it is commonly associated with the rare earths. Yttrium sesquioxide, Y_2O_3, is the only known solid oxide of yttrium. At room temperature and under one atmosphere pressure it possesses the cubic rare earth type C structure (Ia3) (58,59) with 16 sesquioxide formula units per unit cell.

The C type rare earth structure is closely related to the calcium fluoride structure (22,23) with one fourth of the anions missing in order to balance the trivalent cation charge and a slight displacement of the ion positions. The fluorite structure can be represented as an array of cubic MO_8 coordination groups with a cation located at the center of the simple cubic anion cell. The MO_8 groups share edges producing an overall face-centered-cubic symmetry. The C type structure consists of MO_6 coordination groups positioned similar to that of the fluorite array. As a result of the oxygen vacancies and the slight ion displacements, the unit cell possessed a body-centered-cubic symmetry. The oxygen vacancies are located in such a manner as to form relatively open pathways through the oxygen sublattice, consequently material transport

would be expected to be enhanced in these materials. Figure 1A shows an example of the unimpeded paths through the C type rare earth structure.

Electrical conductivity studies and open circuit emf measurements on rare earth sesquioxides and yttria have been few in number. Noddack and co-workers (60-62) determined the electrical conductivity of yttria, many of the rare earth oxides, and several rare-earth oxide binary solid solutions and zirconia-yttria solid solutions. Conductances were determined from dc potential-current and current-temperature measurements. Their samples had been previously sintered at 1300°C for three to six hours. The measurements were carried out in air and in vacuum of unknown oxygen potential. The absence of observing a decomposition potential, separation of materials at the electrodes, and a polarization current indicated that the investigated materials exhibited only electronic conduction between 600 and 1200°C. Activation energies were reported for the conduction processes.

The most reliable conductivity measurements on yttria have been made by Tallan and Vest (63). The electrical conductivity of very pure, polycrystalline Y_2O_3 was obtained from guarded measurements with an ac bridge. The oxygen

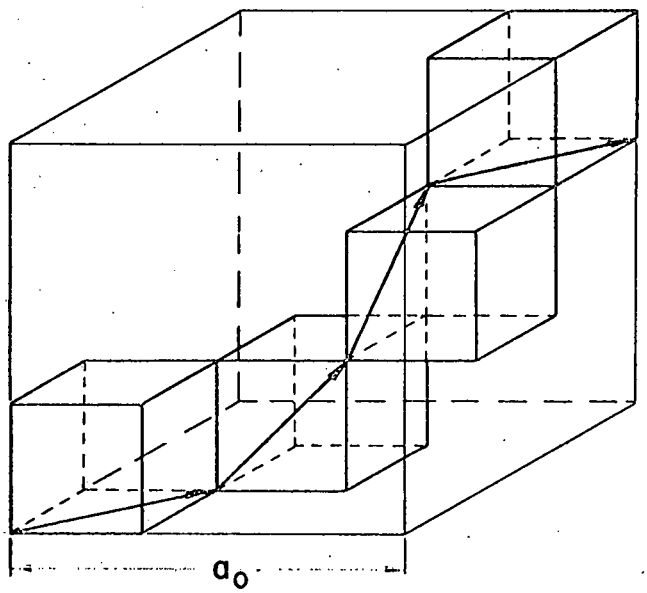

Figure 1A. Unimpeded pathways along 110 directions (RE_2O_3 type C structure)

potential in the gas phase was controlled by using pure oxygen at various pressures, CO and CO_2 mixtures, or H_2 and H_2O mixtures. The data indicated that yttria is an amphoteric semiconductor over the temperature range 1200 to 1600°C and oxygen partial pressures of 10^{-1} to 10^{-17} atm. Within this region the ionic contribution to the total conductivity was less than 1% as determined by the blocking electrode polarization technique. In the region of predominant hole conduction, the conductivity could be expressed by the following relationship.

$$\sigma = 1.3 \times 10^{3} \; P_{O_2}^{3/16} \exp(-1.94/kT) \qquad (13)$$

The observed pressure dependence was attributed to fully ionized yttrium vacancies. Measurable polarization was detected at lower temperatures. The ionic transference number was 0.15 at 800°C and an oxygen partial pressure of 10^{-15} atm. At the same oxygen pressure and 700°C, the ionic transference number had increased to 0.3 indicating mixed conduction in yttria below 900°C.

While investigating the defect structure of ThO_2-Y_2O_3 solid solutions, Subbarao et al. (9) measured the electrical conductivity of pure yttria in air between 800 and 1400°C. The activation energy for conduction agreed quite well with that reported by Tallan and Vest.

Schmalzried (64) measured the open circuit emfs at temperatures between 800 and 1000°C across several rare earth sesquioxides using a galvanic cell of the form:

$$Fe,FeO/RE_2O_3/Ni,NiO\ . \qquad IX$$

The observed open circuit emfs were in agreement with theoretically calculated values demonstrating predominant ionic conduction. These results were encouraging enough to promote further investigations by Tare and Schmalzried (21) over more extended oxygen partial pressures. A galvanic cell of the form

$$Pt,P'_{O_2}/RE_2O_3/P''_{O_2},Pt \qquad X$$

was employed by carefully attaching sintered disks of the rare earth oxides onto a CSZ open end impervious tube. The inside of the tube was maintained at 1 atm pure oxygen while the external oxygen pressure was controlled by N_2-O_2, CO_2-CO, or H_2-H_2O mixtures. All the rare earth oxides investigated with the exception of ceria exhibited predominant ionic conductivity over an intermediate oxygen partial pressure region. The parameters $P_{\oplus}$ and $P_{\ominus}$ which are characteristic of the material were defined as oxygen pressures at which the ionic conductivity equals the hole conductivity or the excess electron conductivity respectively. Only one determination

for yttria was reported. At 825°C the $P_{\oplus}$ value was $10^{-4.2}$ and the $P_{\ominus}$ value was $10^{-21.5}$. $P_{\oplus}$ and $P_{\ominus}$ values for other rare earth oxides were reported.

Macki (65) investigated the electrolytic behavior of doped and undoped Dy_2O_3 and Gd_2O_3 by electrical conductivity studies and open circuit emf measurements. The doped oxides contained various percentages of ThO_2 and CaO. Undoped Gd_2O_3 and ThO_2-doped Gd_2O_3 exhibited predominant ionic conductivity over a small intermediate oxygen potential region, thus nullifying their usefulness as solid electrolytes. The data indicated that CaO doped Gd_2O_3 could be used as a solid electrolyte in regions of low oxygen pressures. The conductivity behavior of Dy_2O_3 and CaO-doped Dy_2O_3 could not be described by a simple defect model. Both the undoped and doped Dy_2O_3 did not show any appreciable ionic conductivity, consequently they were classed unacceptable as solid oxide electrolytes.

Bhattacharyya (66) studied the electrical conductivity of polycrystalline and single crystal Er_2O_3 between 450 and 1450°C and oxygen pressures of 10^0 to 10^{-6} atm. The conductivity could be expressed as

$$\sigma = \sigma_0 P_{O_2}^{1/m} \exp(-E/kT) \qquad (14)$$

with the observed behavior analyzed in terms of two defect

models, metal vacancies and anion interstitials. The various pressure dependencies reported were attributed to the ionization states of the metal vacancies. Electrical conductivity and thermoelectric power measurements indicated predominant hole conduction within the stated temperature and oxygen pressure regions.

McPheeters et al. (67) have patented an electrochemical cell which uses high purity yttria as the electrolyte to continually monitor the oxygen content in a liquid sodium reactor coolant. The particular cell employed was

$$Na,Na_2O/Y_2O_3/Na[O]. \qquad XI$$

Yttria was chosen as the electrolyte material because of its predominant ionic conductivity at temperatures and oxygen potentials present in the sodium coolant loop of a reactor. It also exhibited inert behavior toward liquid sodium and could be fabricated into an impervious state. Observed open circuit emf measurements were on the order of 80 to 100 mv which corresponded to 7 to 30 ppm oxygen in sodium.

Previous Studies on Doped Hafnia

As in the case of the rare earth oxides, there have been a limited number of investigations on doped hafnia. Johansen and Cleary (19) measured the electrical conductivity of CaO-

HfO_2 solid solutions from 800 to 2000°C. The conductivity was assumed to be ionic based on previously reported investigations of CaO-ZrO_2 solid solutions. The oxygen potential was not reported but must have been limited to low or intermediate oxygen partial pressures, since a graphite resistance furnace with an argon atmosphere was used. The maximum conductivity was found to be at 12.5 m/o CaO or 6.25% anion vacancies.

Added insight into the electronic conductivity in calcia stabilized hafnia can be obtained from the oxygen permeability studies by Smith (17). A ¼-power oxygen pressure dependence of the permeability was found for 13.5 m/o CaO-HfO_2 with an activation energy for hole conduction of 58.5 kcal/mole. The transport mechanism was attributed to the migration of oxygen vacancies and electron holes.

Most of the studies involving the rare earth oxides and hafnia deal with the structural determination of various solid solutions, including the existence of a pyrochlore compound $Re_2Hf_2O_7$, and the general determination of phase diagrams (68, 69). Caillet et al. (70) have done a structural study of the HfO_2-Y_2O_3 system from 0 to 50 m/o Y_2O_3. From x-ray diffraction analyses, a two phase region existed between 0 and 8 m/o Y_2O_3 and only the cubic fluorite phase was present above 8 m/o

Y_2O_3. The lattice parameter showed an anomaly at 33.3 m/o Y_2O_3. Along with the electrical conductivity studies by Besson et al. (18) which showed a minimum in conductivity and a maximum in activation energy at 1000°C for the 33.3 m/o Y_2O_3 composition, the existence of the pyrochlore compound $Y_2Hf_2O_7$ was predicted but never really observed. An a-c two probe method was used to measure the electrical conductivity of various yttria-hafnia solid solutions in a controlled atmosphere. The 8 m/o Y_2O_3 composition exhibited a maximum conductivity which was pressure independent and a minimum activation energy. An oxygen pressure dependence was observed with compositions containing less than 8 m/o Y_2O_3 and was interpreted as the electronic contribution from the monoclinic solid solution within the two phase region. Open circuit emf values across various cubic fluorite compositions between Ni-NiO and Fe-FeO electrodes agreed with thermodynamic values verifying that the electrical conductivity remains ionic down to oxygen pressures fixed by the electrodes.

STATEMENT OF PURPOSE

This investigation involved the measurement of the electrical conductivity of undoped yttria over an oxygen partial pressure range of 1 to 10^{-16} atm and a temperature range of 700 to 1000°C. Open circuit emfs were measured over the same temperature interval and oxygen partial pressures of 10^{-6} to 10^{-50} atm.

Electrical conductivity measurements on yttria-hafnia compositions between 6 and 20 mole percent yttria were performed between 800 and 1000°C and oxygen partial pressures of 1 to 10^{-12} atm to determine the optimum composition for further investigations as a possible electrolyte. Open circuit emf measurements, coulometric titration experiments, and polarization studies were performed to determine the electrolytic behavior of the chosen composition.

The purpose of this investigation was to determine the electrolytic domains ($t_{ion} \geq 0.99$) of undoped yttria and yttria stabilized hafnia. Within these domains, these oxides could be used as solid electrolytes in high-temperature galvanic cells.

THEORY

Conduction Domain Theory

It has already been pointed out in the literature survey that a mixed conductor is regarded as a solid electrolyte when its ionic transference number exceeds 0.99: i.e.,

$$t_{ion} = \sigma_{ion}/(\sigma_{ion} + \sigma_{\oplus} + \sigma_{\ominus}) \geq 0.99 \qquad (15)$$

where σ_{ion} represents the total conductivity which may arise from both cation or anion defects and $\sigma_{\oplus}$ and $\sigma_{\ominus}$ represent the positive hole and excess free electron conductivity respectively. This definition is motivated by the desirability of reducing Wagner's general relationship (Equation 16A),

$$E = \frac{-1}{2Z_0F} \int_{\mu_{O_2}(O)}^{\mu_{O_2}(L)} t_{ion}\, d\mu_{O_2} \qquad (16)$$

to the simplified version

$$E = \frac{\mu_{O_2}(L) - \mu_{O_2}(O)}{2Z_0F} . \qquad (17)$$

Equation 17, because of its simplicity and usefulness in analyzing galvanic cells, has found more application than Equation 16.

If the oxygen chemical potential, μ_{O_2}, and the temperature, T, dependences of σ_{ion}, $\sigma_{\oplus}$, and $\sigma_{\ominus}$ can be established

experimentally, then the individual conductivity expressions can be inserted into Relation 15 to deduce the μ_{O_2} and T range in which a material behaves as an electrolyte. This range corresponds to the electrolytic domain of the mixed conductor. For mathematical convenience, the variables log P_{O_2} and $1/T(^oK)$ are preferred over μ_{O_2} and T, therefore conductivity domains will be described in terms of log P_{O_2} vs. 1/T diagrams. The change in variables is easily accomplished since the oxygen chemical potential, μ_{O_2}, is related to the oxygen partial pressure, P_{O_2}, and the absolute temperature, T, by

$$\mu_{O_2} = \mu^o_{O_2} + RT \ln P_{O_2} \qquad (18)$$

where R is the universal gas constant and $\mu^o_{O_2}$ is the chemical potential of oxygen in its standard state. It should be pointed out here that retention of the μ_{O_2} variable would allow the data to be plotted directly on a Richardson and Jeffes diagram (71).

At elevated temperatures solid electrolytes exhibit an ionic conductivity which is virtually independent of oxygen pressure. In contrast $\sigma_\oplus$ and $\sigma_\ominus$ are found to be proportional to $P_{O_2}^{1/n}$ and $P_{O_2}^{-1/n}$ respectively at constant temperature. The value of n is dictated by the existing defect structure within the mixed conductor. At constant P_{O_2}, all three conductivities

exhibit an Arrhenius-type temperature dependence with apparent activation energies Q_{ion}, $Q_{\oplus}$, and $Q_{\ominus}$. By definition the total conductivity in a mixed conductor can be written as:

$$\sigma_T = \sigma_{ion} + \sigma_{\oplus} + \sigma_{\ominus} . \tag{19}$$

However, from experimental observation the following empirical dependencies are found:

$$\sigma_{ion} = \sigma^o_{ion} \exp(-Q_{ion}/RT) \tag{20}$$

$$\sigma_{\oplus} = \sigma_{\oplus} P_{O_2}^{1/n} \exp(-Q_{\oplus}/RT) \tag{21}$$

$$\sigma_{\ominus} = \sigma^o_{\ominus} P_{O_2}^{-1/n} \exp(-Q_{\ominus}/RT) \tag{22}$$

where the parameters σ^o_{ion}, $\sigma^o_{\oplus}$, $\sigma^o_{\ominus}$, n, Q_{ion}, $Q_{\oplus}$, and $Q_{\ominus}$ are P_{O_2} and T independent. Theoretical justification of these empirical formulas for σ_{ion}, $\sigma_{\oplus}$, and $\sigma_{\ominus}$ will be discussed later.

The electrical behavior for a mixed conductor is summarized graphically in Figure 1B. Surfaces corresponding to log σ_{ion}, log $\sigma_{\oplus}$, and log $\sigma_{\ominus}$ plot as planar sheets in log σ, log P_{O_2}, 1/T space because of their functional form. Figure 1B may be thought of as a three dimensional Kröger and Vink diagram (72). Regions A, C, and D in Figure 1B exist where only one conduction mode dominates the total conductivity. Projections of these regions onto the log P_{O_2}, 1/T plane are called the positive hole, excess electron, and electrolytic

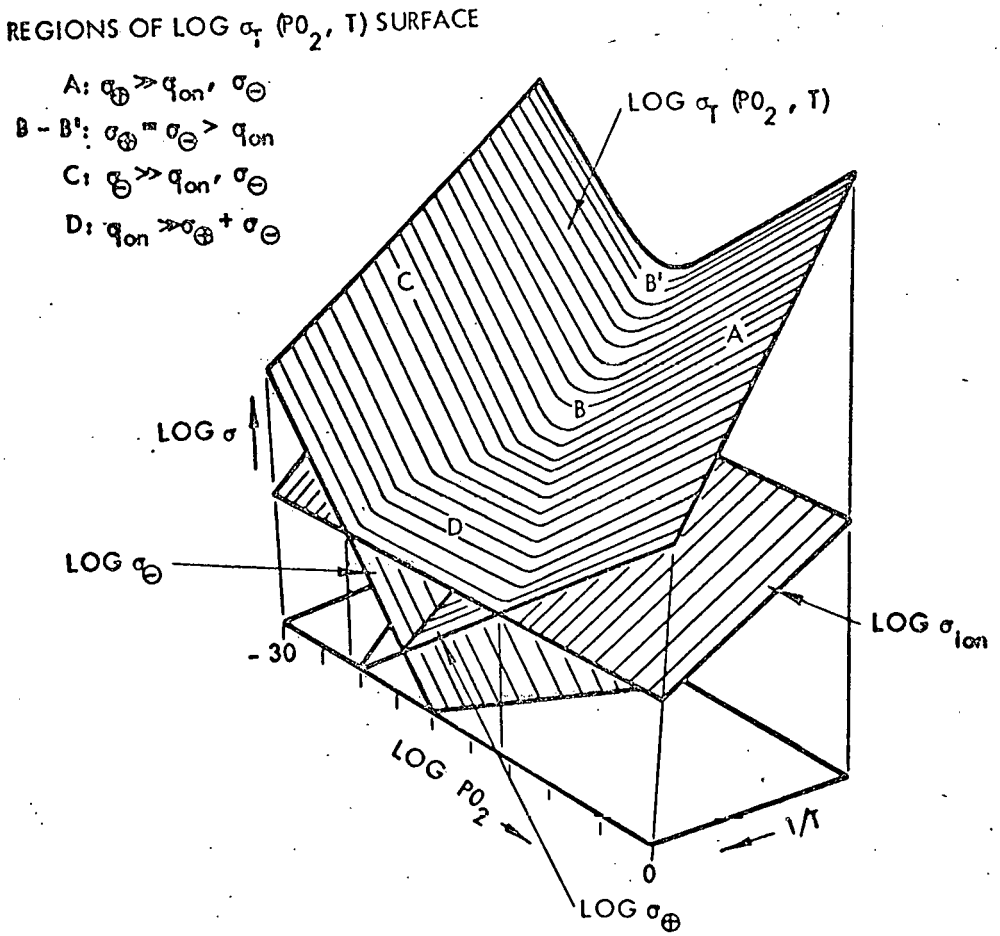

Figure 1B. Schematic representation of log σ surfaces over log P_{O_2}, 1/T space for $\sigma = \sigma_{ion}$, $\sigma_\oplus$, $\sigma_\ominus$, and σ_{total}

conduction domains for a mixed conductor. Thus the electrolytic domain falls within the ionic domain which is defined by the condition

$$\sigma_{ion} \geq \sigma_{\oplus} \text{ or } \sigma_{\ominus} \tag{23}$$

then

$$t_{ion} \geq 0.5. \tag{24}$$

Various domain boundaries, which represent transition conditions for a mixed conductor, can be determined by equating appropriate conductivity expressions. Ionic domain boundaries can be determined by equating σ_{ion} to $\sigma_{\oplus}$ and $\sigma_{\ominus}$ respectively and taking the logarithm of the results,

$$\log P_{\oplus} = -n \frac{Q_{ion} - Q_{\oplus}}{2.303\ R} \frac{1}{T} + n \log \frac{\sigma^{o}_{ion}}{\sigma^{o}_{\oplus}} \tag{25}$$

$$\log P_{\ominus} = n \frac{Q_{ion} - Q_{\ominus}}{2.303\ R} \frac{1}{T} - n \log \frac{\sigma^{o}_{ion}}{\sigma^{o}_{\ominus}} \tag{26}$$

where the parameters $P_{\oplus}$ and $P_{\ominus}$ retain their definitions as proposed by Schmalzried (64). In general, the main interest is limited to applications of mixed conductors within their electrolytic domains. According to the definition of an electrolyte as given above (Relation 15) these boundaries can be determined by equating σ_{ion} to $100\sigma_{\oplus}$ and $100\sigma_{\ominus}$ respectively,

$$\log P^*_{\oplus} = \log P_{\oplus} - 2n$$
$$\log P^*_{\ominus} = \log P_{\ominus} + 2n \qquad (27)$$

where $P^*_{\oplus}$ and $P^*_{\ominus}$ represent oxygen partial pressures corresponding to the above conditions. Any application of a mixed conductor requiring electrolytic behavior must correspond to $\log P_{O_2}$, 1/T conditions which lie between the lines defined by Equations 26 and 27. Figure 1C shows the relationships among the various domain boundaries.

If the parameters σ_{ion}, $\sigma_{\oplus}$, $\sigma_{\ominus}$, n, Q_{ion}, $Q_{\oplus}$, and $Q_{\ominus}$ remain constant, Equations 26 and 27 can be extrapolated beyond the limited ranges determined by direct measurements. Such extrapolations can prove a tremendous advantage in predicting the success of a mixed conductor when used as an electrolyte in a specific application. Also the domain theory provides a means for comparing and critically evaluating data among various investigators.

Experimentally, the foregoing domain concept appears very attractive because electrical conductivity and open circuit emf studies give complementary, yet independent, information concerning the conduction domain boundaries. Electrical conductivity measurements may be used to establish a particular location and orientation for a conductivity sheet in $\log P_{O_2}$, 1/T

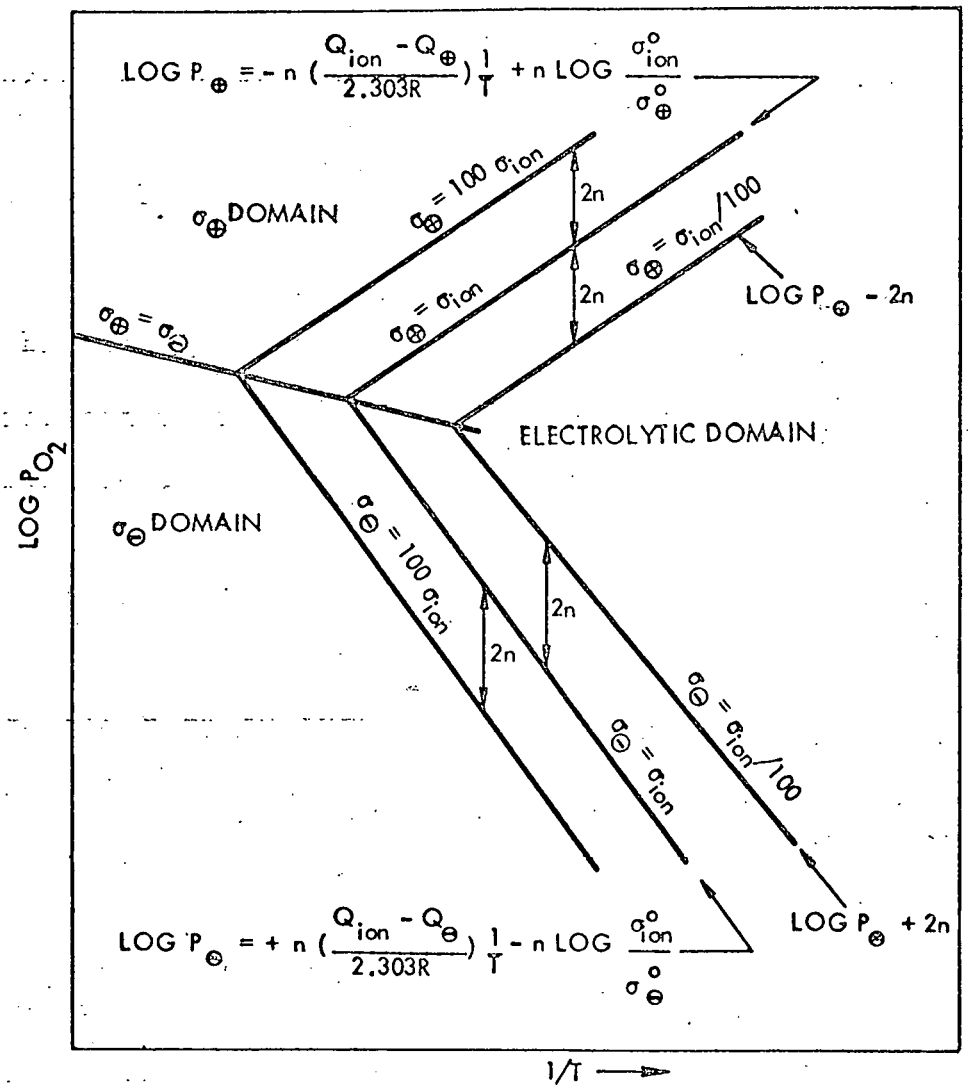

Figure 1C. Relationship between electrolytic and ionic domain boundaries in the log P_{O_2}, 1/T plane

space. The intersections between different sheets are simply related to the various conductivity domain boundaries. In the case of open circuit emf measurements, in which certain electrode conditions are satisfied, the departure of the measured emf from the thermodynamic value is used to gain information regarding the ionic and electrolytic boundaries.

Theory of Partial Electrical Conduction

Introduction

Experimental methods have been developed to measure partial conductivities directly. Consequently the nature of the partial conductivities has been rather well established particularly with respect to their dependence upon chemical potentials and temperature. Theoretically the partial conductivity for a given charge carrier, σ_i, is the product of the carrier concentration, n_i; its mobility, u_i; and its charge, $z_i e$.

$$\sigma_i = n_i z_i e u_i \tag{28}$$

Generally, direct measurement of these quantities is much more difficult than measurement of the conductivities. For ionic compounds, present understanding of the dependence of individual carrier concentrations and especially of carrier mobilities is quite limited. Although the Arrhenius tempera-

ture dependence is commonly observed for ionic and electronic conductivities, it is not presently possible to separate the temperature dependence due to the mobility from that due to the carrier concentration. Realistically, it would seem plausible to regard both the migration process and the defect formation process as being thermally activated. Consequently, in this work carrier concentrations will be converted to conductivities using the assumption that the mobility can be expressed as

$$u_i = u_i^o \exp(-Q_i/RT). \qquad (29)$$

Defect equilibria and electrical conductivity in undoped yttria

Various density, x-ray, and diffusion studies (20,22,23, 73,74,75,76) on yttria and rare earth oxides indicate that deviations from stoichiometry are limited to disturbances on the anion sublattice, namely the formation of oxygen vacancies and interstitials. Normally, the presence of oxygen interstitials is eliminated from consideration for most structures based on geometric arguments. In the case of Y_2O_3, the lattice corresponds to the fluorite structure except that one-quarter of the anion sites remain vacant. Since these vacant sites would remain unoccupied at absolute zero, they are considered to be interstitial sites (75). Thus geometrically the C-type

rare earth oxide structure can adequately accommodate oxygen interstitials.

Based on previous investigations in the temperature range involved, 700 to 1000°C, the defect equilibria considered in Y_2O_3 will be limited to fully-ionized oxygen vacancies, $V_O^{\cdot\cdot}$, and interstitials, O_i''

The intrinsic equilibrium which controls the generation of anion defects under stoichiometric conditions is the dissociation reaction involving normal oxygen sites and is described by the anti-Frenkel reaction:

$$O_O^x \rightleftharpoons O_i'' + V_O^{\cdot\cdot} . \tag{30}$$

The incorporation equilibria control the formation of the electronic defects and also the anion defects under nonstoichiometric conditions. These allow the crystal to change stoichiometry by the addition or removal of oxygen according to the following reactions:

$$\tfrac{1}{2}O_2 \rightleftharpoons O_i'' + 2\oplus \tag{31}$$

$$O_O^x \rightleftharpoons \tfrac{1}{2}O_2 + V_O^{\cdot\cdot} + 2\ominus. \tag{32}$$

Since the concentration of defects is quite small, the thermodynamic activities can be approximated by the concentration. The concentration of defects generated by Reactions 30, 31, and 32 are related, under equilibrium conditions, through

the application of the law of mass action as follows:

$$K_1 = [V_O^{\cdot\cdot}][O_i''] \tag{33}$$

$$K_2 = [O''][\oplus]^2 P_{O_2}^{-\frac{1}{2}} \tag{34}$$

$$K_3 = [V_O^{\cdot\cdot}][\ominus]^2 P_{O_2}^{\frac{1}{2}} \tag{35}$$

where the equilibrium constants, K_i, contain the energy required for the formation of the particular defect. A further constraint on the crystal requires that overall electrical neutrality be maintained.

$$[\oplus] + 2[V_O^{\cdot\cdot}] = [\ominus] + 2[O_i''] \tag{36}$$

At sufficiently high oxygen pressures, the predominant defects are presumed to be O_i'' and $\oplus$. This allows the electroneutrality condition to be approximated by

$$[\oplus] = 2[O_i''] . \tag{37}$$

Substitution of Equation 37 into 34 shows that the hole concentration is proportional to the 1/6 power of the oxygen pressure.

$$[\oplus] = (2K_2)^{1/3} P_{O_2}^{1/6} \tag{38}$$

Since the electronic defect mobilities are much greater than the ionic defect mobilities, no significant ionic conduction is anticipated at these high oxygen pressures. Consequently, the electrical conductivity for Y_2O_3 in high P_{O_2} regions can

be expressed as

$$\sigma_{\oplus} = \sigma_{\oplus}^{o} P_{O_2}^{1/6} \exp(-Q_{\oplus}/RT) \tag{39}$$

where $\sigma_{\oplus}^{o}$ is a material constant independent of P_{O_2} and T. The activation energy, $Q_{\oplus}$, consists of the defect formation and migration energies.

Application of similar arguments for the low P_{O_2} region where Θ and $V_O^{\cdot\cdot}$ are presumed to be dominant leads to an expression for the excess electron conductivity.

$$\sigma_{\Theta} = \sigma_{\Theta}^{o} P_{O_2}^{-1/6} \exp(-Q_{\Theta}/RT) \tag{40}$$

At intermediate oxygen pressures, the concentrations of oxygen vacancies and interstitials are essentially independent of P_{O_2} and are determined only by

$$[V_O^{\cdot\cdot}] = [O_i''] = K_1^{\frac{1}{2}} . \tag{41}$$

Substitution of Equation 41 into 34 and 35 and subsequent use of these defect concentrations to compute the individual conductivities results in the following expressions:

$$\sigma_{ion} = \sigma_{ion}^{o} \exp(-Q_{ion}/RT) \tag{42}$$

$$\sigma_{\oplus} = \sigma_{\oplus} P_{O_2}^{\frac{1}{4}} \exp(-Q_{\oplus}/RT) \tag{43}$$

$$\sigma_{\Theta} = \sigma_{\Theta}^{o} P_{O_2}^{-\frac{1}{4}} \exp(-Q_{\Theta}/RT). \tag{44}$$

The defect equilibria in undoped Y_2O_3 over all P_{O_2} ranges are summarized in Figure 1D. Note that only Zone II is included

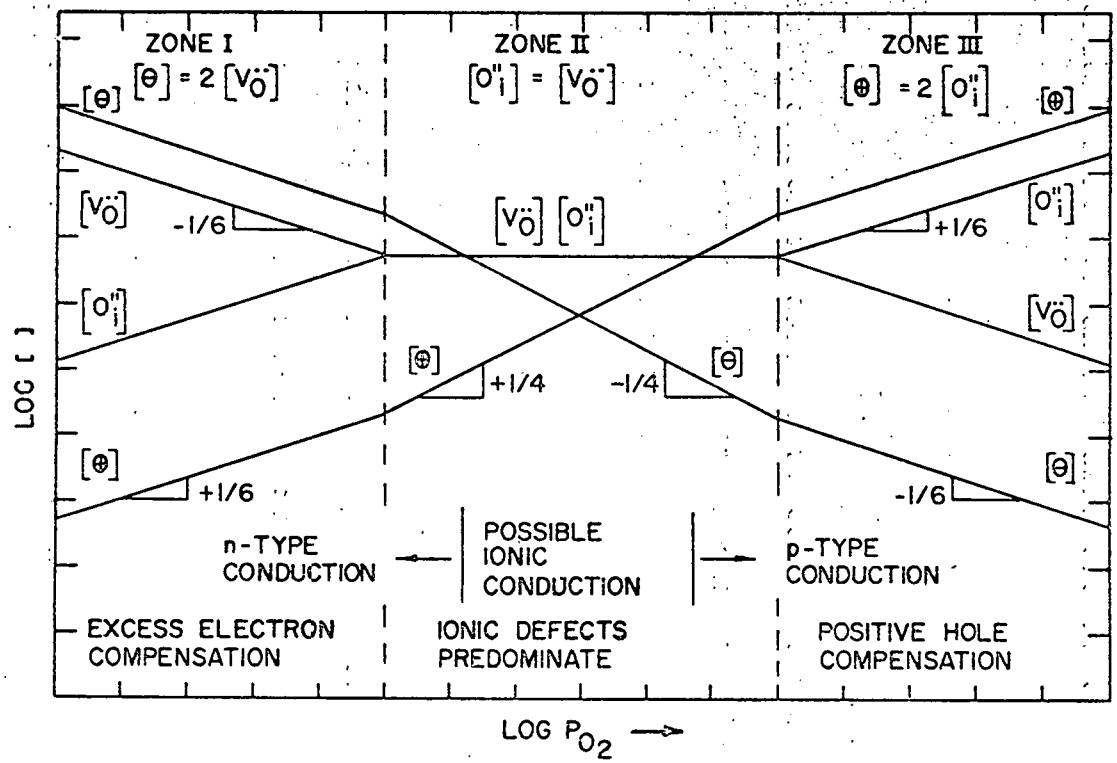

Figure 1D. Defect equilibria in pure Y_2O_3

in Figure 1B.

It is important to note that the functional forms of the individual conductivities as derived from defect equilibria are identical to the functional forms of the empirical conductivities used in the electrolytic domain theory.

When the concentration of charge carriers is determined by impurities or dopants rather than by thermodynamically created defects within the crystal, the impurity or dopant level can control the conduction. In the case of Y_2O_3, an aliovalent impurity cation is assumed to occupy a normal cation site producing a compensating anion defect. The net effect might be to render the anion defect concentration independent of log P_{O_2} as well as temperature since these defects are not thermally generated, but rather are fixed only by the aliovalent ion concentration. An example of this would be the incorporation of a divalent cation on an yttrium site, M_Y', with $V_O^{\cdot\cdot}$ being the compensating defect. Substitution of the electrical neutrality condition

$$[V_O^{\cdot\cdot}] = \tfrac{1}{2}[M_Y'] = \tfrac{1}{2}[MO] = \text{constant} \qquad (45)$$

into Equations 34 and 35 leads to expressions for the electronic defect concentrations

$$[\oplus] = K_2^{\frac{1}{2}} (2K_1)^{-\frac{1}{2}} [MO]^{\frac{1}{2}} P_{O_2}^{\frac{1}{4}} \qquad (46)$$

$$[\theta] = (2K_3)^{\frac{1}{2}} [MO]^{-\frac{1}{2}} P_{O_2}^{-\frac{1}{4}} \quad (47)$$

where [MO] represents the concentration of divalent metal oxide added to Y_2O_3. Thus the same value of n, namely n = 4, may characterize the P_{O_2} dependence of $[\oplus]$ and $[\theta]$ and hence of $\sigma_\oplus$ and σ_θ for doped Y_2O_3 as well as undoped Y_2O_3 in intermediate P_{O_2} ranges.

In general any of several different defect equilibrium schemes (72) can lead to the same value of n. Consequently the parameter n cannot be used to unequivocally distinguish among such cases and independent information must also be considered. Examples of such independent information may include density-lattice parameter data, which will be discussed later for YSH, as well as the activation energies for conduction. These activation energies may be expected to vary markedly depending on which defect equilibria dominate the defect structure of the crystal. In view of the large number of defect structures that may be proposed to rationalize the P_{O_2} dependencies between n = 4 and 6, discussion has been restricted to the most plausible defect equilibrium based on theoretical models proposed by Wagner (77) and Schmalzried (64). These proposals have been favored over that proposed by Tallan and Vest (63) for Y_2O_3.

Defect equilibria and electrical conductivity in yttria doped hafnia solid solutions

Much of the pioneering work on the electrical conductivity and defect structure of fluorite solid solutions has been done on CSZ and YDT. Since YSH possesses the same structure as CSZ and YDT, the conduction mechanisms and defect structures would also be expected to be identical.

Electrical conductivity measurements on CSZ (4) and YDT (9,10,78) indicate a P_{O_2}-independent conductivity over a large P_{O_2} range. The agreement of measured emfs (4,9,10) with values predicted from thermodynamic data prove that this conductivity results from oxygen ion migration. Density measurements (7,9) and oxygen diffusion studies (11) indicate that the presence of anion vacancies is responsible for the oxygen ion conductivity. Thus these studies confirm that the oxygen ion transference number is virtually unity over a wide P_{O_2} range.

As previously pointed out, the electrolytic domain is limited by the onset of electronic conductivity. Wagner d-c polarization measurements (14,79) have been used to locate these onsets for both materials. The measurements also show a $-\frac{1}{4}$ P_{O_2} dependence for the excess electron conductivity and a $+\frac{1}{4}$ P_{O_2} dependence for the positive hole conduction. Inde-

pendent oxygen permeability studies (17) support the $+\frac{1}{4}$ P_{O_2} dependence of the hole conductivity. Empirically both CSZ and YDT possess large electrolytic domains which are terminated by the onset of hole and electron conductivities possessing a $+\frac{1}{4}$ and $-\frac{1}{4}$ P_{O_2} dependence, respectively.

The accepted model which predicts the above behavior requires the aliovalent dopant ion to occupy a normal cation site. Since the crystal is constrained to maintain electrical neutrality, it does so by forming anion vacancies.

$$[V_O^{\cdot\cdot}] = [Y_2O_3] = \tfrac{1}{2}[Y'_{Hf}] \tag{48}$$

The term $[Y_2O_3]$ indicates the dopant concentration of Y_2O_3 in HfO_2. Deviations from stoichiometry are expressed by the following incorporation reactions:

$$\tfrac{1}{2}O_2 + V_O^{\cdot\cdot} \rightleftharpoons O_O^X + 2\oplus \tag{49}$$

$$O_O^X \rightleftharpoons \tfrac{1}{2}O_2 + V_O^{\cdot\cdot} + 2\ominus. \tag{50}$$

Application of the law of mass action and the definition of electrical conductivity leads to the following expressions for the individual conductivities:

$$\sigma_{ion} = \sigma^o_{ion} \exp(-Q_{ion}/RT) \tag{51}$$

$$\sigma_{\oplus} = \sigma^o_{\oplus} P_{O_2}^{\frac{1}{4}} \exp(-Q_{\oplus}/RT) \tag{52}$$

$$\sigma_{\ominus} = \sigma^o_{\ominus} P_{O_2}^{-\frac{1}{4}} \exp(-Q_{\ominus}/RT). \tag{53}$$

Again, for the case of YSH, the functional forms of the conductivities derived from defect equilibria are identical to the functional forms of the observed conductivities.

In general, the dopant concentration generates such a large number of oxygen vacancies that the ionic conductivity overwhelms the electronic contributions resulting in electrolytic behavior in the sense of Relation 15 over a fairly large P_{O_2} range.

Theory of Open Circuit Emf Measurements

Wagner (2,77,80) has shown that the open circuit emf measured across an oxide mixed conductor between dissimilar, virtually reversible electrodes is given by Equation 16A,

$$E = \frac{-1}{2Z_0F} \int_{\mu_{O_2}(0)}^{\mu_{O_2}(L)} t_{ion}\, d\mu_{O_2}. \qquad (16)$$

The ionic transference number, t_{ion}, is defined by Equation 15, Z_0 is the absolute value of the oxygen ion valence, and F is Faraday's constant. The oxygen chemical potentials, μ_{O_2}, at each location x = 0 and x = L are held constant by the electrodes such that $\mu_{O_2}(0) > \mu_{O_2}(L)$. The electrochemical cell being

$$\mu_{O_2}(0)_{x=0}/\text{mixed oxide conductor}/\mu_{O_2}(L)_{x=L}. \qquad \text{XII}$$

In view of the gradient of chemical potentials, anions migrate from the left-hand to the right-hand side of the above cell at a rate that is limited by the migration rate of electrons in the opposite direction. The potential difference under a steady state condition created by the redistribution of carriers within the mixed conductor is the open circuit emf.

It has already been shown that, in the case of predominant ionic conduction, Equation 16 simplifies to Equation 17. Schmalzried (64) has examined the consequences of t_{ion} departing from unity. The initial step and most critical part of his theory involves expressing t_{ion} as a function of μ_{O_2}. Once this is known the integral in Equation 16 can be evaluated.

For convenience and compliance with conductivity data, the variable of integration μ_{O_2} is changed to P_{O_2} by means of Equation 18. Based on empirical results and defect equilibria involving anion defects in a mixed oxide conductor, Schmalzried chose the following functional forms for the individual conductivities at a constant temperature:

$$\sigma_{ion} = K_{ion} = \text{constant} \qquad (54)$$

$$\sigma_{\oplus} = K_{\oplus} P_{O_2}^{1/n} \tag{55}$$

$$\sigma_{\ominus} = K_{\ominus} P_{O_2}^{-1/n}. \tag{56}$$

It should be noted that these expressions are identical to those used in the conduction domain theory under the condition of constant temperature.

Substitution of Equations 54, 55, and 56 into Equation 15, and introduction of the parameters $P_{\oplus}$ and $P_{\ominus}$, where

$$P_{\oplus} = (K_{\ominus}/K_{ion})^{-n} \tag{57}$$

$$P_{\ominus} = (K_{\ominus}/K_{ion})^{n}, \tag{58}$$

allows t_{ion} to be expressed as a function of P_{O_2}.

$$t_{ion} = [1 + (P_{O_2}/P_{\oplus})^{1/n} + (P_{O_2}/P_{\ominus})^{-1/n}]^{-1} \tag{59}$$

The conductivity parameters $P_{\oplus}$ and $P_{\ominus}$ are the oxygen partial pressures where $\sigma_{ion} = \sigma_{\oplus}$ and $\sigma_{ion} = \sigma_{\ominus}$, respectively. Substituting Equation 59 into 16 and integrating between the limits of $P_{O_2}(0)$ and $P_{O_2}(L)$ results in Schmalzried's most general expression for the open circuit emf,

$$E = \frac{nRT}{4F\omega}\left[\ln\frac{1 + \omega + 2\beta}{1 + \omega + 2\alpha} + \ln\frac{1 - \omega + 2\alpha}{1 - \omega + 2\beta}\right] \tag{60}$$

where

$$\omega = [1 - 4(P_{\ominus}/P_{\oplus})^{1/n}]^{\frac{1}{2}} \tag{61}$$

$$\alpha = [P_{O_2}(0)/P_{\oplus}]^{1/n} \tag{62}$$

$$\beta = [P_{O_2}(L)/P_{\oplus}]^{1/n}. \tag{63}$$

Equation 60 can be simplified for the useful case where $P_{\oplus}$ and $P_{\ominus}$ differ from each other sufficiently that

$$(P_{\ominus}/P_{\oplus})^{1/n} \lesssim 0.01, \tag{64}$$

in this case

$$E = \frac{nRT}{4F}\left[\ln \frac{P_{\oplus}^{1/n} + P_{O_2}^{1/n}(L)}{P_{\oplus}^{1/n} + P_{O_2}^{1/n}(0)} + \ln \frac{P_{\ominus}^{1/n} + P_{O_2}^{1/n}(0)}{P_{\ominus}^{1/n} + P_{O_2}^{1/n}(L)}\right]. \tag{65}$$

By judicious choice of electrodes, Equation 65 can be further simplified and separated into four distinct cases.

Case I results when the P_{O_2} values fixed by the electrodes lie within the electrolytic domain. This condition can be represented by $P_{\oplus} \gg P_{O_2}(0) \gg P_{O_2}(L) \gg P_{\ominus}$. The resulting expression for the open circuit emf is

$$E = \frac{RT}{4F} \ln \frac{P_{O_2}(0)}{P_{O_2}(L)} \tag{66}$$

and is identical to Equation 17.

Case II represents the maximum attainable emf of an electrolyte. This results when the electrodes fix the P_{O_2} values outside of the electrolytic domain such that $P_{O_2}(0) \gg P_{\ominus} \gg P_{\ominus} \gg P_{O_2}(L)$ giving

$$E = \frac{RT}{4F} \ln \frac{P_{\oplus}}{P_{\ominus}}. \tag{67}$$

Case III occurs when one electrode fixes a P_{O_2} value within the electrolytic domain and the second electrode establishes a P_{O_2} value much lower than P_θ. The required condition is $P_\oplus >> P_{O_2}(0) >> P_\theta >> P_{O_2}(L)$ which allows Equation 65 to be reduced to

$$E = \frac{RT}{4F} \ln \frac{P_{O_2}(0)}{P_\theta} . \qquad (68)$$

Equation 68 provides an experimental method for determining P_θ providing the implied approximations are valid. The determination of P_θ at different temperatures would provide information concerning the ionic and electrolytic domain boundaries at low oxygen potentials. Several investigators have used this method to determine the electrolytic domain boundary for CSZ (44) and YDT (15,54) at low oxygen potentials.

Case IV, which is analogous to Case III, is used to extract information concerning the high oxygen potential limits of the ionic and electrolytic domains. The required electrode conditions are $P_{O_2}(0) >> P_\oplus >> P_{O_2}(L) >> P_\theta$ and the resulting emf is

$$E = \frac{RT}{4F} \ln \frac{P_\oplus}{P_{O_2}(L)} . \qquad (69)$$

The characteristic feature of open circuit emf measurements is that they can be used to establish the presence of

ionic conduction. When the measured emf equals the thermodynamic emf, Equation 17, the conduction mechanism is totally ionic and the material is classed as an electrolyte. Similarly, a zero emf would suggest predominant electronic conductivity. Intermediate emfs imply mixed conduction, that is, the presence of both ionic and electronic conduction contributing to the total conductivity. Analysis of data obtained in this region serves to locate the various conduction domains and determine the temperature dependence of certain conductivity parameters.

Theory of D-c Polarization Measurements

The electronic conductivity of mixed conductors has been successfully investigated by d-c polarization techniques as suggested by Hebb (81) and Wagner (77). The cell

$$\underset{x=0}{\text{Reversible Electrode}} \;\Big|\; \text{Oxide Mixed Conductor} \;\Big|\; \underset{x=L}{\text{Nonreversible Electrode}} \qquad \text{XIII}$$

is subjected to a d-c emf below the decomposition voltage of the oxide specimen. The emf may be applied so that the initial migration of the mobile ion is towards the reversible electrode where it is consumed. This requires the reversible electrode to act as a sink to the mobile ion and retain a

known chemical potential of the mobile ion. The blocking electrode prevents mobile ions from entering the specimen at x=L. At steady state, the migration of ions due to the applied emf is counterbalanced by the back diffusion of ions down the chemical potential gradient. Hence, the net ionic flux is zero and the measured current corresponds to the electronic conductivity only. According to Wagner, the total steady state current can be expressed in an integral form[1] which for the case of oxide mixed conductors is equivalent to

$$I_T = I_\oplus + I_\ominus = -\frac{A}{4FL} \int_{\mu_{O_2}(0)}^{\mu_{O_2}(L)} (\sigma_\oplus + \sigma_\ominus) d\mu_{O_2}. \qquad (70)$$

Using the functional forms of the individual conductivities as stated in Equations 54, 55, and 56 where $K_\oplus$ and $K_\ominus$ represent the hole and excess electron conductivities at 1 atm of oxygen, respectively. $K_\oplus$ and $K_\ominus$ can be rewritten in terms of the hole and electron conductivities at the reversible electrode, $\sigma^*_\oplus$ and $\sigma^*_\ominus$

$$K_\oplus = \sigma^*_\oplus P^{*-1/n}_{O_2} \qquad (71)$$

$$K_\ominus = \sigma^*_\ominus P^{*1/n}_{O_2} \qquad (72)$$

---

[1] See Equation 25 on page 368 in reference (77).

where $P^*_{O_2}$ is the partial pressure of oxygen fixed by the reversible electrode. At constant temperature, the general expressions for the total hole and electron conductivities can be rewritten as

$$\sigma_\oplus = \sigma^*_\oplus \, (P_{O_2}/P^*_{O_2})^{1/n} \tag{73}$$

$$\sigma_\ominus = \sigma^*_\ominus \, (P_{O_2}/P^*_{O_2})^{-1/n} \tag{74}$$

which simply involves a change in reference state from pure oxygen to a new reference state defined by the reversible electrode.

Substitution of Equations 73 and 74 into 70 with change of the variable of integration to P_{O_2} gives

$$I_\infty = \frac{nART}{4FL} \left\{ \sigma^*_\oplus [1 - \exp(-4u/n)] + \sigma^*_\ominus [\exp(4u/n) - 1] \right\} \tag{75}$$

where

$$u = EF/RT \tag{76}$$

and E is defined by Equation 17 or 66. It is desirable to rearrange Equation 75 so that electronic conductivities can be read directly from a plot of the data.

$$\frac{I_\infty}{1 - \exp(-4u/n)} \times \frac{4FL}{nART} = \sigma^*_\oplus + \sigma^*_\ominus \exp(4u/n) \tag{77}$$

A "converted" plot based on the data handling method of Patterson (14) should have a slope of $\sigma^*_\ominus$ and an intercept of $\sigma^*_\oplus$.

The above derivation is very similar to Wagner's (77), however the restriction to a specific type of defect equilibrium has been relaxed by inserting general pressure-dependent hole and electron conductivities.

The measured electronic conductivities at the reversible electrode allow the hole and electron conduction sheets to be located in log σ, log P_{O_2}, 1/T space. Extrapolation of these sheets to intersect the ionic conduction sheet determines the ionic domain boundaries and hence locates the electrolytic domain of the oxide mixed conductor.

EXPERIMENTAL EQUIPMENT AND PROCEDURE

Preparation of the Undoped Yttria Samples

The yttrium sesquioxide used in this study was supplied by the Ames Laboratory as the oxide clinker resulting from the calcination of the hydrated yttrium oxalate. A spectrographic analysis of the yttria as received is given in Table 1.

Table 1. Spectrographic analysis of Y_2O_3 powder

Element	Concentration (ppm)
Ca	20
Mg	20
Si	200
Fe	35
Na	faint trace
Cu	20
Ti	30
Ta	<200
Al	100
Co	<35
Yb	<100
Er	<100
Ho	<60
Dy	<100
Gd	<100
Tb	<200
Sm	<250
Total	1570

The soft clinker was wet ground for one hour in a porcelain ball mill using distilled water as the liquid medium and dried to a powder.

Spectrographic analysis of the powder failed to detect any contamination incurred during the milling operation. Particle size analysis showed the average agglomerate size to be 5-10 microns and x-ray diffraction line broadening techniques indicated a crystallite size of 0.1-0.2 microns. A theoretical density of 5.030 gm/cm^3 for pure yttria was calculated from a lattice parameter of 10.6066Å which was determined from several x-ray diffraction patterns. The x-ray equipment and procedures will be discussed later. The characterized yttria powder was used as the starting material for the undoped yttria and the yttria stabilized hafnia samples.

Yttria samples which were to be cold pressed and sintered were prepressed at 1800 p.s.i. in a 3/4 in. diameter double action steel die lined with tungsten carbide. This operation produced the desired shape and green strength necessary for handling. The prepressed yttria disks were isostatically pressed to 50,000 p.s.i. A 6 kw induction furnace, Ajax Electrothermic high frequency converter, was used to sinter the samples at 1850°C for 1 hr. at temperature. An oxidizing atmosphere was maintained in the hot zone by placing an impervious alumina tube which was open to an air atmosphere between the graphite susceptor and the samples. During the firing

operation, the samples were contained in a covered yttria crucible. Water immersion determinations of the bulk densities of the sintered disks were 85 to 90% of theoretical density. In general the porosity was open.

A resistance tungsten heating element furnace (Centorr Associates, Inc., Suncook, New Hampshire) operating in a protective atmosphere of flowing argon was used to sinter samples for 1 hr. at 2000°C to achieve disks of greater densities. Bulk densities were 90 to 95% of theoretical with a significant amount of closed porosity.

Several yttria samples were hot pressed to achieve densities approaching the theoretical density. The hot pressing operation was carried out in a double acting graphite die with a 1 in. diameter x 3/4 in. sample cavity placed in a graphite-susceptor induction furnace. Densification was carried out at a temperature of 1600°C and held under a pressure of 3300 p.s.i. for 15 min. The samples were cooled after relief of pressure and extracted from the die at room temperature. It was not uncommon for the samples to fracture upon ejection from the die, consequently a considerable number of runs were required to produce an acceptable sample. The few resulting samples were black in color indicating partial reduction by contact with the graphite die. The samples were annealed

in air in a globar furnace at 1200°C for one week. Water immersion density measurements indicated the sample densities were greater than 99% of theoretical density.

A slip casting technique was used to fabricate several yttria disks. This method eliminated some of the disadvantages of the above two methods while retaining the high densities and conventional firing operation. The characterized yttria powder was dissolved in concentrated HCl and diluted to 5 gm. Y_2O_3 in 4N HCl/100 ml. solution. Ammonium hydroxide was used to precipitate the hydroxide which was subsequently calcined at 1100°C for 1 hr. The resulting oxide clinker was ball milled for 15 min. in 40 gm. batches with 13 ml. of solution containing 0.021 ml. "Darvan 7"/ml. distilled water. The slip was poured into a mold the shape of a 1/4 in. x 3/4 in. diameter disk and allowed to stand 1 min. The disks were prefired in air at 1000°C to develop handling strength and finally sintered in the Centorr furnace for 1 hr. at 1900°C. Measured bulk densities were greater than 97% of theoretical density.

Reprecipitation and recalcination of the initial oxide powder to the hydroxide and back to the oxide produced a more sinterable powder. This procedure produced new clean and active surfaces which enhanced sintering. Further justifica-

tion for this procedure is based on the investigations of Furlong and Domingues (82) in which the best sinterable powder of Y_2O_3 was obtained from calcination of the hydroxide. The method of slip casting yttria disks proved to be the most reproducible and desirable from the standpoint of density. In general the slip cast samples were very close to being translucent. Figure 2 illustrates the typical microstructures of the various Y_2O_3 samples used in this investigation.

Preparation of the Yttria Doped Hafnia Samples

Spectrographic grade hafnium oxychloride obtained from Wah Chang Corporation (Lot SP10684B) and the previously described yttria powder were the starting materials used in the preparation of the yttria-hafnia solid solutions. Spectrographic analysis supplied with the hafnium oxychloride is given in Table 2.

The hafnium oxychloride powder was dissolved in distilled water and the hafnium oxide content was determined analytically. The insoluble hafnium hydroxide precipitate was formed by pipetting 5 ml. of solution into an equal amount of 10N NH_4OH. The precipitate was filtered, washed, dried, and calcined at 1000°C in a Kanthal muffle furnace for 1 hr. The calcined product was weighed and the hafnium oxide content per

57

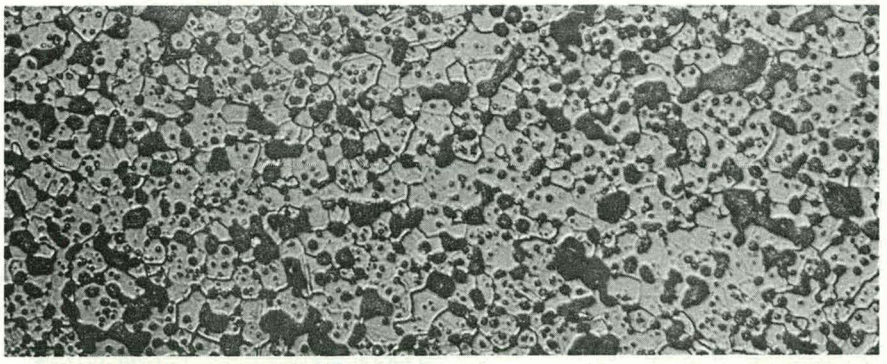

(a) Air induction fired; 400X

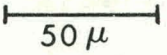

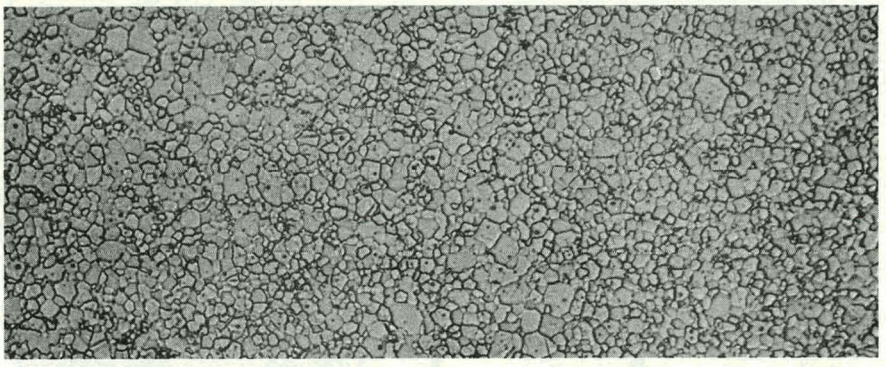

(b) Hot pressed; 400X

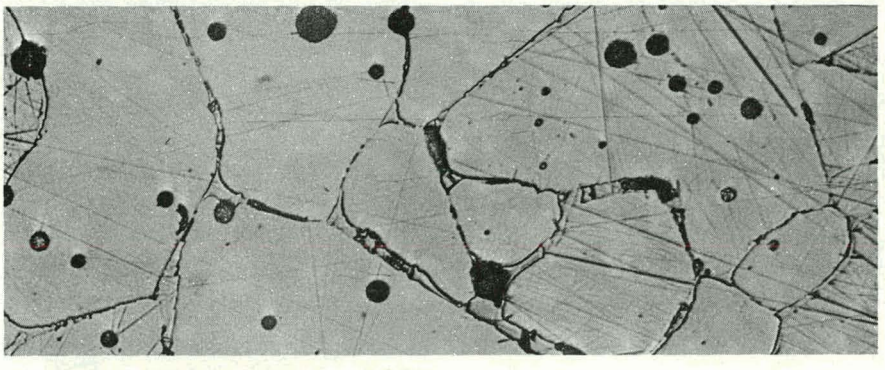

(c) Slip cast; 400X

Figure 2. Microstructures of Y_2O_3 samples

ml. of solution calculated. The standardization of the hafnia solution based on six determinations was 0.0958 gm. HfO_2/ml. solution.

Table 2. Spectrographic analysis of hafnium oxychloride spectrographic grade powder

Element	Concentration (ppm)
Al	<25
B	<0.2
Cb	<100
Cd	<1
Co	<5
Cr	<10
Cu	<40
Fe	<50
Mg	<10
Mn	<10
Mo	<10
Ni	<10
Pb	<5
Si	<40
Sn	<10
Ta	<200
Ti	<20
V	<5
W	<20
Zr	64
Total	635.2

The yttria powder was dissolved in hot concentrated HCl and then diluted with distilled water to produce a 4N HCl solution. An identical procedure previously described for the hafnia solution was used to standardize this solution which

was found to contain 0.0489 gm. Y_2O_3/ml. The two solutions were mixed in the required proportions to prepare the desired solid solution compositions. The mixed solution was slowly added to an equal volume of 10N NH_4OH. A magnetic stirrer kept the NH_4OH solution in constant agitation, during and for a short time after the addition of the mixed solution. The insoluble hydroxides of yttrium and hafnium formed a coprecipitate which was allowed to settle for 1 hr. The gelatinous nature of the coprecipitate seemed to eliminate any segregation. The coprecipitate was filtered, washed, dried, and calcined for 1 hr. at 1000°C.

The calcination temperature appeared to have a significant influence on the final sintered state. Dried precipitates were calcined at 600, 800, and 1000°C for various lengths of time. Those calcined at 1000°C possessed the highest sintered densities while those calcined at 600°C possessed the lowest sintered densities. Calcination times did not or were not controlled sufficiently to produce an observable effect on the sintered samples.

X-ray diffractometer traces of calcined compositions known to be within the single phase region indicated that the calcined material was a one phase fluorite solid solution. The diffraction peaks were quite broad as would be expected

from a very fine grained material and produced the typical face centered cubic pattern.

The calcined clinker was ground to -325 mesh with a Diamonite mortar and pestle (Diamonite Products Manufacturing Co., Shreve, Ohio). The powder was prepressed to 1800 p.s.i. in a 3/4 in. diameter tungsten carbide lined steel die. The green disks were then isostatically pressed to 50,000 p.s.i. All compositions were subjected to identical firing cycles in the Centorr furnace for 1 hr. at 2000°C and 30 min. at 1500°C. The lower temperature anneal was employed to stabilize the expected anion vacancies as demonstrated in the calcia-zirconia system (7). Disks of identical composition were placed in a covered yttria crucible and rhenium metal was used to separate the individual disks within the crucible. The hafnia solid solutions investigated, 2 to 20 m/o Y_2O_3 in 2 m/o intervals, were light brown in color after firing indicating partial reduction by the furnace atmosphere. Annealing the disks for several hours in air at 1000°C produced a color change to white. Water immersion bulk densities determined on the yttria-hafnia samples varied between 80 and 94% of theoretical density depending upon calcination temperature. Figure 3 shows the typical microstructure of an 8 m/o Y_2O_3 sample. Apparent densities used to identify the defect model were

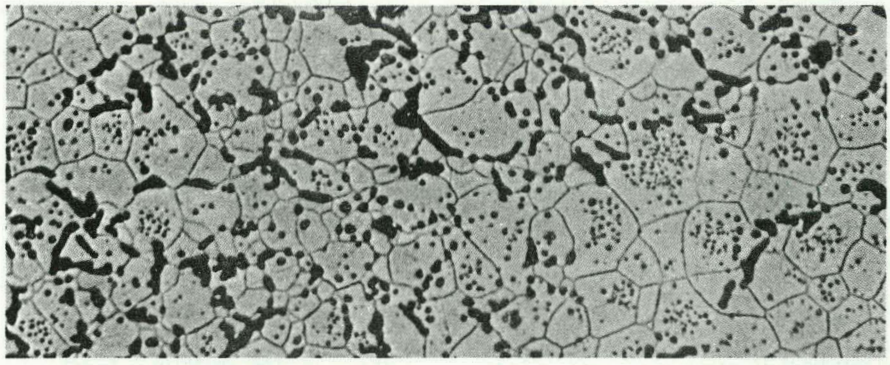

(a) 8 m/o Y_2O_3-92 m/o HfO_2; 400X — 50 μ

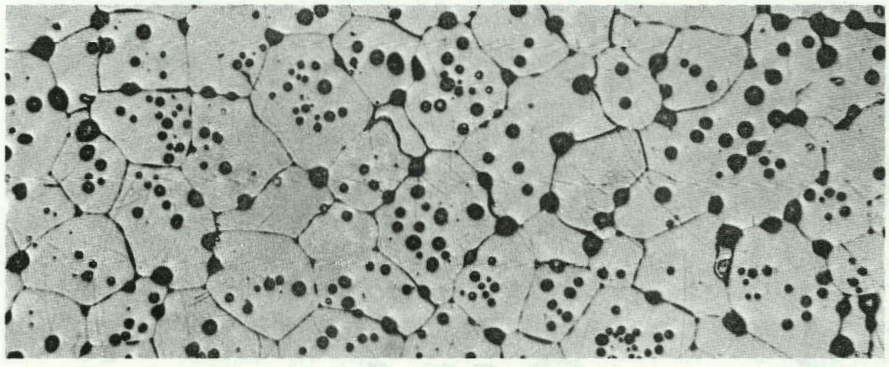

(b) 15 m/o CaO-85 m/o ZrO_2, commercial; 400X

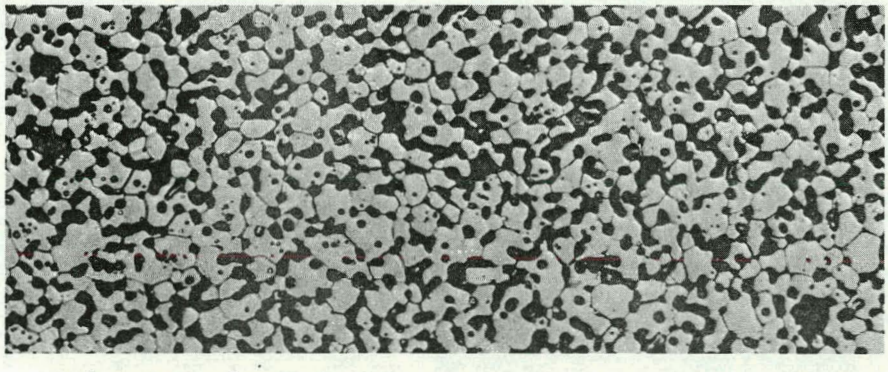

(c) 15 m/o CaO-85 m/o ZrO_2, nuclear grade powder; 400X

Figure 3. Microstructures of fluorite solid solutions

obtained from samples possessing low bulk densities in order to eliminate complications arising from closed porosity.

Both the undoped yttria and the yttria doped hafnia disk faces were ground parallel on a diamond wheel surface grinder. Hot pressed and slip cast Y_2O_3 samples required their cylindrical surfaces to be ground uniform in order to eliminate irregularities arising from the fabrication processes. This was accomplished by affixing the Y_2O_3 disks to a 1/2 in. drill stock with Loc-Wax-20 (Geoscience Instruments Corp., Mount Vernon, New York). The drill stock was then chucked into a small laboratory lathe which was attached to the bed of the surface grinder and a diamond wheel was used to grind the cylindrical surfaces smooth and uniform. The flat surfaces of each disk were further ground smooth on 600 grit SiC paper. All samples to be used for conductivity, open circuit emf, polarization, and x-ray studies were machined according to this procedure. General dimensions of the samples following this treatment were 15 to 19 mm. in diameter and 1.2 to 1.5 mm. thick. The exact dimensions were taken using a micrometer and measuring to the nearest 0.01 mm. Several undoped Y_2O_3 samples were ground thinner, 0.6 to 1.0 mm., to shorten equilibration times during experimental runs.

An x-ray analysis of the yttria-hafnia system was made to

determine the lattice parameter as a function of composition. A composition dependent lattice parameter would indicate a single phase region, while a composition independent lattice parameter would support evidence of a two phase region. YSH disks were analyzed before and after each conductivity run on a Norelco diffractometer using a copper tube at 40 kv and 20 ma with a Ni filter and a scanning rate of 1^{o} 2θ/min. Prior to the analysis the diffractometer was aligned and checked with a silicon standard. Lattice parameters were determined by Cohen's extrapolation method as modified by Vogel and Kempter (83). The monoclinic hafnia solid solution was identified by comparing the diffraction patterns with the monoclinic HfO_2 ASTM card. The fluorite structure of the YSH solid solutions was confirmed by comparing intensities and 2θ values to those obtained for erbia stabilized hafnia solid solutions which have been identified as possessing the calcium fluoride structure with anion vacancies according to Johnstone.[1]

---

[1]Johnstone, J. K., Ames Laboratory, Ames, Iowa. Structures of erbia-hafnia solid solutions. Private communication. 1970.

Experimental Apparatus for Cell Assemblies

The apparatus shown in Figure 4 was used for all electrical conductivity, open circuit emf, and polarization measurements. The cell assembly (A) was positioned above the alumina support tube (C). All ceramic parts of the apparatus were made of impervious alumina (McDanel AP35, McDanel Refractory Porcelain Co., Beaver Falls, Pa.) An alumina cap (B) which was connected to tension springs (L) located in the cool zone kept the cell under compression and helped maintain good electrical contact between various components of the cell. Four platinum leads (G) were available for electrode connections and entered the furnace through Fusite feed through connectors (M) (Fusite Corporation, Cincinnati, Ohio). Two additional leads were for the Pt vs. Pt, 10% Rh thermocouple (P) which was positioned inside the cap adjacent to the cell. The thermocouple was calibrated against a National Bureau of Standards thermocouple and checked in situ against the melting point of silver.

The alumina tube (E) was secured to the brass flange (J) with Apiezon wax forming an air tight chamber. The flange was water cooled by means of the copper cooling coil (H). Flanges (J) and (K) were bolted together and an O-ring seal prevented

THIS PAGE

WAS INTENTIONALLY

LEFT BLANK

Figure 4. Schematic diagram of experimental apparatus for electrical conductivity, open circuit emf and polarization studies

A. Cell assembly
B. Alumina cap
C. Alumina support tube
D. Alumina tube to control flow of controlled atmosphere
E. Outside alumina tube which forms gas tight enclosure
F. Grounded Inconel shield
G. Pt lead wires for cell connections
H. Water cooled Cu coils
I. Outlet valve for the system
J. Brass flange which is removable to load cells
K. Brass flange which remains stationary
L. Tension springs
M. Fusite feed through connections
N. Chromel-alumel control thermocouple
P. Pt-10%Rh, Pt temperature measuring thermocouple
Q. Marshall non-inductively wound, Nichrome element furnace
R. To gas purification train and Matheson Gas Proportioner
S. Veeco vacuum valve
T. To mechanical vacuum pump

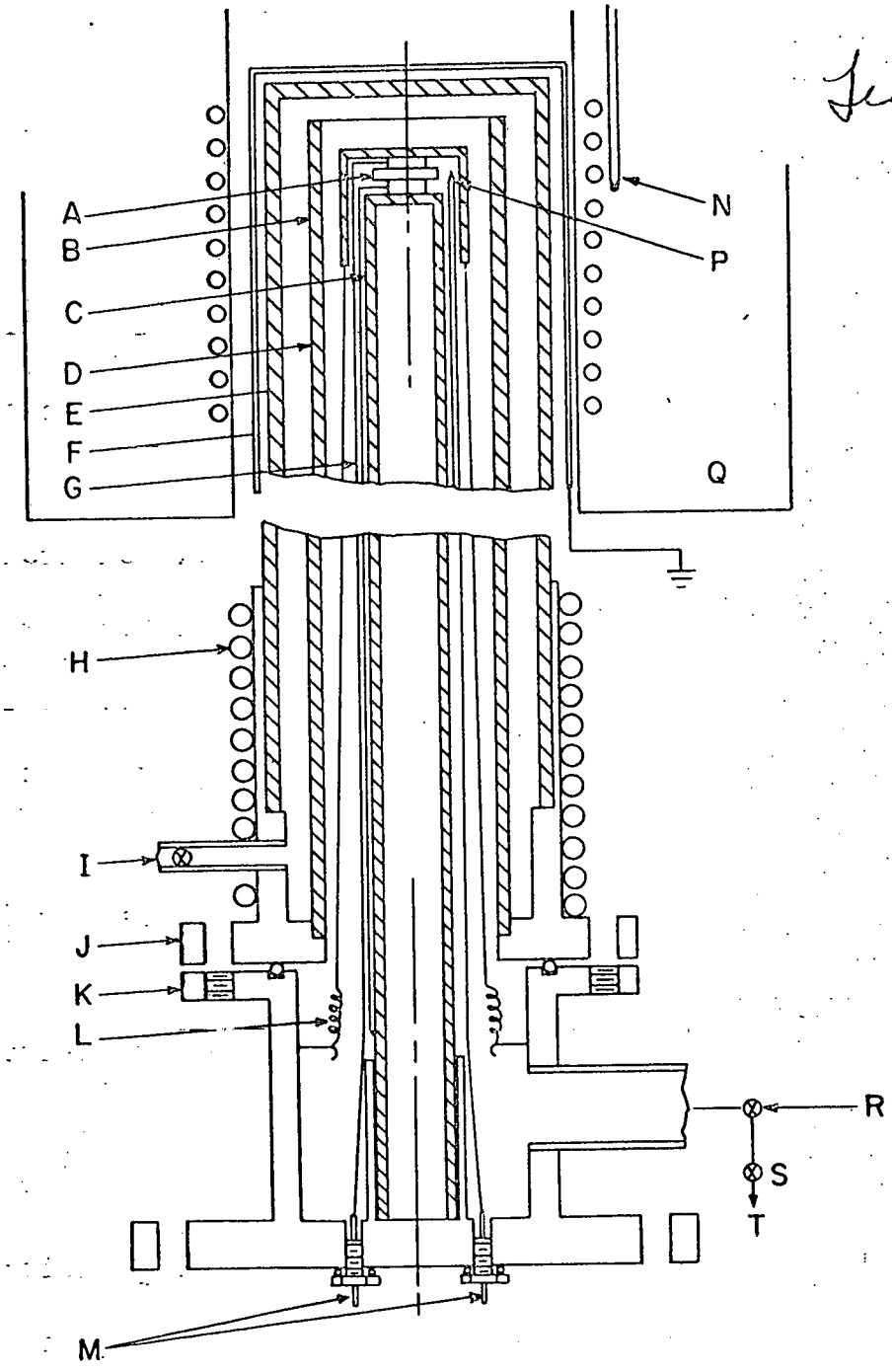

Fig 1

any gas leakage. An Inconel shield (F) was slipped down over the outside of alumina tube (E) and grounded. Its purpose was twofold; to eliminate induced voltages and to even out temperature gradients within the hot zone. The alumina tube (D) insured that controlled atmospheres flowed pass the cell assembly.

A Nichrome, noninductively wound, Marshall furnace (Q) was used to attain temperatures of 600 to 1000°C. Shunting of the external taps from the furnace winding was used to establish a uniform hot zone. A 2°C temperature gradient existed across a 3 in. hot zone as measured by a differential thermocouple. Since cell assemblies occupied only the middle inch of the hot zone, thermal gradients were expected to be negligible. This was confirmed by open circuit emf measurements of less than 1 mv. across CSZ between identical reversible electrodes.

The furnace was mounted on a metal guide so that it could be raised and rotated to one side. The assembly which included the flange (J) and alumina tubes (D) and (E) was lifted off the stationary flange (K) to allow access to the cell.

A West stepless silicon controlled rectifier in conjunction with a West proportional controller provided a temperature control of $\pm$ 1°C. The controller operated from the output

of a chromel-alumel thermocouple (N) located near the furnace windings.

Electrical leads were connected between the Pt furnace leads at the Fusite feed through connectors (M) and a central switch box. The inputs and outputs of the various measuring instruments were connected to a panel box. Connections between the two boxes allowed circuits to be constructed with a minimum of complication and a maximum in flexibility. All electrical leads were made with Teflon insulated, single conductor coaxial cable (Allied #55D9997, RG180 B/U, Allied Radio, Chicago, Ill.). All shields were grounded in such a manner that ground loops were kept to a minimum.

The system was evacuated through outlet (T) with a mechanical vacuum pump which could be isolated from the system by a Veeco vacuum valve (S). A controlled atmosphere was introduced into the system through (R) and exited through (I) into a mineral oil bubbler and finally exhausted out of the building through a laboratory hood. A picture of the experimental apparatus is shown in Figure 5.

Gas Handling System

Cell assemblies employing reversible metal-metal oxide electrodes were contained in an inert atmosphere of purified

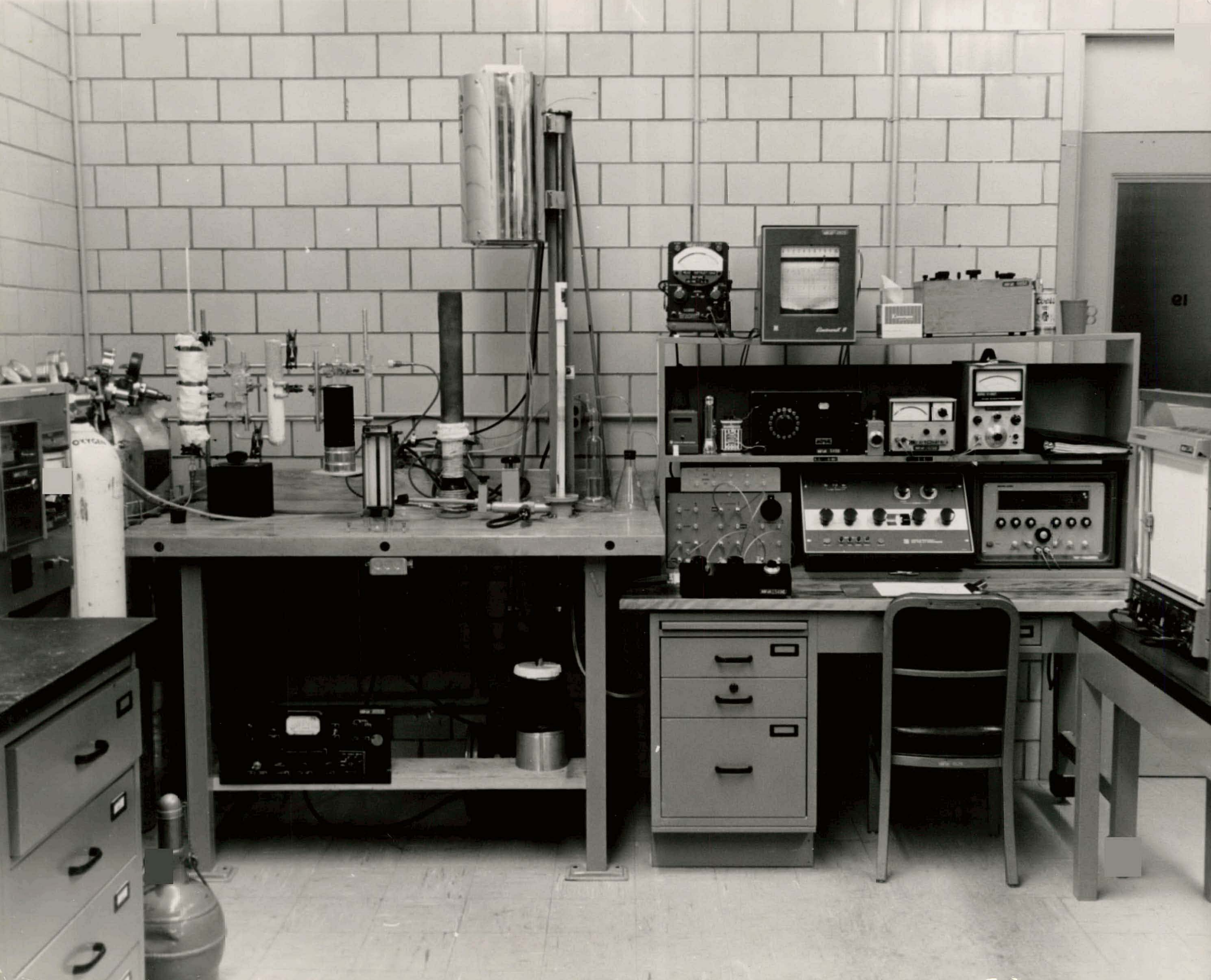

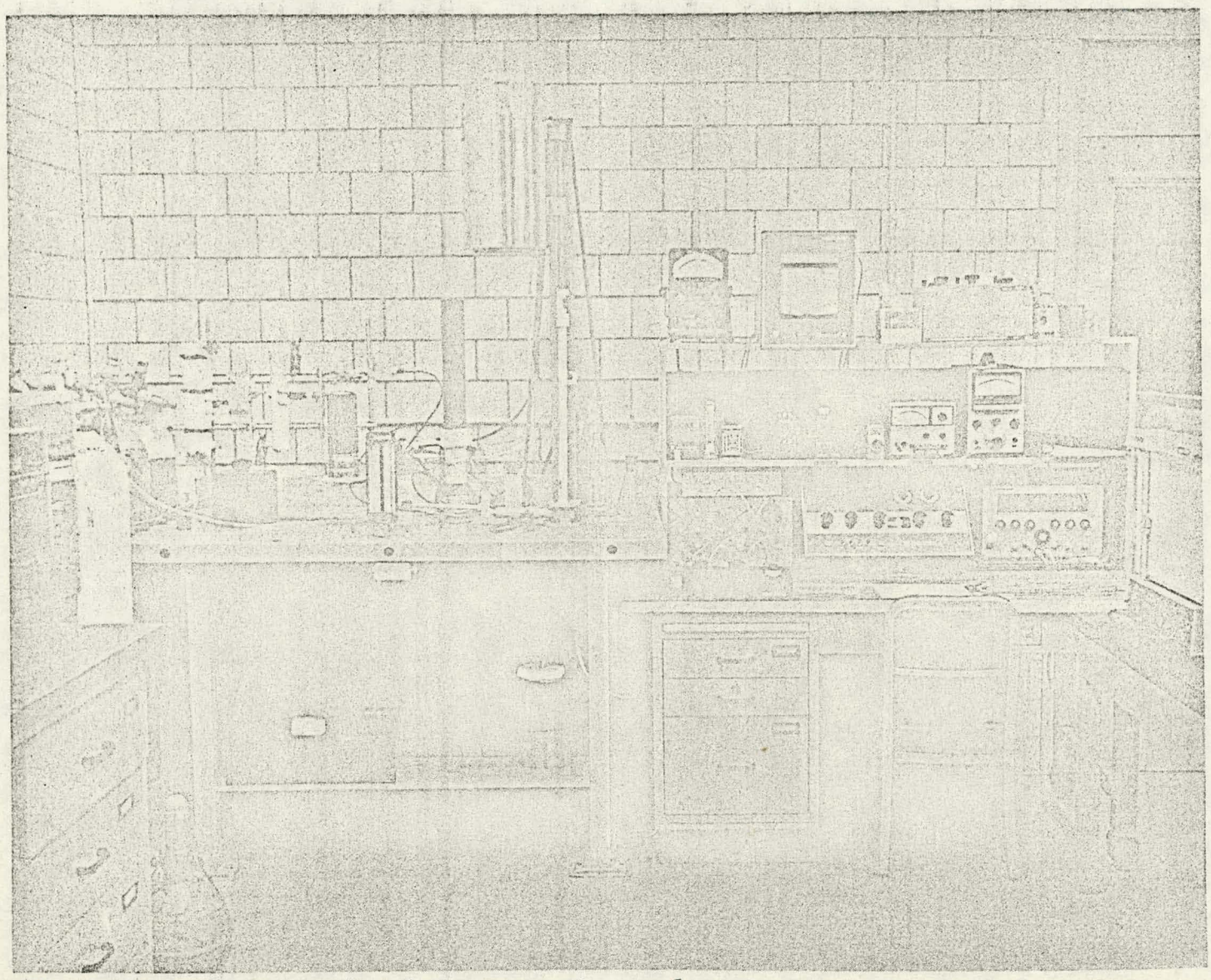

Figure 5. Photograph of the experimental area

helium. The tank helium was passed through a conventional gas purification train made of glass. The purification involved passing the gas through activated BTS Catalyst at 160°C; a mixture of activated alumina, Drierite, and Anhydrone; Ascarite; and a liquid nitrogen cold trap in that sequence. The glass purification train was connected to copper tubing by Cenco seals.

For controlled atmospheres of high oxygen pressures, dried tank oxygen, dried air, and He/O_2 ratios of 10 and 100 were used. The oxygen and air gases were dried by passing them through Drierite, Anhydrone, activated alumina, and Ascarite. The $He-O_2$ mixtures were obtained by passing the gases through a Matheson Gas Proportioner which permitted metering of the individual gases to make two component mixtures. The gas proportioner was used with Matheson flowmeter tubes 600, 601, and 610.

Low oxygen partial pressures were obtained from CO_2-CO mixtures based on the following dissociation reaction.

$$CO_2 \rightleftarrows CO + \tfrac{1}{2}O_2 \qquad (78)$$

The standard Gibbs free energy for this reaction (84) is given by

$$\Delta F_T = 68{,}270 + 0.13T(^{\circ}K)\ln T + 0.34\times10^{-3}T^2 - 0.87\times10^{5}T^{-1} - 23.28T. \qquad (79)$$

From equilibrium thermodynamics the oxygen partial pressure can be calculated from Equation 80.

$$\log P_{O_2} = 2\log \frac{P_{CO_2}}{P_{CO}} - \frac{2\Delta F_T}{2.3RT} \qquad (80)$$

if conditions are maintained so that the temperature is constant and known and the CO_2/CO ratio is constant and known. In this investigation, CO_2/CO ratios were varied between 100 and 0.1. The CO_2-CO mixtures were obtained by passing the two gases through the gas proportioner. Bone dry carbon dioxide and C.P. carbon monoxide were the grades of gases used in this investigation. The error in oxygen pressure due to impurities in the gases based on typical tank analyses was 0.3 of an order of magnitude in P_{O_2} for the worst possible ratio, consequently these gases were not purified.

Each flowmeter tube was calibrated for a particular gas by measuring the displacement of an air-water interface with time in a graduated cylinder for large flow rates (80 cc/min.) and a graduated burette for lower flow rates (5 cc/min.). Water heads of less than 6 in. were used in the calibration and the overall reproducibility of a particular setting was such that pressure corrections were neglected.

Open Circuit Emf Measurements

Open circuit emf measurements were made using dissimilar reversible metal-metal oxide electrodes with a cell of the type

$$Pt, M,MO/M_aO_b/M',M'O, Pt \qquad XIV$$

where M-MO and M'-M'O represent dissimilar electrodes and M_aO_b is either Y_2O_3 or YSH.

The metal-metal oxide mixtures for the electrodes were prepared to give a 10/1 molar ratio of metal to metal oxide at equilibrium. Powders were dry mixed and pressed in a 1/2 in. tungsten carbide lined die at 3000 p.s.i. and then isostatically pressed to 50,000 p.s.i. The electrodes were not sintered prior to fabrication of the cell; sintering occurred during the experimental run providing good tight interfaces between the electrode and oxide specimen and good electrical contact between the electrodes and the platinum lead wires. For low P_{O_2} runs, two zirconium getter buttons were placed above and below the cell. Figure 6 shows a picture of a typical emf cell construction employing the following cells

$$Co,CoO/Y_2O_3/Ni,NiO/Y_2O_3/Cu,Cu_2O. \qquad XV$$

Equilibrium oxygen activities for the reversible metal-metal oxide electrodes used in this investigation are listed in

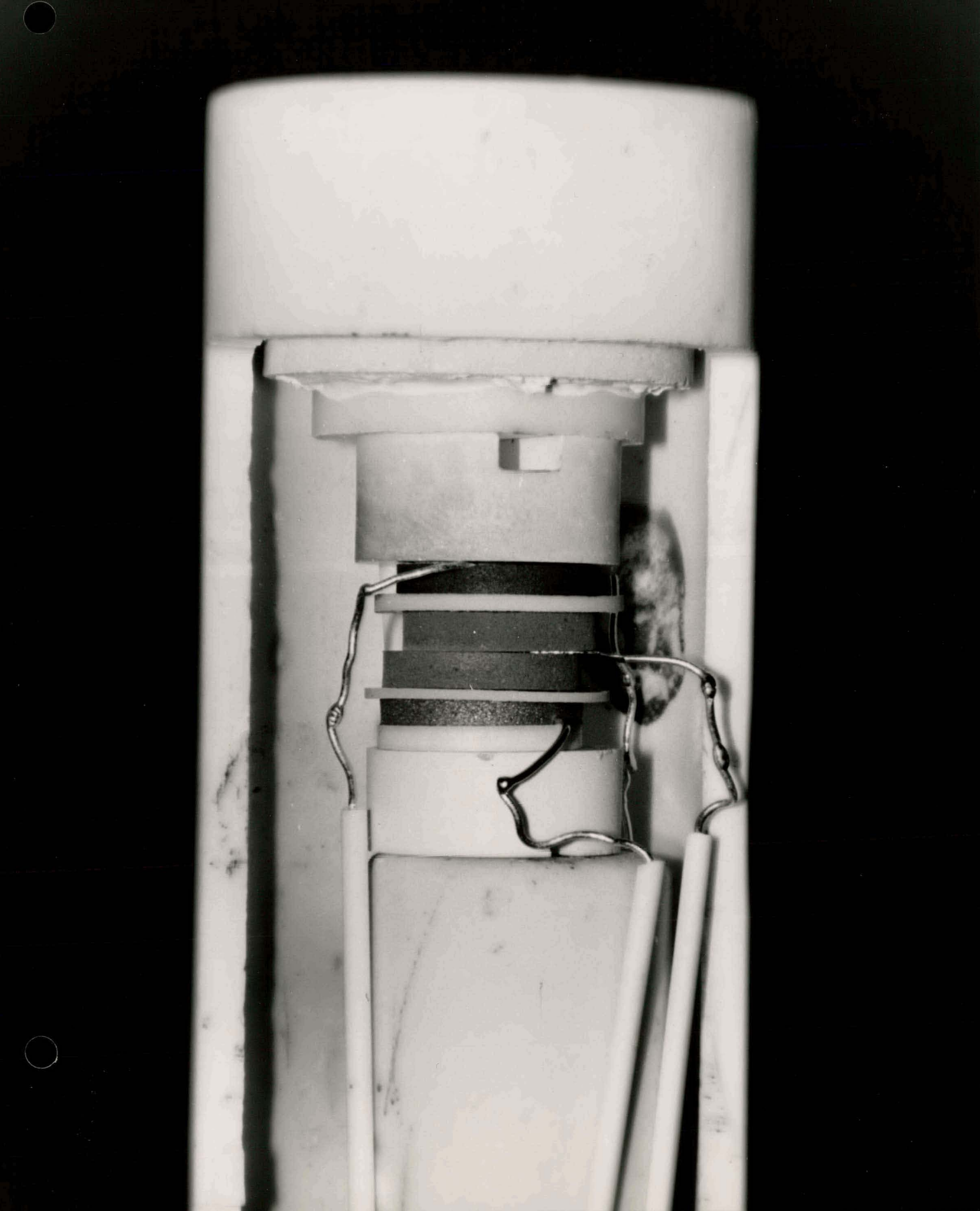

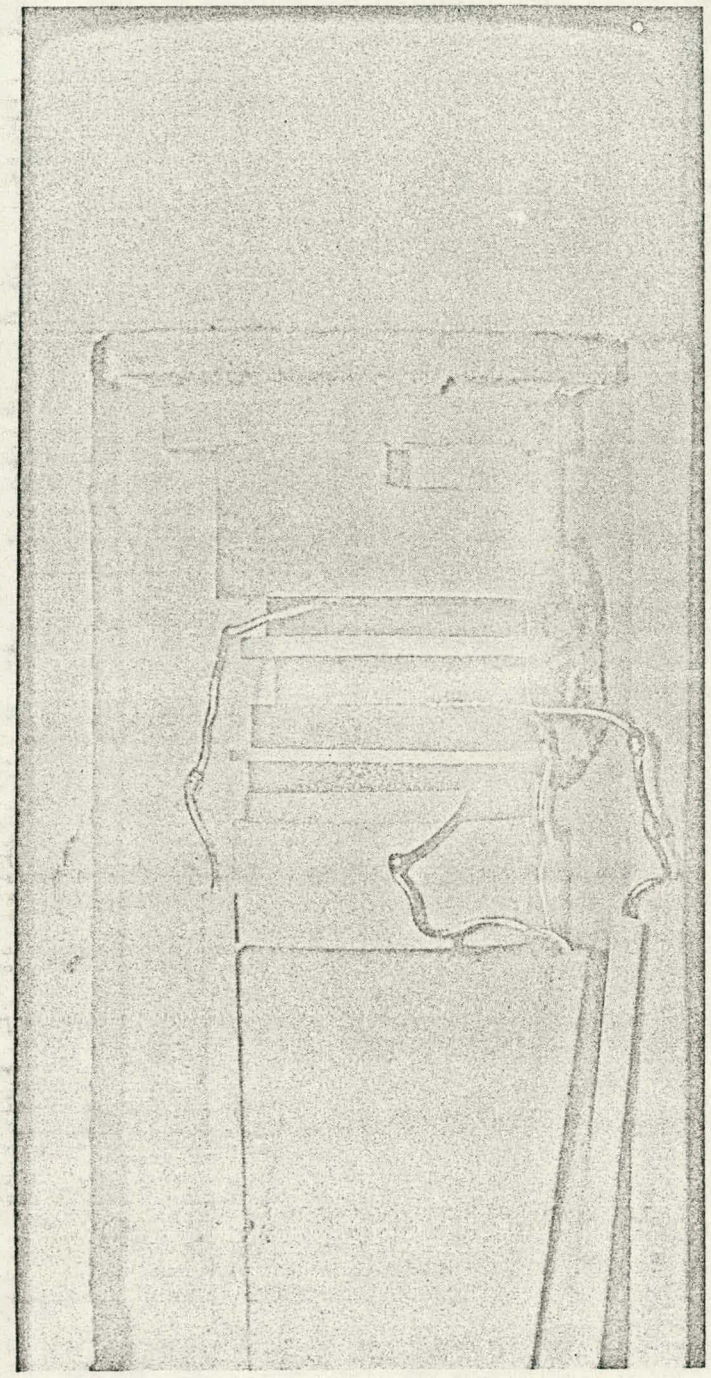

Figure 6. Photograph of a typical open circuit cell assembly

Table 3.

Table 3. Equilibrium oxygen activities for reversible electrodes

Electrode	Standard free energy change (Cal)	-Log P_{O_2} (Atm) at 1000°C	Reference
Cu_2O-CuO	-62,600 + 45.2T (°K)	0.87	85
Cu-Cu_2O	-79.850 + 34.2T	6.24	36
Ni-NiO	-111,930 + 40.6T	10.34	86
Co-CoO	-112,950 + 34.4T	11.88	4
Fe-FeO	-126,470 + 31.3T	14.88	86
NbO-NbO_2	-172,200 + 34.6T	22.00	31
Hf-HfO_2	-262,900 + 43.0T	35.74	84
Y-Y_2O_3	-279,500 + 48.1T	37.46	84

The cell assemblies were constructed outside of the furnace, transferred to the support tube, and placed under compression. Cell assemblies normally consisted of two identical cells. The platinum leads from the electrodes were welded to the platinum instrument leads to complete the electrical connections. All leads were checked for electrical continuity. The system was sealed and the furnace lowered into position. The system was evacuated by the fore-pump to ~20μ at a temperature of 200°C and held there for several hours. The system

was flushed twice and then finally filled with purified helium. The furnace temperature was increased to 1000°C placing the cell under a positive pressure. Static inert atmospheres were chosen because of convenience after verifying that measurements were independent of flow rates.

The cells were allowed to equilibrate at 1000°C. Open circuit emf measurements were made with a Leeds and Northrup 7554 Type K-4 potentiometer in conjunction with a Keithley 610B Electrometer employed as the null detector. The high input impedance (10^{14} ohms) of the electrometer prevented the cell from becoming polarized during the nulling operation. The same potentiometer with a Hewlett Packard 419A DC Null Voltmeter was used to measure the thermocouple output. The output of the electrometer was recorded with time to determine a steady state value. Honeywell Electronik 18 and 19 strip chart recorders and a Moseley Model 2DR X-Y recorder were used for this purpose. Equilibration times varied between 3 and 24 hrs. depending upon material and temperature. The temperature was lowered in 50°C increments and then recycled in equal increments back to 1000°C.

Problems arose in cells involving a low P_{O_2} electrode. Either the platinum lead wires became brittle and broke or

the high P_{O_2} electrode would reduce and/or the low P_{O_2} electrode would oxidize. The data per cell was greatly limited by the advent of these malfunctions.

D-c Polarization Measurements

Essentially the same procedure was followed for the polarization experiments. One of the reversible electrodes was replaced by a blocking electrode of gold. The gold was vapor deposited onto the oxide specimen and then backed with 5 mil gold foil. The reversible electrode was $Cu\text{-}Cu_2O$.

The d-c voltage was applied across the cell by means of a 6 volt battery and a voltage divider. The applied voltage was measured with a Systron Donner Digital Multimeter Model 7050. The current through the cell was determined by measuring the voltage drop with the K-4 potentiometer using the Hewlett Packard Voltmeter as the null detector across a 1K precision resistor which was in series with the cell. The null output was recorded with time to determine a steady state value. Measurements were taken at only two temperatures, 850 and 1000°C. Currents were measured for both increasing and decreasing applied voltages.

Electrical Conductivity Measurements

The construction of electrical conductivity cell assemblies with reversible metal-metal oxide electrodes is similar to that for the emf cells. In the case of controlled atmospheres, coatings of porous platinum paste (Englehard Industries, Inc., No. 232) were painted on the flat surfaces of the oxide specimens to serve as reversible electrodes with the atmosphere. Generally three coatings were required to produce a resistance of less than 0.5 ohm between any two points on the surface. Each coating was fired at 950 to 1000°C for a minimum of 1 hr. For 2 probe measurements the samples were backed with 1 mil platinum foil and the area was determined by measuring the specimen diameter with a micrometer. For 3 probe measurements (87) guard rings were formed by scraping away a portion of the platinum coating with a plastic template and a diamond stylus forming an insulated ring between the center electrode and the outer guard ring. This operation was done after the third platinum coating had been fired. A sample along with a piece of machined drill stock of known diameter were photographed together. Eight measured diameters of the center electrode obtained from a large print of the photograph were averaged and the area calculated from the mean

diameter. A typical 3 probe conductivity cell with an 8 m/o YSH sample is shown in Figure 7.

The a-c conductivity measurements were made with a Wayne-Kerr, Model 221, Universal bridge, which balances the conductance against standards of conductance and capacitance. The bridge measures the equivalent parallel conductance and capacitance of the samples and leads at a frequency of 1592 hz. Previous investigations on yttria (63) and rare earth oxides (65) indicated that conductances were independent of frequency above 100 hz, consequently the frequency was not varied in this investigation.

The system was outgassed at 200°C under vacuum. The flowing controlled atmosphere was introduced and the system heated to 1000°C. Conductances were measured periodically until there was a change of less than 1% in the reading over a period of an hour. The temperature cycling was identical to that described for the emf studies.

Since the conductivity was so high for the YSH samples, lead resistance corrections were required. To determine the lead resistance, two platinum leads contacted the porous platinum coating of one surface and a small voltage was impressed across the leads which were disconnected at the bridge. The voltage across the leads and across a precision

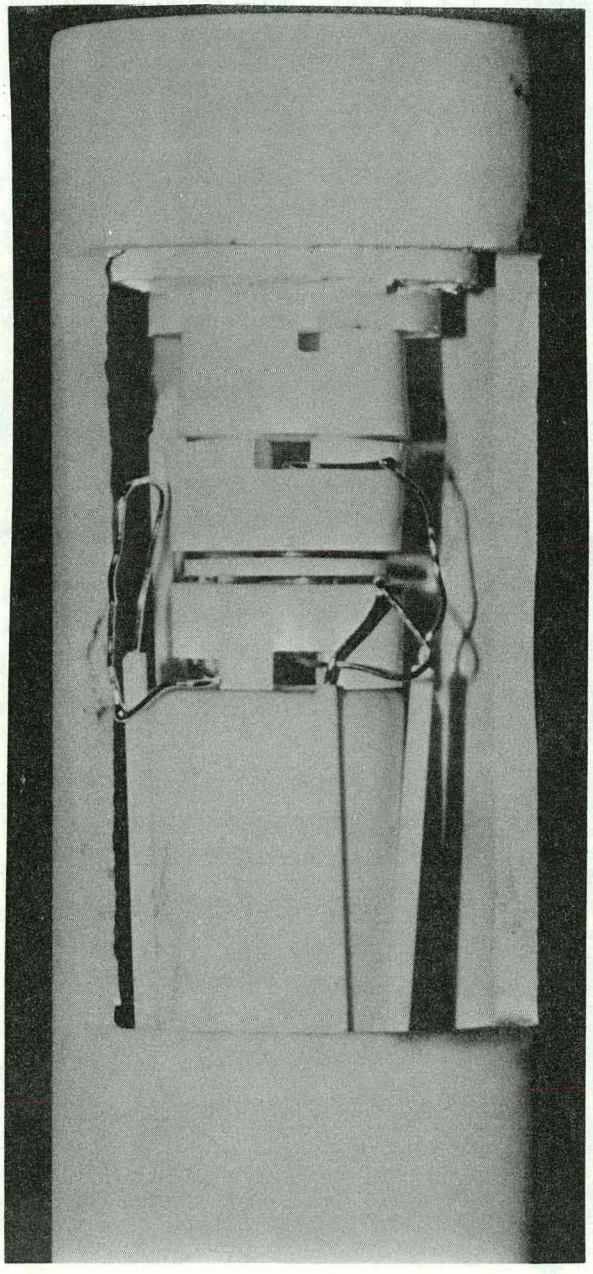

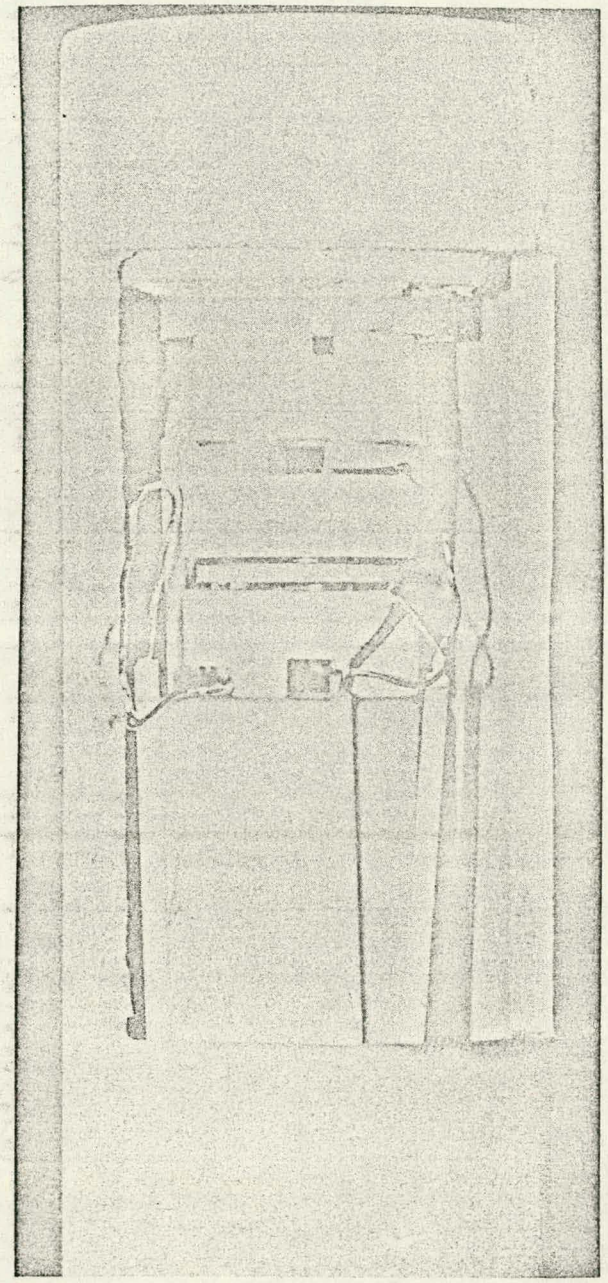

Figure 7. Photograph of a typical 3-probe electrical conductivity cell

resistor in series with the leads were measured with the K-4 potentiometer. A least squares fit of the data for five runs between 800 and 1000°C gave

$$R_L = 6.081 + 0.0013T(^{o}C) \pm 0.2. \qquad (81)$$

The lead resistance was added to the internal resistance of the bridge and the measured conductances were corrected as outlined in the operation manual for the bridge.

The conductance values were corrected for lead resistance where appropriate and multiplied by the thickness and divided by the cross sectional area of the electrodes to give the electrical conductivity of the sample.

Coulometric Titration-Open Circuit Emf Measurements

A new cell assembly was designed based on the combination of a polarization cell and two open circuit emf cells. Figure 8 is a schematic diagram of the coulometric titration-open circuit emf cell. A voltage was applied across a CSZ (15 m/o CaO) electrolyte between a metal-metal oxide electrode and a platinum screen. Since this portion of the cell constituted a polarization cell, changes in the applied voltage produced a change in the oxygen potential at the platinum screen interface. The metal-metal oxide electrode, CSZ electrolyte, and platinum screen formed a solid state ion pump and functioned

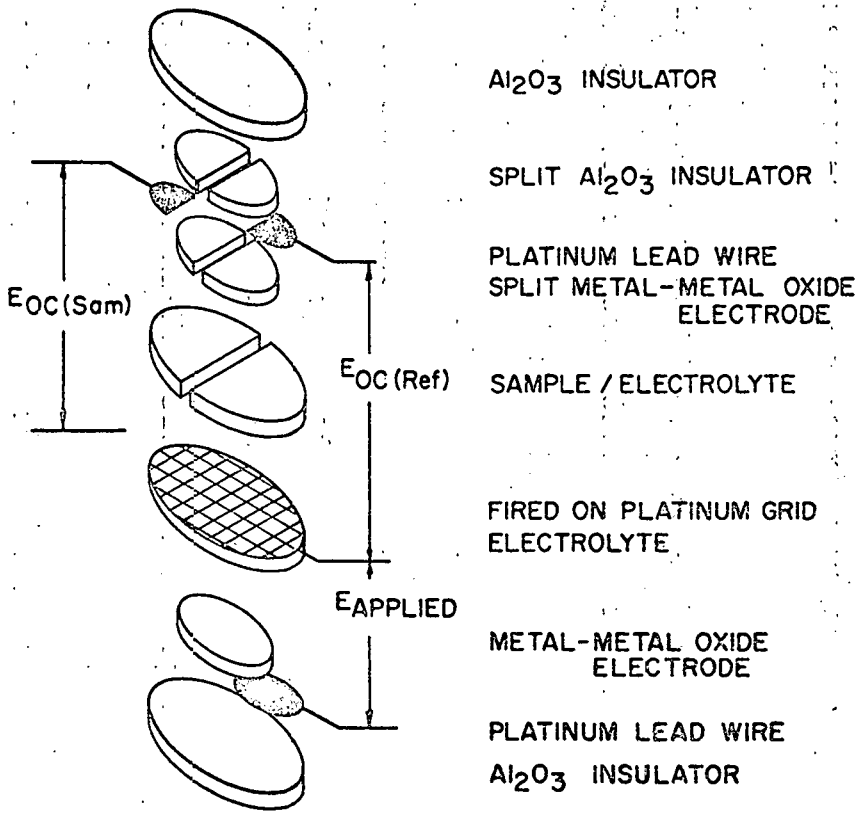

Figure 8. Schematic diagram of a coulometric titration-open circuit emf cell

as a variable P_{O_2} electrode. The upper portion of the assembly consisted of two open circuit emf cells. The cell employing the CSZ electrolyte served as a reference, its open circuit emf reflected the P_{O_2} set at the screen interface. The open circuit emf across the sample was compared to that across the electrolyte to determine the electrolytic behavior of the sample as a function of P_{O_2}. Application of this type of cell is limited to the electrolytic domain of the reference electrolyte.

Nuclear grade, -325 mesh, CSZ (15 m/o CaO) powder and impervious CSZ (15 m/o CaO) disks, 7/8 in. diameter and 1/8 in. thick, were purchased from Zircoa Corp. The powder was fabricated into 3/4 in. diameter by 1/8 in. thick disks according to the procedure outlined for pressing and firing the YSH samples. Both types of disks were verified as electrolytes by generating thermodynamic emfs when placed between Cu-Cu_2O, Fe-FeO, and Ni-NiO electrodes. Typical microstructures for both types of CSZ are shown in Figure 3.

The platinum screen was imbedded in the pump electrolyte surface. This surface was then ground flat to provide a flush contact with the adjoining surfaces of the emf cells. After the surface of the pump electrolyte had been ground flat with a diamond grinding wheel, one center groove of 20

mils and several 7 mil grooves were cut in a screen pattern into the surface with a diamond saw. A 20 mil platinum wire was placed into the center groove and served as an electrical lead. The grooves were completely filled with platinum by repeated applications of platinum paste. Finally the pump surface was ground smooth on 600 grit SiC paper.

The cell construction, initial heating, and open circuit emf measurements were identical to those for the simpler cells. The ion pump was operated similar to the polarization cells. Unexpected behavior was observed in that the applied voltage across the pump always exceeded the open circuit voltage across the reference electrolyte, the differences being as high as 100% in some instances. The behavior could be explained by internal ohmic resistance losses in the pump electrolyte and electrode and/or oxygen leakage at the common interface. At a constant temperature the desired P_{O_2} range was scanned by varying the applied voltage; the open circuit emf cells were allowed to equilibrate and the emfs recorded. Figure 9 is a picture of an actual coulometric titration-open circuit cell.

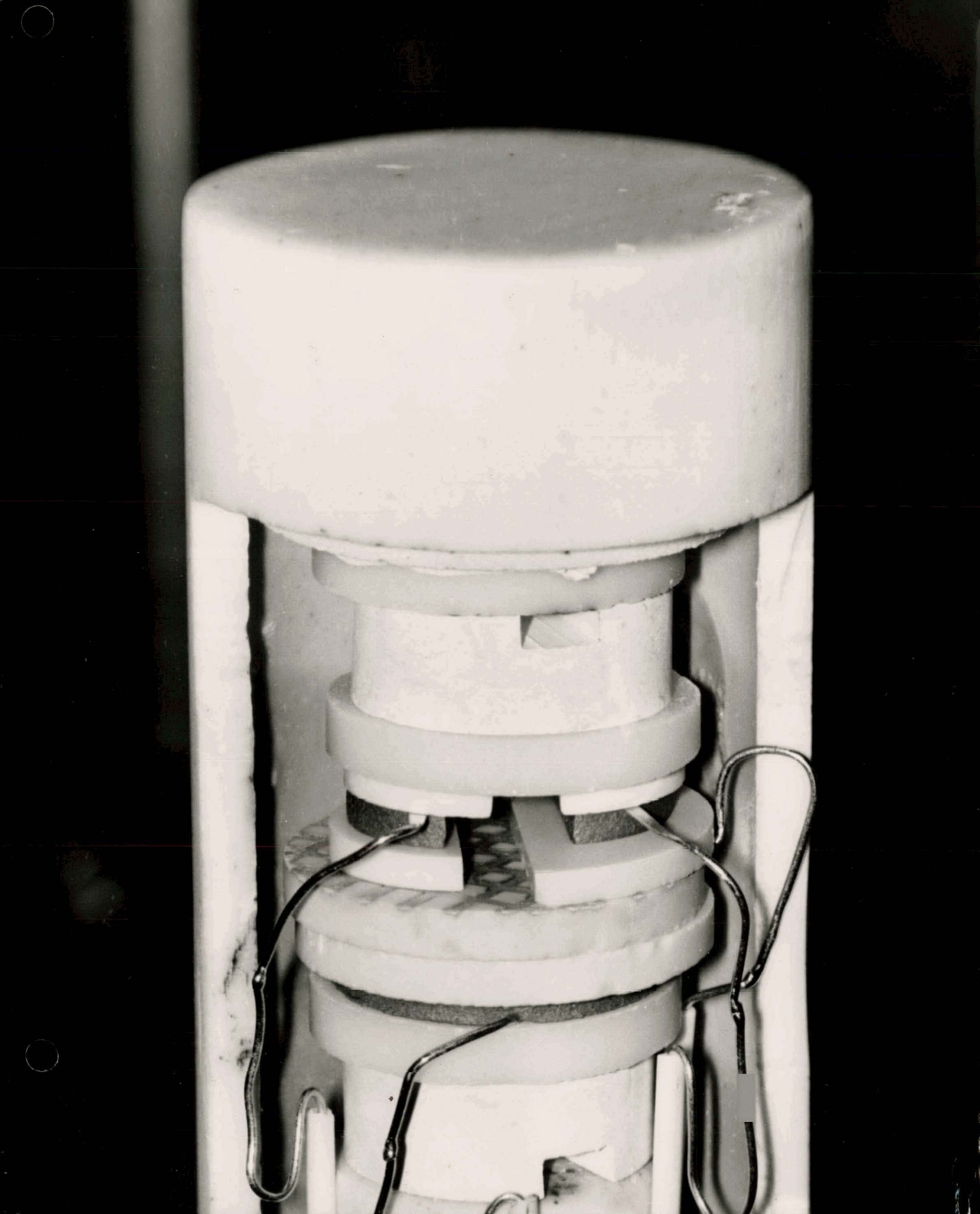

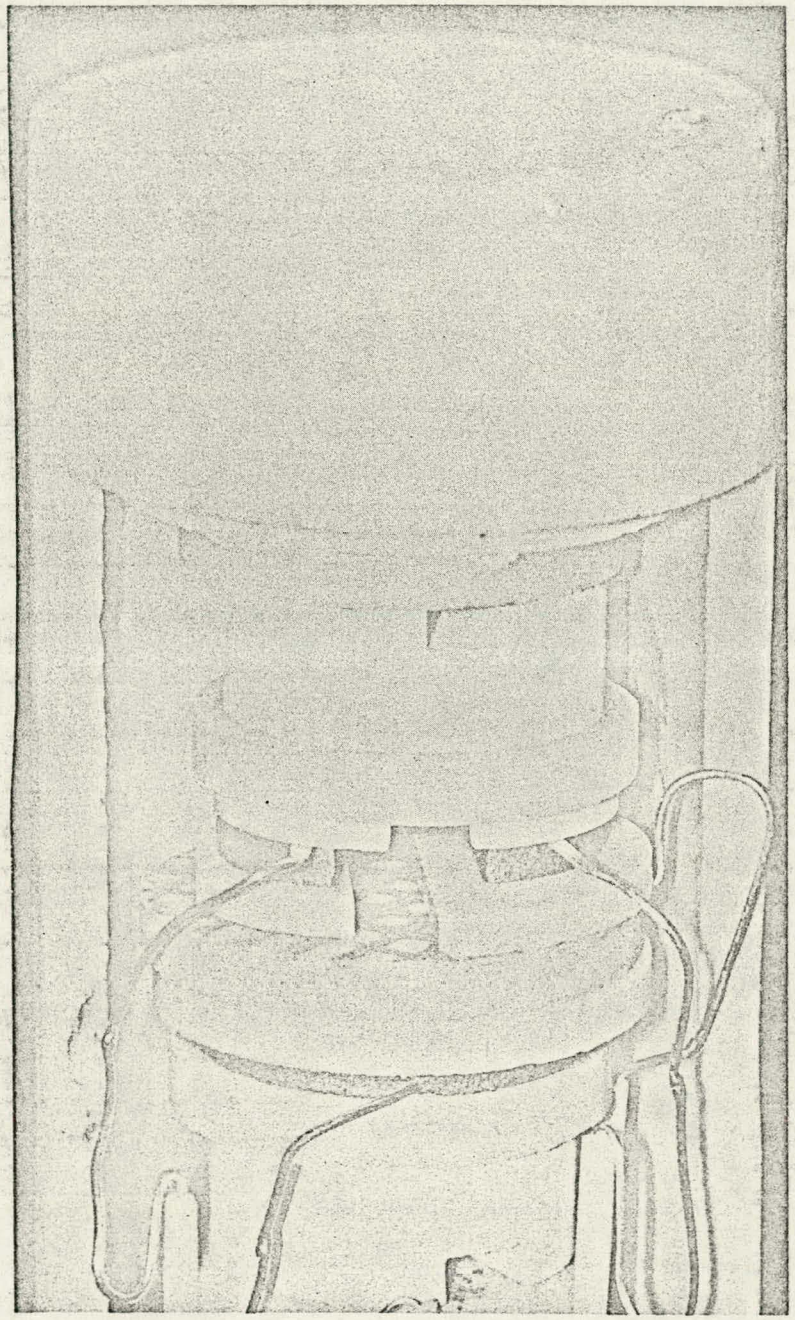

Figure 9. Photograph of an actual coulometric titration-open circuit emf cell

Solid State Oxygen Gage

A solid state oxygen gage was constructued to monitor the controlled atmospheres and check the calibration of the gas proportioner. The cell consisted of a reversible Cu-Cu_2O electrode that was sealed within a 3/8 in. I.D. by 1/2 in. tall CSZ (15 m/o CaO) crucible. Porous platinum served as the reversible gas electrode. The cell being

$$Cu,Cu_2O/CSZ\ crucible/O_2,Pt. \qquad XVI$$

The open circuit emf measured the oxygen potential in the atmosphere with respect to the oxygen potential as established by the Cu-Cu_2O reference equilibrium.

The gage was constructed by first firing several coatings of platinum paste on the outside bottom of the crucible. An unsintered 3/8 in. diameter Cu-Cu_2O disk which had been isostatically pressed was inserted into the crucible. A platinum lead lay across the top of the Cu-Cu_2O disk and exited from the crucible along a side wall. Another Cu-Cu_2O disk covered the lead and an impervious 1/2 in. by 1/4 in. diameter Al_2O_3 rod was set atop the disks. The Al_2O_3 rod protruded above the crucible and served as a push rod to keep force on the gage assembly.

The seal between the rod and crucible was most trouble-

some and the problem was never really solved. Of the many solutions attempted, the following proved the best but not really satisfactory. A zirconia castable (Zircoa Cast 28D, Zircoa Corp.) was forced down into the crucible between the side wall and rod. The castable was allowed to dry at room temperature and the joint coated with an impervious alumina cement (Ceramabond, Aremco Products, Inc.). The gage was positioned on top of the regular cell assemblies. As the Cu-Cu_2O disks sintered, the compressive force on the push rod caused the Cu-Cu_2O to deform producing an exceptionally tight interface with the electrolyte.

The data obtained from the gage during several conductivity runs is presented in Figure 10. The low oxygen pressure portion of the graph indicates that the gas proportioner was calibrated accurately within experimental error as shown by the span in data at a particular thermodynamic voltage. As expected the largest dispersion occurred at a CO_2/CO ratio of 100 (-228 mv.) where a small error in CO flow would significantly influence the oxygen partial pressure. At a ratio of 1 (-480 mv.), both flowtubes were operating in their optimum ranges as demonstrated by close grouping of the data points.

Oxygen partial pressures in purified helium were measured with the gage over a temperature range of 700 to 1000°C. As

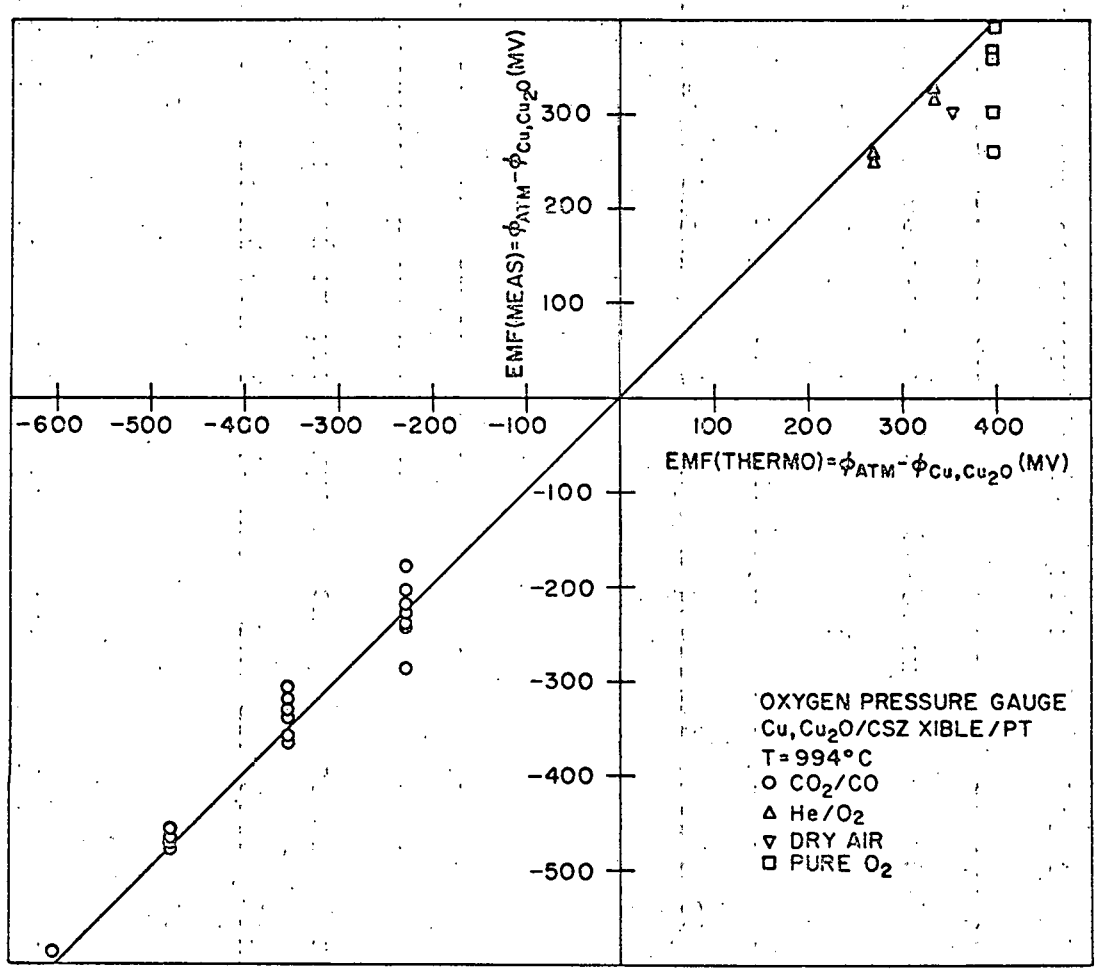

Figure 10. Comparison of the open circuit emf measured from the oxygen gauge with that computed for the input atmosphere

predicted by theory, the cell emf decreased with decreasing temperature and the oxygen pressure remained constant at 10^{-11} to 10^{-12} atm. The temperature behavior of the gage proved it was operating satisfactorily.

In the high oxygen pressure region of the graph (270-398 mv.), the data are considerably less reliable. For the He-O_2 mixtures the calibration does appear to be off but the error is tolerable when compared to the CO_2-CO mixtures. Cells operating in air and pure oxygen always failed and, more often than not, the data represented the highest emf prior to failure. After establishing a low oxygen pressure with a CO_2-CO mixture, pure oxygen or air was introduced into the system. Normally the emf reversed sign and started increasing to a peak value below the thermodynamic value for a minute or two and then decreased rapidly to zero. Two gages did generate the thermodynamic emf in pure oxygen, one gage survived for 3 hrs. while the second went for 24 hrs. The air data point and the four low pure oxygen data points were peak values during cell failure.

The failures resulted from the oxidation of the Cu-Cu_2O electrode which eliminated the required two phase equilibrium. Failures were traced to cracks in the seal between the Al_2O_3

rod and the crucible, and from cracks in the electrolyte crucible itself. In view of the fabrication problems, the failures were not unexpected.

Prior to failure, the gages responded nearly instantaneously to changes in oxygen pressures. Over-all gage response depended on the time constant of the gas system for handling the controlled atmospheres. For a CO_2/CO ratio of 100 this was approximately 15 min. Time constants for other controlled atmospheres were less.

RESULTS AND DISCUSSION

All the data reported in this investigation are presented in tabular form in the Appendices.

Electrical Conductivity of Undoped Yttria

The possibility of predominant ionic conductivity in Y_2O_3 was investigated by open circuit emf and electrical conductivity measurements. Conductivity isotherms as a function of P_{O_2} are shown in Figure 11.

Conductivities calculated from measured conductances based on individual length to area (L/A) ratios were scattered within an order of magnitude. Since Runs 2, 3, 4, 5, and 7 did produce a nearly identical 1000°C isotherm, this isotherm was used as a reference for correcting Runs 1, 6, 8, 9 and 10. A multiplying factor was calculated for each specimen (1,6,8, 9, and 10) to make their calculated conductivities agree with the 1000°C isotherm at one temperature and pressure (63). Descriptions of the electrical conductivity samples are given in Table 4. Runs 6, 9, and 10 required an upward shift to force the individual calculated conductivities to equal the isothermal conductivity. These runs employed porous platinum electrodes. Examination of the electrode-specimen interfaces

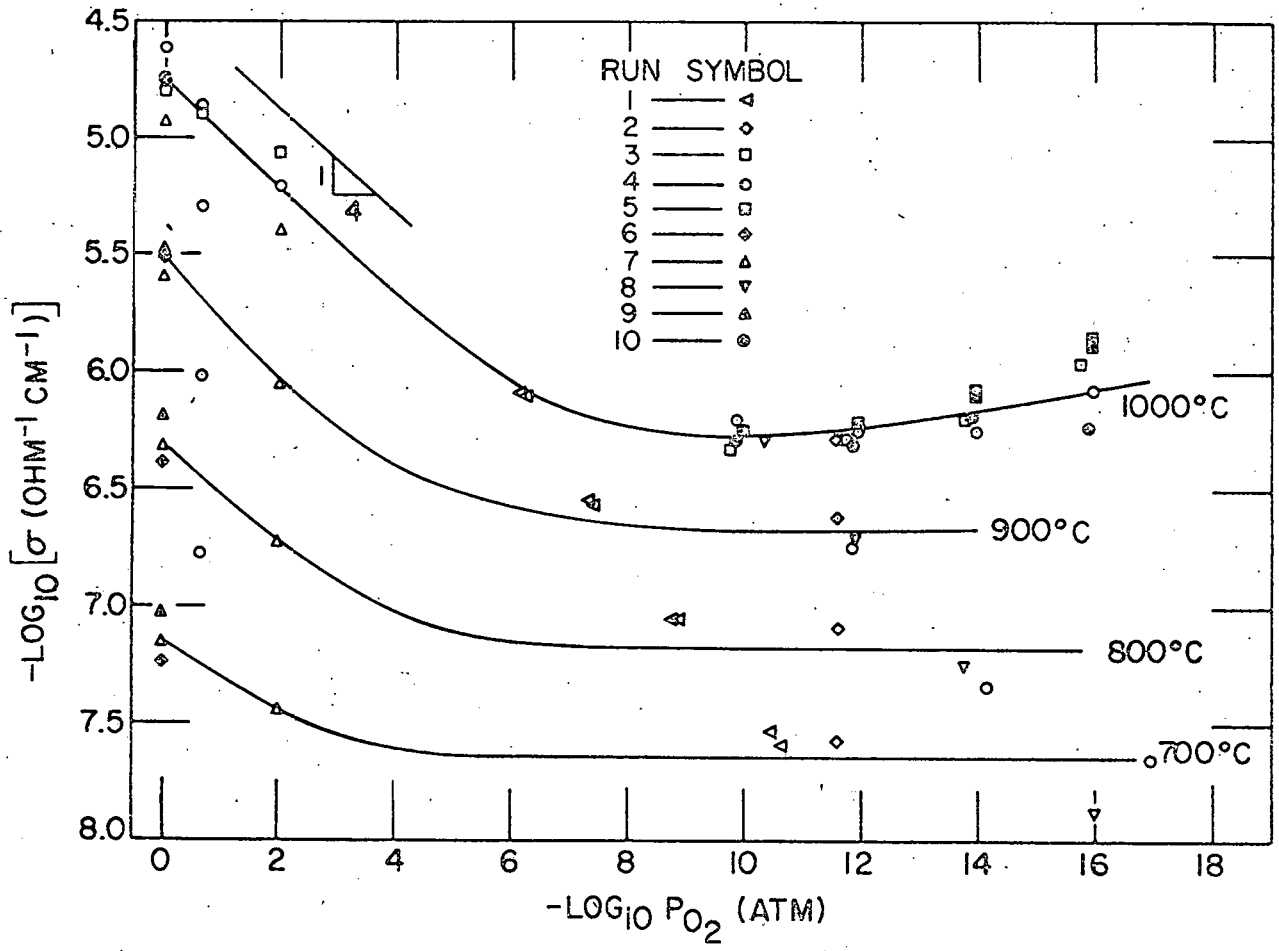

Figure 11. Electrical conductivity isotherms as a function of oxygen partial pressure for undoped Y_2O_3

following the run indicated that the electrode contact may have been questionable. The overall effect of this would be to decrease the original area, A, causing the conductivities calculated from the conductances to be too low. Thus the upward shift of the data for Runs 6, 9, and 10 does have some justification.

Table 4. Description of electrical conductivity samples

Sample	Electrodes	% Theoretical density	Fabrication
1	$Cu-Cu_2O$	79.2	Air induction
2	Porous Pt	98.5	Hot pressed
3	"	99.5	Hot pressed
4	"	80.2	Air induction
5	"	96.7	Slip cast
6	"	97.5	Slip cast
7	"	97.5	Slip cast
8	Ni-NiO	97+	Slip cast
9	Porous Pt	97+	Slip cast
10	"	98.5	Hot pressed

The opposite was true for the conductivity runs involving metal-metal oxide electrodes. Runs 1 and 8 required a downward shift in the data to match the 1000°C conductivity isotherm. Run 1 required a larger shift than Run 8. Justification for the shift is based on the sintering behavior of the electrodes. Since the metal-metal oxide electrodes had not been previously sintered, the original L/A ratios were

obtained from an unsintered compact. As the temperature increased, the electrode materials sintered and flowed under pressure increasing their area. The Cu-Cu_2O electrode showed a greater increase in area than the Ni-NiO electrode which necessitated the larger downward shift of the data for the run with Cu-Cu_2O electrodes.

Samples 3 and 5 possessed almost no porosity, while Sample 4 contained 20% porosity. Sample 3 was hot pressed and possessed a very fine grain structure while Sample 5 was slip cast and possessed enormous grains (Figure 2). One of the surprising observations was the lack of grain boundary and porosity effects, since Runs 3, 4, and 5 produced identical results. There is no explanation as to why these effects were not observed.

The high oxygen pressure data do indicate the presence of an oxygen pressure dependent conductivity. A least-squares analysis of 9 high oxygen pressure points at 1000°C gave a slope of 0.228 ± 0.11 which is very close to the +1/4 P_{O_2} dependence for hole conduction predicted by the following equilibrium:

$$\tfrac{1}{2}O_2 \rightleftharpoons O_i'' + 2\oplus \qquad (31)$$

where the $[O_i'']$ is fixed by the impurity content. This appears reasonable since the impurity content of the undoped

Y_2O_3 (Table 1) is sufficiently high to control the conductivity.

The apparent activation energy for hole conduction was 47.9 kcal/mole as determined from an Arrhenius plot of the data for pure oxygen between 700 and 1000°C. This value agrees favorably with 44.7 kcal/mole obtained by Tallan and Vest (63) and 43.8 kcal/mole obtained by Subbarao et al. (9). The positive hole conductivity can be represented by the following expression:

$$\sigma_{\oplus} = 2.8\times10^{3}\ P_{O_2}^{\frac{1}{4}}\ \exp(-47{,}900/RT)\ \text{ohm}^{-1}\ \text{cm}^{-1}. \qquad (82)$$

The scatter in the data is such that no specific defect equilibrium can be confirmed. In fact, the pressure dependence of the conductivity is actually between that predicted by the fully ionized oxygen interstitial model and the defect model proposed by Tallan and Vest (63). In the latter proposal, the hole conductivity arises from fully ionized cation vacancies as follows:

$$\tfrac{1}{2}O_2 \rightleftharpoons O_O^x + 2/3\ V_Y^{'''} + 2\oplus. \qquad (83)$$

It is interesting to note that the hole conductivity expression of Tallan and Vest (63)

$$\sigma_{\oplus} = 1.3\times10^{3}\ P_{O_2}^{3/16}\ \exp(-44{,}700/RT)\ \text{ohm}^{-1}\ \text{cm}^{-1} \qquad (84)$$

is very similar to Equation 82.

At lower oxygen pressures, the conductivity isotherms show an oxygen pressure independent conductivity, suggesting the presence of ionic conduction. This is consistent with other investigations (9,63) which detected the presence of ionic conduction under similar conditions of temperature and oxygen pressure. The 1000°C isotherm shows a slight pressure dependent conductivity at very low oxygen pressures, possibly indicating the onset of excess electron conductivity. If so, the ionic plateau is very narrow at 1000°C. Data from the lower temperature isotherms at low oxygen pressures are too limited to yield to any interpretation.

An activation energy calculated for ionic conduction at a constant oxygen pressure defined by the minimum in the 1000°C isotherm (log P_{O_2} = -9.5) was 27.9 kcal/mole. This value is higher than that reported by Berard et al. (75) of 19.6 kcal/mole for oxygen ion diffusion and much less than 69.2 kcal/mole for cation diffusion. Although good agreement is lacking, it is assumed that the ionic conductivity results from oxygen ion migration as predicted by the chosen defect model. The ionic conductivity can be expressed as:

$$\sigma_{ion} = 3.17 \times 10^{-2} \exp(-27{,}900/RT) \text{ ohm}^{-1} \text{ cm}^{-1}. \qquad (85)$$

In summary, undoped yttria exhibits a pressure dependent conductivity at high oxygen pressures which can be associated with electronic defects, i.e. positive holes. At lower oxygen pressures, the presence of ionic conduction is suggested by the appearance of an oxygen pressure independent conductivity. These conclusions are of a general nature since the data are somewhat scattered due to stray conductances as high as 10% of the measured sample conductances.

Open Circuit Emf Measurements on Undoped Yttria

Open circuit emf measurements were made to verify the presence of predominantly ionic conduction in Y_2O_3 as suggested by the electrical conductivity study. The raw data obtained from three different types of cells are presented in Figure 12. A Ni-NiO electrode was chosen as the reference electrode based on limited data from initial runs. These runs indicated that the Ni-NiO equilibrium defined a P_{O_2} that was centered within the presumed ionic domain of yttria. Fe-FeO was eliminated as a possible electrode material since it reacted with Y_2O_3 to form the compound $YFeO_3$. Co-CoO was also tried as a reference electrode, however it functioned worse than Ni-NiO as shown in Figure 12 by the scatter in the data for the cell

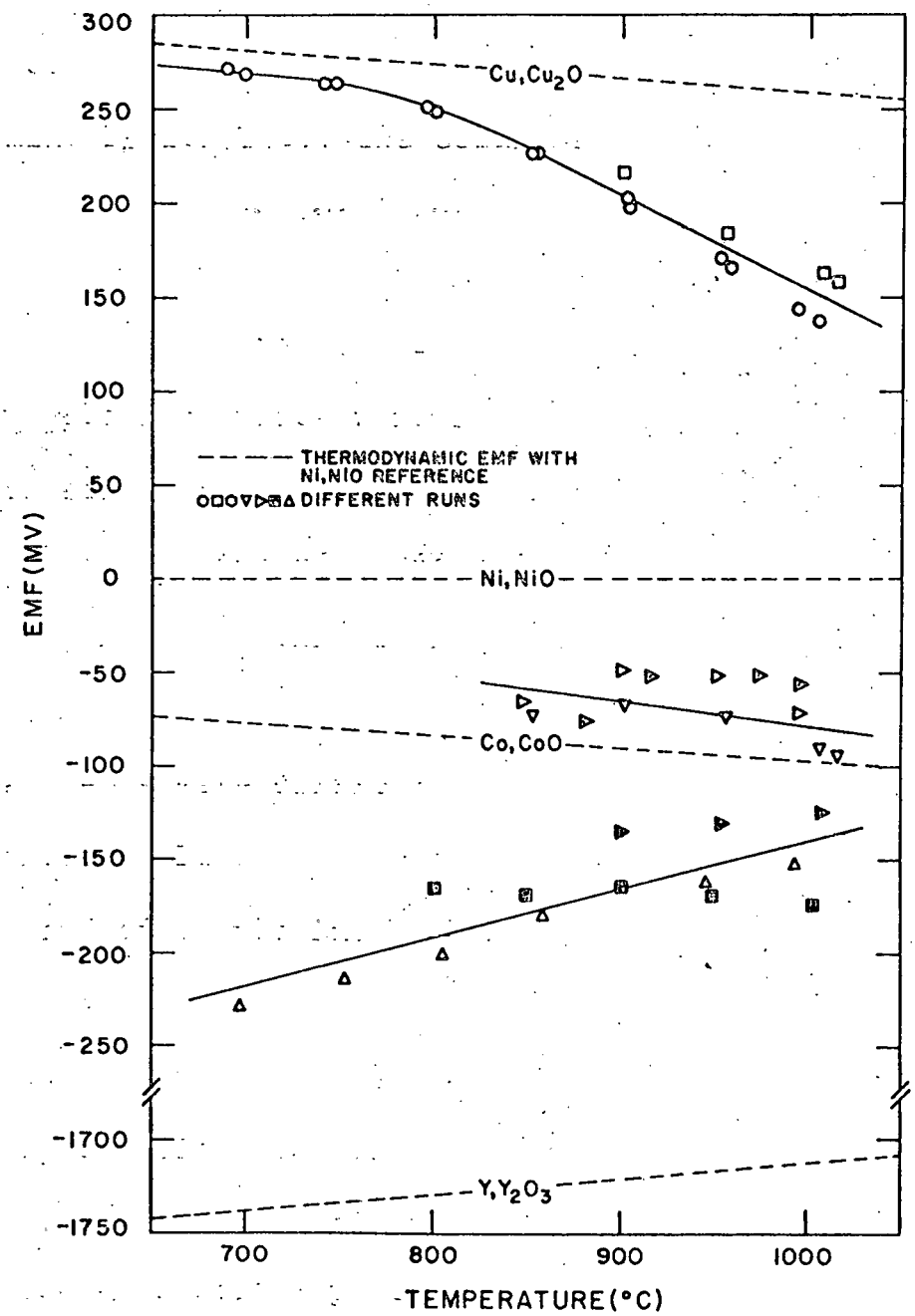

Figure 12. Open circuit emf data for undoped Y_2O_3

$$Ni,NiO/Y_2O_3/Co,CoO. \qquad XVII$$

Post run examination of these cells generally indicated that failures could be traced to oxidation of the Co in the Co-CoO electrodes.

The cells using a low P_{O_2} $Y\text{-}Y_2O_3$ electrode were employed to determine P_θ for Y_2O_3, the cells being

$$Ni,NiO/Y_2O_3/Y,Y_2O_3 \qquad XVIII$$

and

$$Co,CoO/Y_2O_3/Y,Y_2O_3 \; . \qquad XIX$$

One or two platinum wires were spot welded to an yttrium metal disk which served as an electrical lead connection. Since the electrode-specimen interface formed the required two phase equilibrium, moderate oxidation of the yttrium metal was not detrimental to the cell.

Steady emfs were difficult to obtain in cells using low P_{O_2} electrodes. Electrical contacts frequently lost their integrity and often platinum embrittlement resulted in premature termination of the runs due to a break in an electrical lead. Another serious problem arose since electrodes were not isolated by gas tight compartments, consequently many of the runs were terminated by failure of an electrode to maintain a fixed oxygen potential. This was particularly true for cells

with large gradients in oxygen chemical potential. In the case of Cells XVIII and XIX, the presence of zirconium getter disks further promoted failure of the reference electrodes, even though the exposed surface of the electrodes was coated with Ceramabond.

The third type of cell

$$Ni,NiO/Y_2O_3/Cu,Cu_2O \qquad XX$$

produced some very interesting results as shown in Figure 12. Below 800°C the open circuit emf almost paralleled the thermodynamic emf based on Cu-Cu_2O equilibrium, while above 800°C the measured emfs gradually decreased with respect to the thermodynamic values. Within the temperature range of 700 to 1000°C, this behavior strongly indicated that $P_{\oplus} \approx P_{O_2}(Cu, Cu_2O)$ and, in fact, that $P_{\oplus}$ crossed the $P_{O_2}(Cu,Cu_2O)$ line. This behavior did establish that the measured emfs resulted from the Y_2O_3 specimen and not from spurious effects within the furnace.

Equations 68 and 69 were used to determine rough approximations of $P_{\oplus}$ and $P_{\ominus}$. In the case of $P_{\oplus}$, the results were extremely misleading. Although the resulting plot of log $P_{\oplus}$ vs 1/T was linear as predicted by the conduction domain theory, it exhibited a negative slope. Such a negative slope

implies that $Q_{ion} > Q_{\oplus}$ which is difficult to justify. Consequently, Equation 69 could not be used for even a rough estimate of $P_{\oplus}$ since the necessary approximations were not valid. On the other hand, Equation 68 did provide a reliable first order approximation of $P_{\ominus}$ and this represented the starting point for evaluating the open circuit emf data.

The values of $P_{\ominus}$ determined from Equation 68 were inserted into a computer program which represented Schmalzried's most general solution, Equation 60, and $P_{\oplus}$ was allowed to vary until the calculated emfs of the program matched the observed emfs of Cell XX. These values of $P_{\oplus}$ were then inserted into the program and $P_{\ominus}$ was allowed to vary until the calculated emfs matched the observed emfs of Cells XVIII and XIX. The above iteration process was repeated until there was less than a 0.1 change in log $P_{\oplus}$ and log $P_{\ominus}$ compared with the previous cycle.

As predicted by the conduction domain theory, a plot of log $P_{\oplus}$ and/or log $P_{\ominus}$ vs 1/T is linear. Figure 13 shows such a plot for undoped Y_2O_3. The ionic domain boundaries can be expressed as:

$$\log P_{\oplus} = \frac{11030}{T(^{o}K)} - 15.84 \qquad (86)$$

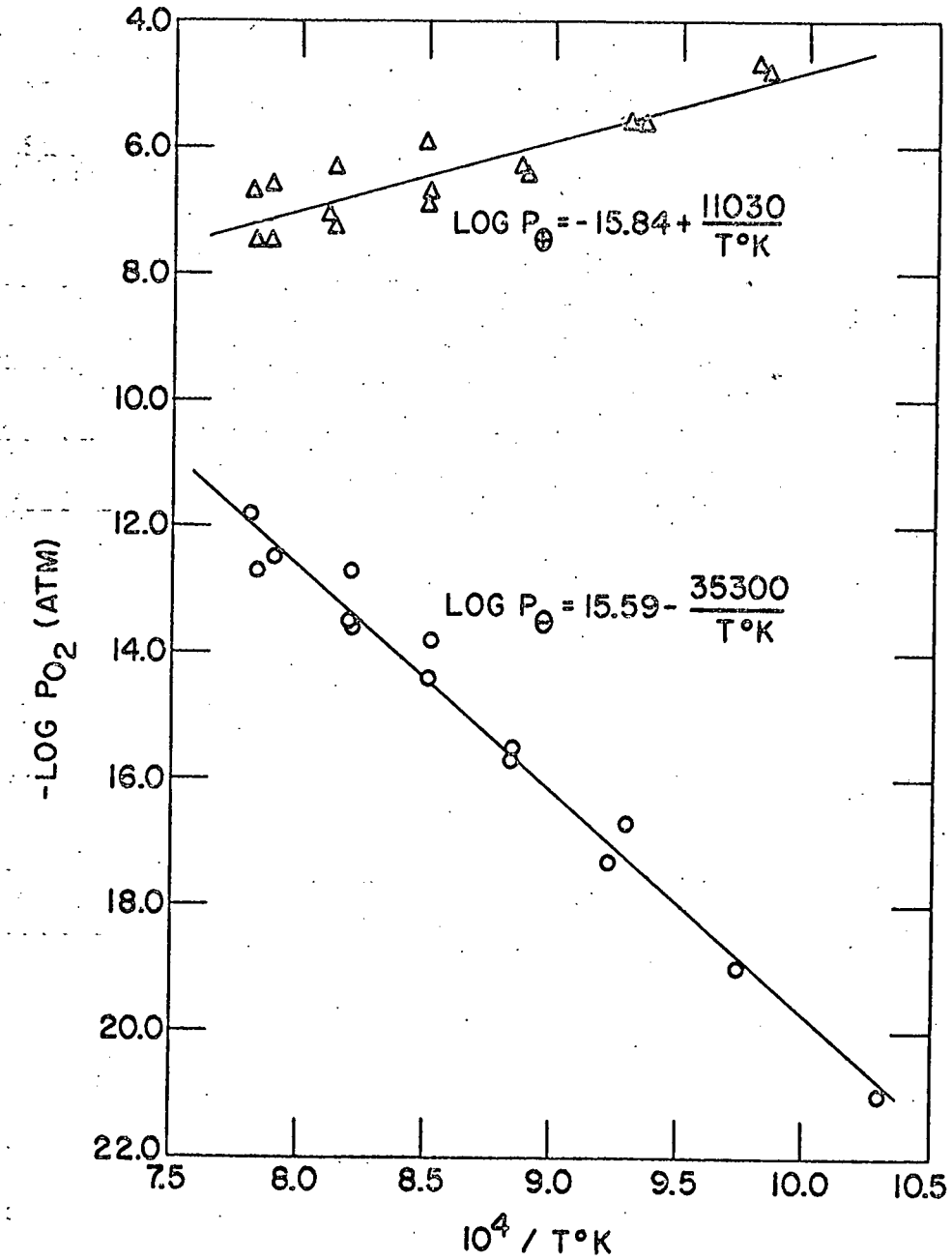

Figure 13. Ionic domain boundaries for undoped Y_2O_3

$$\log P_\theta = \frac{-35300}{T(^\circ K)} + 15.59. \qquad (87)$$

Further analysis of Equations 86 and 87 to obtain activation energies will be deferred until the open circuit emf and the electrical conductivity data are compared.

Since the chosen defect model requires that n = 4, a displacement of 8 (2n) is required to locate the electrolytic domain boundaries with respect to the ionic domain boundaries according to Equations 27. Such a translation shows that, within the experimental temperature range, there is no electrolytic domain for undoped Y_2O_3. However, based on extrapolations of Equations 86 and 87, an electrolytic domain for Y_2O_3 is indicated at lower temperatures.

The solid state oxygen gage described by McPheeters et al. (67) for measuring oxygen contamination in liquid sodium using a pure Y_2O_3 electrolyte has been operated at a lower temperature (400°C). Figure 24 shows proposed ionic domain boundaries for various rare earth oxides, Y_2O_3, and several solid electrolytes exhibiting the fluorite structure. Also included on this plot is the Na-Na_2O equilibrium with various iso-concentration lines for oxygen dissolved in liquid sodium. Assuming that an extrapolation of log P_θ is justifiable, it

becomes obvious that the ionic domain of Y_2O_3 is located above the Na-Na_2O (88) equilibrium. The conclusion is that the undoped Y_2O_3 of this research could never by used as an electrolyte ($t_{ion} \geq 0.99$) to measure oxygen activities in liquid sodium. Furthermore, even if Y_2O_3 could be used, the ionic conductivity is so low that equilibration times would be prohibitively long.

The yttria used as an electrolyte in the electrochemical cell patented by McPheeters et al. (67) is described as "high purity yttria (less than 1/100% impurities)." Previous investigations (21,63) along with the present investigation indicate that the electrolytic domain of yttria broadens with increasing impurity content. Although the impurity content of the yttria used in this research was higher than that described by McPheeters et al. (67), the electrolytic domain was so small that it did not include the Na-Na_2O equilibrium. This assumed that extrapolation of Equation 87 to lower temperatures is valid. One plausible explanation for their measured open circuit emfs is that their yttria electrolyte became contaminated with sodium from the electrodes. The increased impurity concentration would lead to enhanced ionic conduction. The fact that McPheeters et al. (67) did observe sig-

nificant electronic conductivity at 500°C indicated that the lower limit of the electrolytic domain for their yttria was very close to the Na-Na_2O equilibrium.

McPheeters et al. (67) also implied that CSZ has been used as a solid electrolyte but its effectiveness was limited by a reaction with sodium. Patterson (16) has evaluated the existing data concerning the electrolytic domain for CSZ. His results are shown in Figure 24 and indicate that CSZ would also be questionable as an electrolyte much below the Na-Na_2O equilibrium. In fact, according to Figure 24, the only material which appears satisfactory for this purpose is YDT and investigations concerning such measurements are currently being pursued at various laboratories.

Figure 24 also includes Tare and Schmalzried's determination (21) of log $P_{\oplus}$ and log $P_{\ominus}$ for Y_2O_3 at 825°C. The ionic domain defined by these two points is larger than the ionic domain determined by this research. Tallan and Vest (63) have suggested that such differences may result from differences in the impurity content of the Y_2O_3.

The final least-squares values of log $P_{\oplus}$ and log $P_{\ominus}$ were inserted into another computer program which plotted Schmalzried's most general solution, Equation 60, of emf as a func-

tion of log P_{O_2} between log P_{O_2} = 0 and -54. The resulting curves are shown in Figure 14 for various temperatures. The larger maximum emfs with decreasing temperature indicate the widening of the ionic domain in accordance with Equation 67.

The computer program also evaluated t_{ion} at each particular P_{O_2} value based on Equation 59 in which n was assumed to be 4. The results are summarized in Figure 15 and graphically illustrate that t_{ion} is less than 0.99 between 700 and 1000°C. Extrapolation of the data to 400°C indicates the presence of an electrolytic domain, however it is located well above the Na-Na_2O equilibrium.

Provided that a value of the electrical conductivity is known for a particular temperature and oxygen partial pressure, a complete conductivity vs log P_{O_2} curve can be calculated from the individual values of t_{ion} as follows:

$$\sigma_T = \sigma_{ion}/t_{ion} \qquad (88)$$

where σ_{ion} is constant at constant temperature. A comparison of the measured electrical conductivity data with that derived from open circuit emf measurements is shown in Figure 16. The reference conductivity for each temperature was that of Y_2O_3 in pure oxygen since it compared favorably with other investigations and represented the most reproducible data. There is

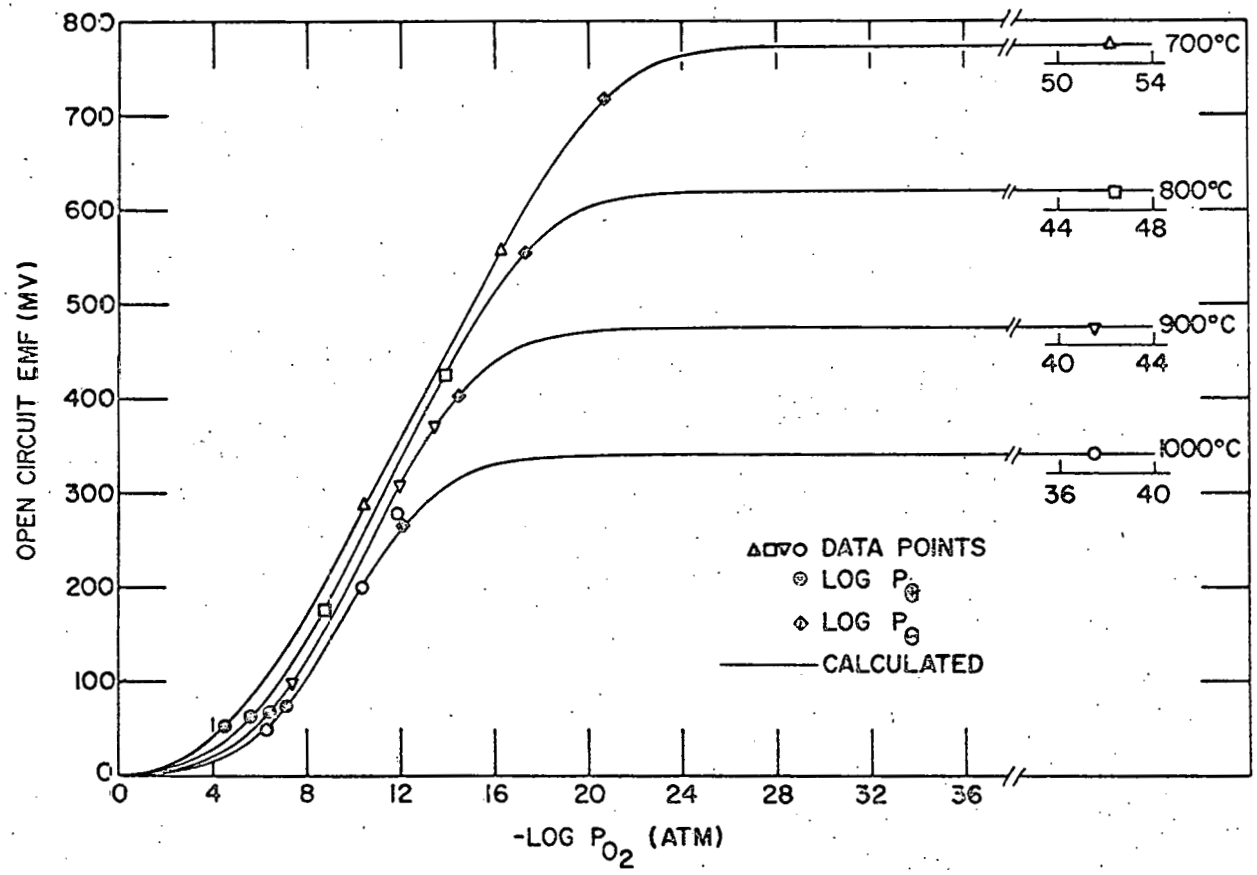

Figure 14. Calculated and measured open circuit emfs as a function of oxygen partial pressure for undoped Y_2O_3

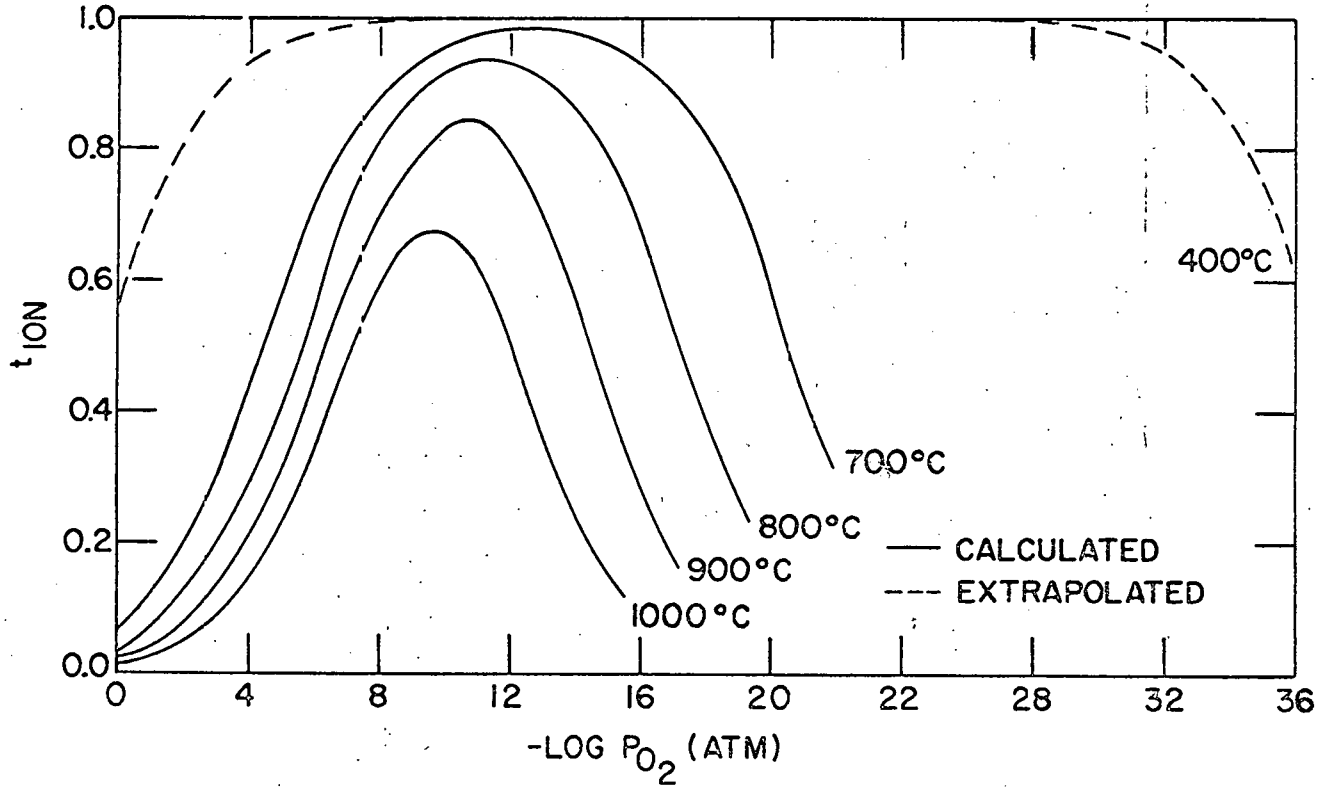

Figure 15. Ionic transference number as a function of oxygen partial pressure for undoped Y_2O_3

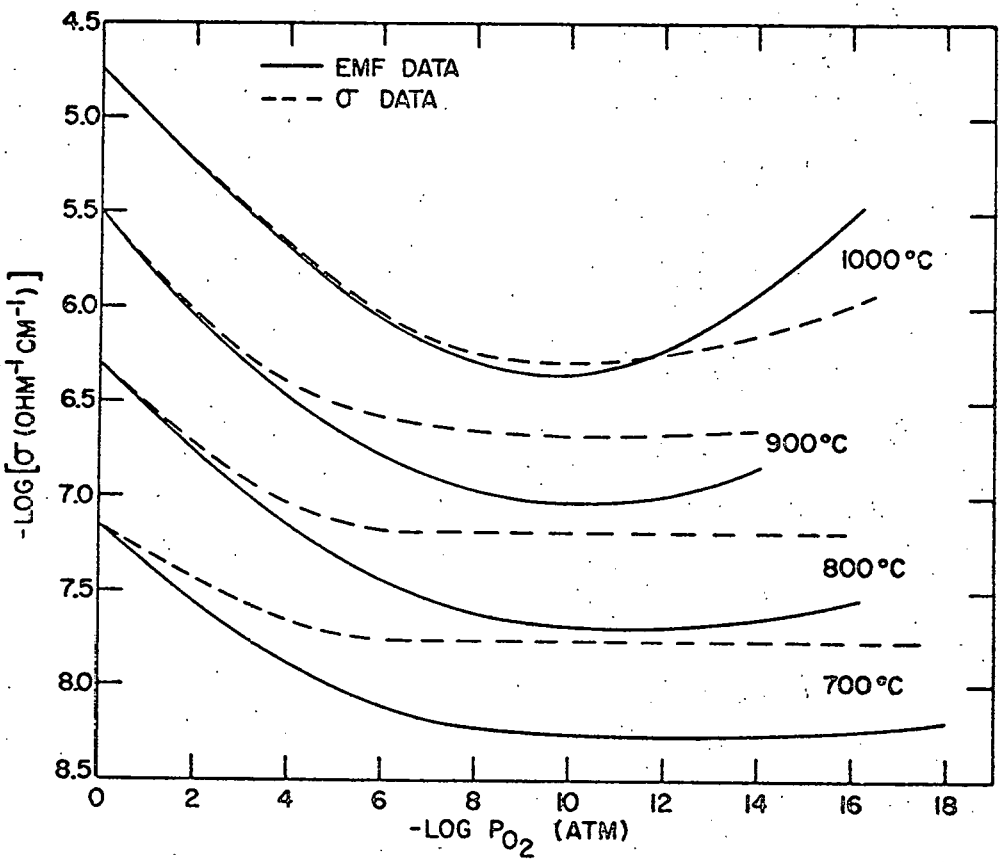

Figure 16. Comparison of the measured electrical conductivity with that derived from open circuit emf measurements for undoped Y_2O_3

very good agreement between the 1000°C isotherms. This is particularly gratifying since emf and conductivity measurements involve completely independent experiments. The limited amount of conductivity data at the lower temperatures makes it impossible to draw any conclusions, however departures do become worse with decreasing temperatures.

A useful activation energy, which actually represents the difference between $Q_{\oplus}$ and Q_{ion} can be obtained by equating the terms involving 1/T in Equations 25 and 86:

$$Q_{\oplus} - Q_{ion} = 12.6 \text{ kcal/mole.} \tag{89}$$

This value compares satisfactorily with 18.2 kcal/mole obtained from the conductivity data. A similar treatment of Equations 26 and 87 leads to

$$Q_{\ominus} - Q_{ion} = 40.4 \text{ kcal/mole} \tag{90}$$

which when combined with Q_{ion} from the electrical conductivity studies and from the open circuit emf measurements gives a bracket for $Q_{\ominus}$ of 68.0 to 75.7 kcal/mole. The fact that $Q_{\ominus} > Q_{\oplus}$ suggests a shift in the p-n junction with respect to log P_{O_2} as illustrated in Figure 1C. Tallan and Vest (63) have observed this behavior.

X-ray and Density Studies of Yttria Doped Hafnia Solid Solutions

Hafnia solid solutions with 2 to 20 m/o Y_2O_3 were subjected to x-ray analysis to determine the solubility limit of HfO_2 in the cubic fluorite structure. The presence of both the monoclinic HfO_2 and the cubic fluorite characteristic peaks on the diffractometer traces indicated that the system consists of two phases between 2 and 6 m/o Y_2O_3. For compositions between 8 and 20 m/o Y_2O_3 only the cubic fluorite phase appeared, consequently the phase boundary lies between 6 and 8 m/o Y_2O_3.

The variation in fluorite phase lattice parameter with composition is shown in Figure 17. This variation can be accounted for by the relative size of the ions, since the ionic radius of Y^{+3} (1.02 Å) (89) is larger than that of Hf^{+4} (0.83 Å) (89). The lattice parameters in this study were determined by the extrapolation method of Cohen as modified by Vogel and Kempter (83) and are based on all the observed peaks for the two phase compositions and only those peaks for which $2\theta > 60^{\circ}$ for the single phase compositions. The lattice parameters obtained in this investigation are in good agreement with published values (70).

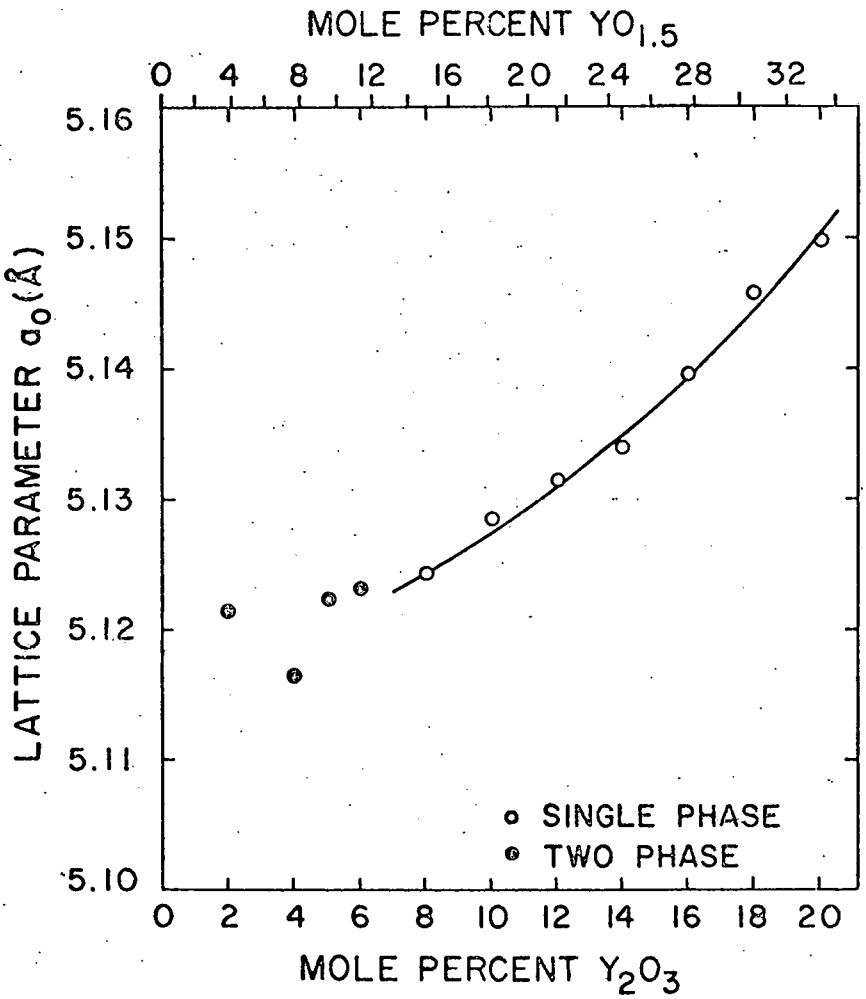

Figure 17. Variation of the fluorite phase lattice parameter with composition in the Y_2O_3-HfO_2 system

As Y_2O_3 is added to HfO_2, the charge neutrality is maintained by one of two defect structures. Either the cation sublattice remains completely filled and the appropriate number of anion vacancies are created, or the anion sublattice remains filled and the excess cations occupy interstitial sites. The difference between the two models is the addition of extra cations or the absence of oxygen ions within a unit volume and should be reflected by a difference in densities. A comparison between the measured apparent densities and the theoretical densities for each model calculated from the lattice parameter data is shown in Figure 18. On the basis of these data and the similarity between YSH and CSZ, it was concluded that the single phase cubic solid solutions possess a fluorite-type structure with a filled cation sublattice and anion vacancies.

Apparent densities were determined on sintered disks containing 10 to 15% total porosity by a water displacement method. Assuming that the disks were still within the open pore stage of sintering, the apparent densities should be very close to the pycnometric values.

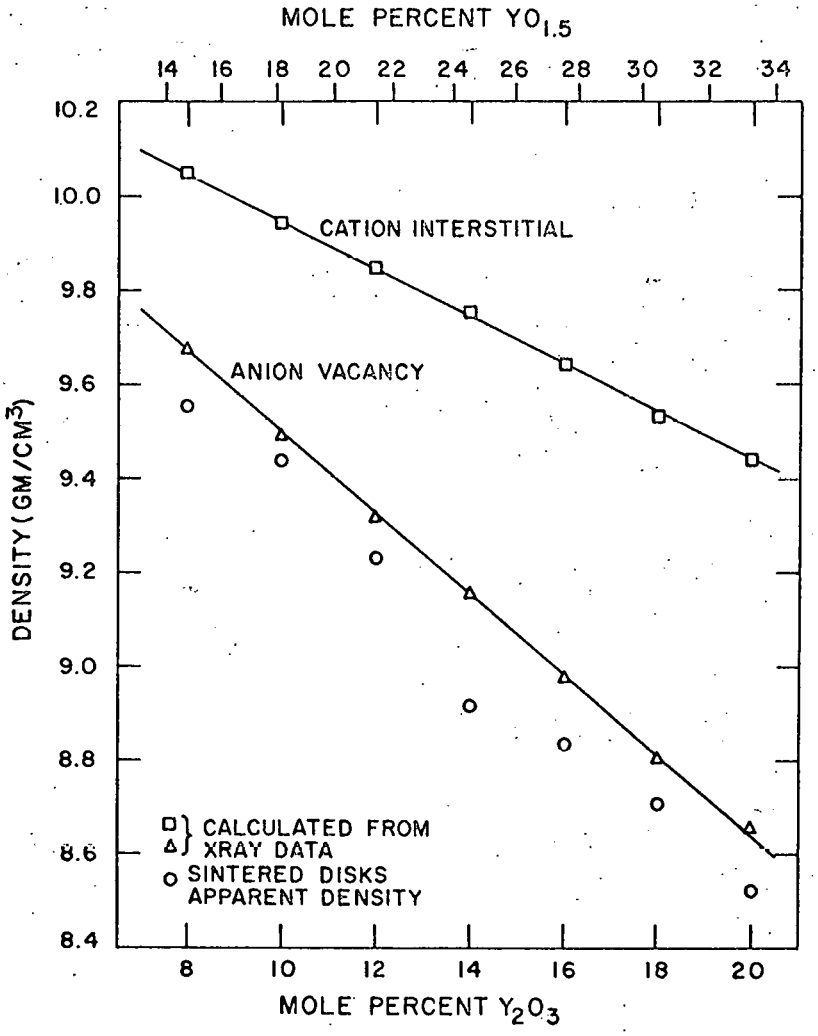

Figure 18. Theoretical and measured densities of Y_2O_3-HfO_2 solid solutions

Electrical Conductivity of Yttria Doped Hafnia Solid Solutions

The electrical conductivities of the yttria doped hafnia solid solutions were measured as a function of composition and oxygen partial pressure to determine the optimum composition for further investigation as a possible electrolyte. Figure 19 is a plot of log σ_T vs $1/T(^oK)$ for compositions from 6 to 20 m/o Y_2O_3; activation energies are included for each composition. The conductivities shown in Figure 19 were measured in dry air using a 3-probe method (87) with porous platinum electrodes.

At a constant temperature of 1000°C, the conductivities remained unchanged in atmospheres of pure oxygen, air, He/O_2 at ratios of 10 and 100, and purified helium in which log P_{O_2} was found to be ≤ -10 as measured by an in-situ solid electrolyte oxygen gage. This type of behavior indicated that all the compositions investigated were ionic conductors. Conductivities measured in controlled CO_2-CO mixtures were significantly lower than those measured in the above described atmospheres. No explanation for this type of behavior is offered, particularly since other independent experiments supported the presence of a pressure independent ionic conductivity.

The electrical conductivities agree well with values

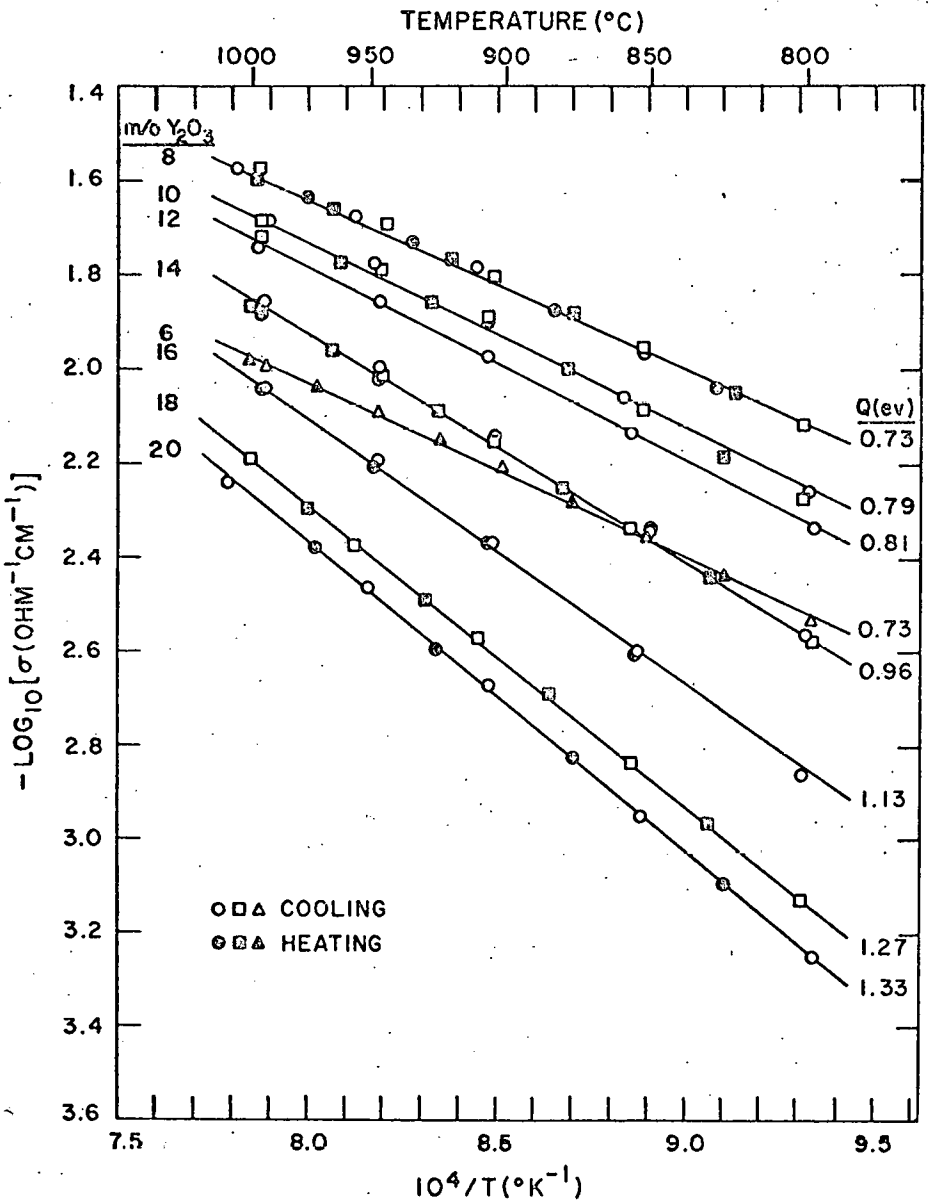

Figure 19. Total conductivity in dry air as a function of temperature for different compositions in the Y_2O_3-HfO_2 system

previously reported by Besson et al. (18) within the common temperature range of 900 to 1000°C. However, activation energies reported by Besson et al. (18) are approximately 0.25 ev higher than those obtained from this work.

Since the 8 m/o Y_2O_3 composition possessed the highest conductivity and the lowest activation energy as shown in Figure 20, it was chosen for further investigation as a possible electrolyte. The fact that the 6 m/o composition had the same activation energy as the 8 m/o composition but a lower total conductivity supports the x-ray studies in placing the phase boundary between these two limits. If there are two phases present at the 6 m/o composition, the monoclinic HfO_2 solid solution would be present as small islands in a continuous cubic fluorite host with a composition corresponding to the solubility limit of HfO_2 in the fluorite structure. Indications are that the conductivity is much lower in the monoclinic phase (18) than in the fluorite phase, consequently the measured conductivity and activation energy would correspond to the continuous fluorite host with a slightly reduced effective cross sectional area. Thus the effect of the nonconducting islands would be to decrease the total flux and thereby decrease the apparent total conductivity without altering the

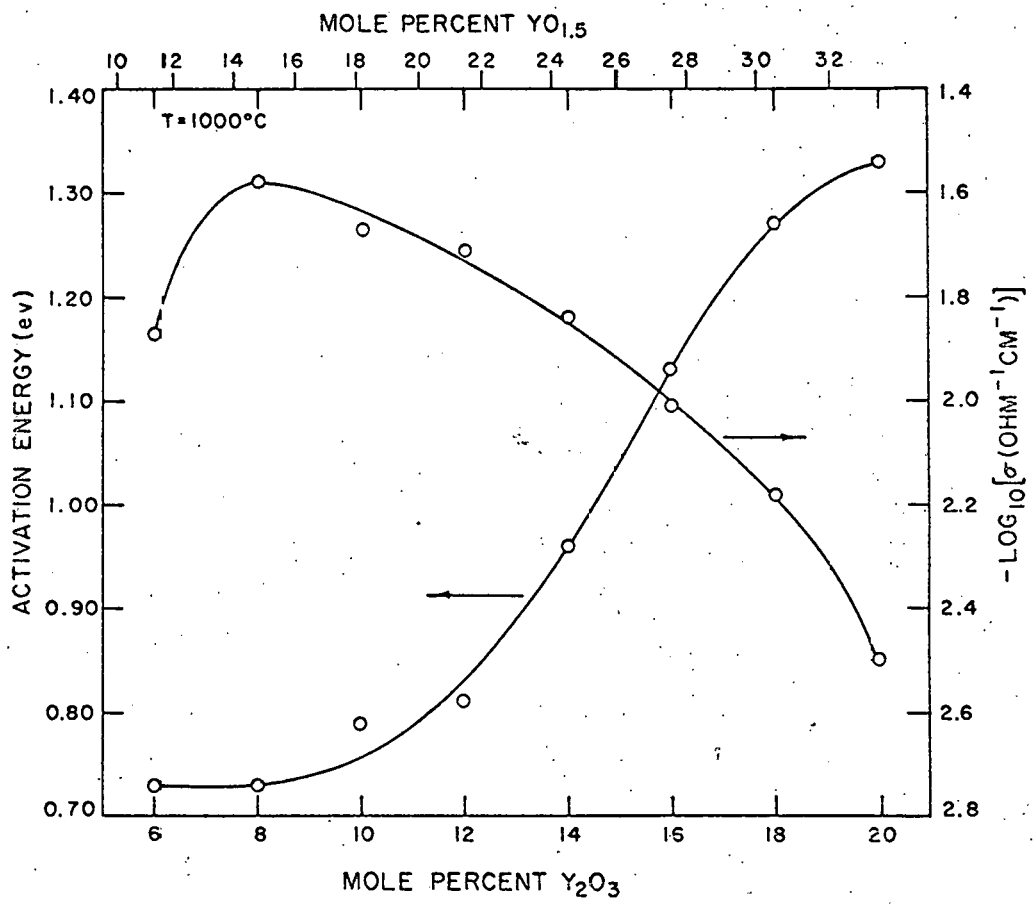

Figure 20. Activation energy and 1000°C isothermal conductivity as a function of composition in the Y_2O_3-HfO_2 system

activation energy.

Figure 20 shows a trend of increasing activation energies and decreasing conductivities for increasing Y_2O_3 content above 8 m/o. This trend has been previously observed for the fluorite phase of the Y_2O_3-HfO_2 system (18,90) and other similar systems (10,19,32). It has been suggested that this trend is due to ordering of anion vacancies which are then not as free to participate in the conduction process (8).

Open Circuit Emf Measurements on 8 m/o Y_2O_3-Hafnia

Straightforward open circuit emf measurements were made on the following cells:

$$Ni,NiO/YSH/Co,CoO \qquad XXI$$

$$Cu,Cu_2O/YSH/Ni,NiO \qquad XXII$$

to check for electrolytic behavior of the 8 m/o Y_2O_3 composition. The results of these measurements as a function of temperature are given in Figure 21. The measured emfs are slightly lower than the thermodynamic emfs given by Equation 66. The pressure independence of the conductivity in the high oxygen pressure region and the magnitudes of $\sigma_{\oplus}$ and $\sigma_{\ominus}$ from polarization experiments suggest that the low emf values are not the result of a perceptible electronic transference number ($t_e > 0.01$).

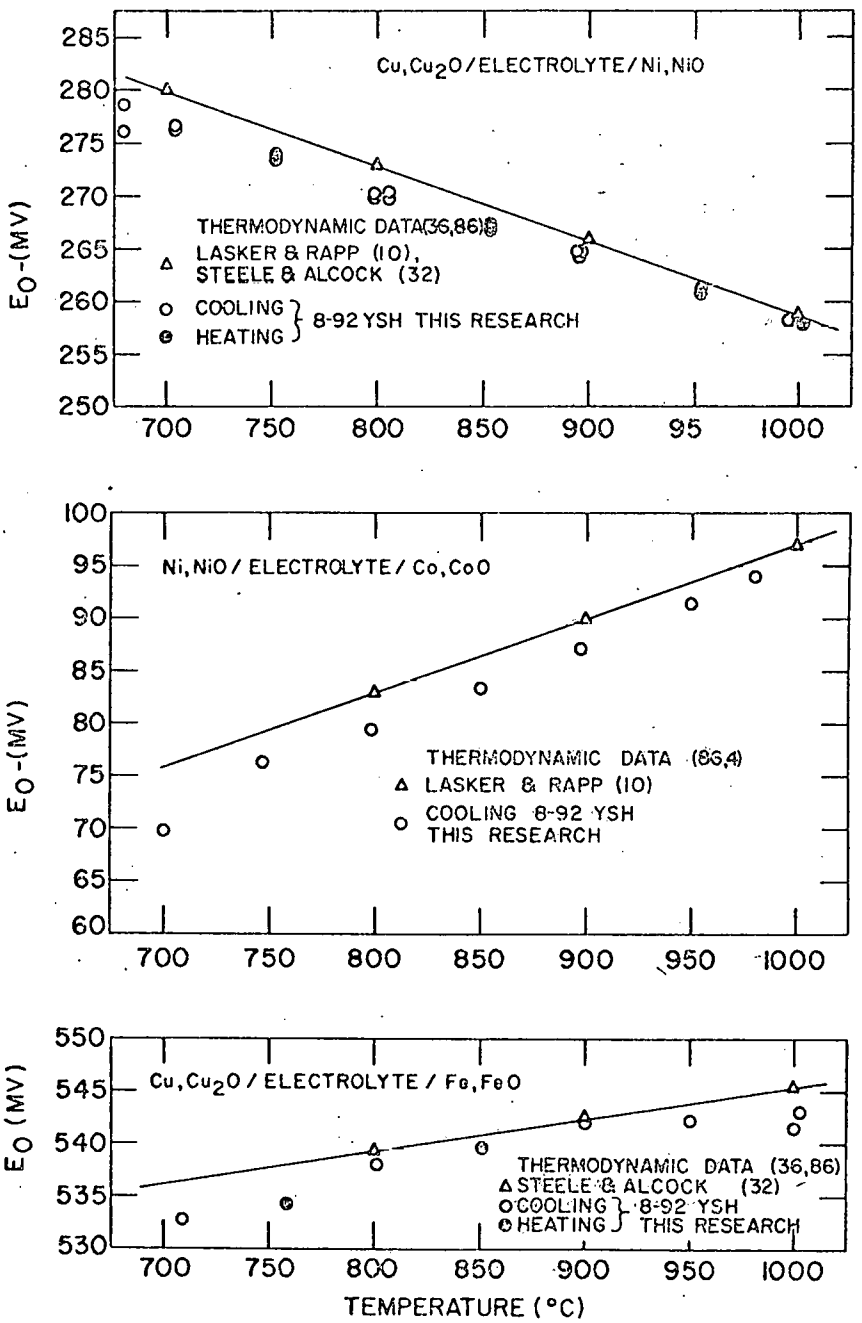

Figure 21. Open circuit emfs as a function of temperature for various cells using an 8 m/o Y_2O_3-HfO_2 electrolyte

Open circuit emf cells, such as

$Cu,Cu_2O/YSH/Fe,FeO$ XXIII

$Fe,FeO/YSH/Hf,HfO_2$ XXIV

$Co,CoO/YSH/NbO,NbO_2$ XXV

which involved large oxygen potential gradients did not produce stable emfs. It was believed that the large amount of open porosity in the samples allowed molecular or atomic oxygen to be transferred through the electrolyte leading to failure of the electrodes to maintain a fixed oxygen potential. To combat this problem and rejuvenate the cell, an appropriate voltage was applied to the cell to titrate oxygen from the low to the high oxygen potential electrode. The titrations were deliberately designed to "over restore" the apparently polarized electrodes. The titration current leads were then removed and the open circuit emf was recorded as a function of time. The open circuit emfs decreased to a steady value, which remained essentially constant for perceptible periods of time before starting to decay again. In all cases, the emf vs time plateaus corresponded very closely to the thermodynamic emfs as illustrated for example by Cell XXIII. Oxygen was titrated away from the Fe-FeO electrode and into the $Cu-Cu_2O$ electrode. The cell was open circuited and two

plateau emfs were observed at 700°C with respect to Fe-FeO equilibrium; the first one corresponded to Cu_2O-CuO equilibrium (810 mv) and the second one corresponded to Cu-Cu_2O equilibrium (533 mv).

Another interesting observation concerning this cell titration was that the emf initially decayed (4 mv) below the Cu-Cu_2O plateau value before regaining the plateau value. Tare and Schmalzried (57) observed this type of behavior when they investigated the decomposition kinetics for CO_2 during the oxidation of iron to wüstite by CO_2-CO gas mixtures. Following their interpretation, the 4 mv dip mentioned above is a measure of the oxygen chemical potential difference required to nucleate Cu in Cu_2O.

The data for Cell XXIII as represented in Figure 21 were obtained from steady plateau emfs with time following coulometric titration of the cell.

Similarly, emf data were extracted from Cells XXIV and XXV following oxygen titration to rejuvenate the electrodes. Both cells supplied limited information at 1000°C before a break in an electrical lead terminated the runs. Cell XXV produced an emf plateau between 640 and 620 mv as compared to a thermodynamic emf of 639 mv. This indicates that the 8 m/o

Y_2O_3 composition remains very nearly an electrolyte at oxygen partial pressures as low as log P_{O_2} = -21.9.

The open circuit plateau emf for Cell XXIV was at 595 mv. Since the necessary approximations are valid, Equation 68 was used to calculate the lower limit of the ionic domain, i.e. log P_θ = -24.4. It is interesting to note, as shown in Figure 24, that this point is very close to log P_θ for CSZ.

Representative samples taken after the sintering process, the conductivity, and the emf investigations were submitted for electron microprobe and wet chemical analyses to verify the composition of the solid solutions and to check for contamination resulting from the electrodes used in the emf studies. Results showed that the compositions remained unchanged and equalled the calculated compositions based on the standardized yttria and hafnia liquid solutions. As expected, the microprobe analysis indicated that the Fe-FeO electrode reacted slightly with the fluorite solid solutions, probably due to the presence of Y_2O_3. No reaction zones could be detected for the other electrodes used.

D-c Polarization Measurements on 8 m/o Y_2O_3-Hafnia

An electrolyte of 8 m/o Y_2O_3 was subjected to Wagner d-c polarization measurements to determine the magnitude of the

electronic conductivity. A voltage was applied across the cell

$$Cu,Cu_2O/YSH/Au,Pt \qquad \text{XXVI}$$

forcing the oxygen ions to migrate to the reversible electrode. The steady state current, which is assumed to be entirely electronic in nature, was recorded as a function of the applied voltage. The data were analyzed through the use of Equation 77 and the results are shown in Figure 22, where $\sigma_\oplus$ and $\sigma_\ominus$ represent the hole and excess electron conductivity, respectively, at the Cu-Cu_2O electrode.

The total conductivities of the 8 m/o Y_2O_3 composition measured in this investigation were assumed to be the ionic conductivities. The hole and excess electron conductivities given in Figure 22 were extrapolated based on a +1/4 and a -1/4 oxygen pressure dependence until they intersected the ionic conductivity. These intersections define the ionic domain and are represented by log $P_\oplus$ and log $P_\ominus$. Results from this type of analysis are summarized in Table 5.

Table 5. Log $P_\oplus$ and log $P_\ominus$ for 8 m/o Y_2O_3-Hafnia

Temperature (°C)	log $P_\oplus$ (atm)	log $P_\ominus$ (atm)
1000	+8.4	-24.8
850	+5.1	-28.7

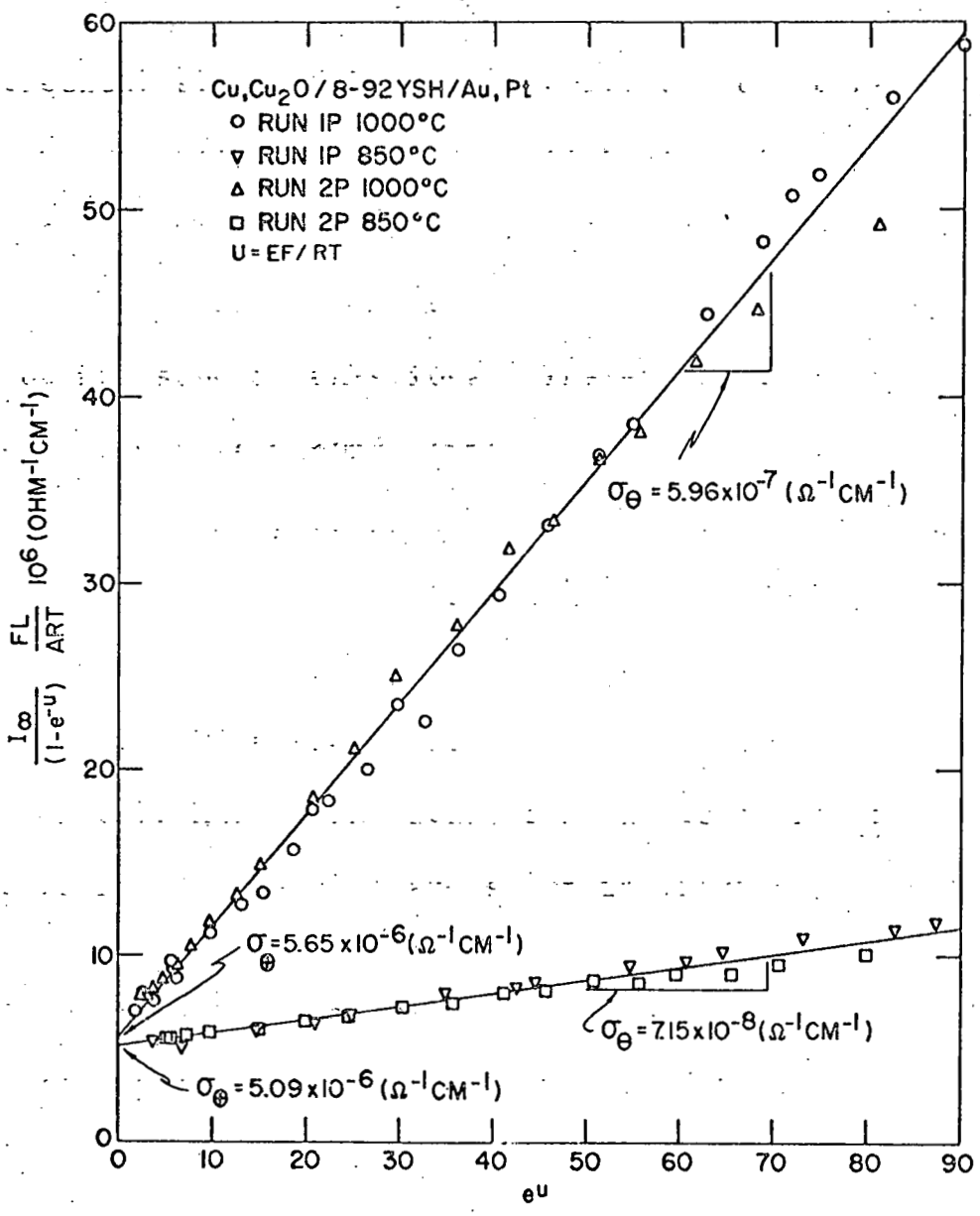

Figure 22. Converted data plot according to Patterson (14) for d-c polarization measurements with the cell $Cu,Cu_2O/8m/o\ Y_2O_3\text{-}HfO_2/Au,Pt$

The 850°C data appear questionable when analyzed according to Wagner's theory (77). Although the data showed the expected nonohmic behavior when plotted on a I_∞ vs E graph, doubt arises when the data are plotted on a log I_∞ vs E graph. At high applied voltages (E > 300 mv), the 1000°C data possessed the theoretical slope of F/(2.3RT) while the 850°C data gave half the theoretical slope. The less than theoretical slope at 850°C could indicate a change in conduction mechanism, however the open circuit emf and electrical conductivity studies do not support this idea. Therefore, only the 1000°C data are used with any confidence.

Analysis of the polarization data at 1000°C did locate the upper and lower limits of the ionic domain. In fact the lower domain limit of log P_θ = -24.8 is in excellent agreement with that of log P_θ = -24.4 obtained by open curcuit emf measurements on Cell XXIV. The ionic domain boundaries from the 1000°C polarization results are shown in Figure 24.

Coulometric Titration-Open Circuit Emf Cell Results

The cell pictured in Figure 9 was used to compare the electrolytic behavior of YSH with that of CSZ. The results of the measurements are represented in Figure 23 and can be very simply summarized by the following expression:

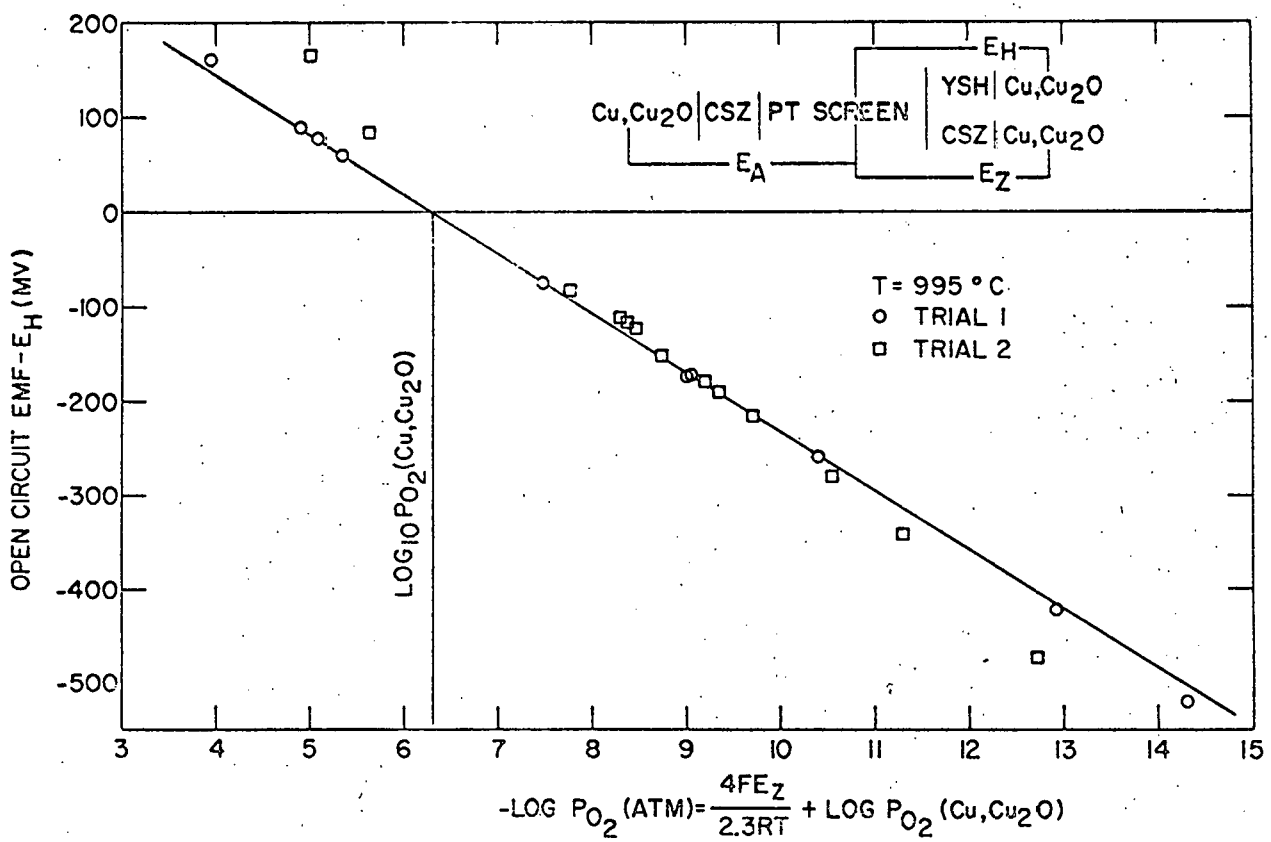

Figure 23. Open circuit emf of 8 m/o Y_2O_3-HfO_2 as a function of oxygen partial pressure based on the reference electrolyte calcia stabilized zirconia

$$E(YSH) \geq E(CSZ). \qquad (91)$$

Since CSZ is an accepted electrolyte (4) over the entire P_{O_2} range scanned, Relation 91 implies that YSH is also an electrolyte over the same P_{O_2} range. The difference between the two measured open circuit emfs for a given applied potential is believed to result from contact and electrode problems at the common interface, rather than from nonelectrolytic behavior of either the CSZ or YSH specimens. The fact that the applied voltage across the oxygen pump was significantly greater than the measured open circuit emfs also supports this belief.

Since this is the first time a cell of this type has ever been used, there are certain experimental difficulties associated with its operation. However, it does appear to offer an experimental method for determining ionic domain boundaries of various materials.

THIS PAGE

WAS INTENTIONALLY

LEFT BLANK

Figure 24. Ionic domain boundaries for various oxide materials

1. Na, Na_2O equilibrium, Wicks and Block (88)
2. $P_{\oplus}$, Y_2O_3, this research
3. $P_{\ominus}$, Y_2O_3, this research

Δ $P_{\oplus}$, Y_2O_3, Tare and Schmalzried (21)

$\square$ $P_{\ominus}$, Y_2O_3, Tare and Schmalzried (21)

4. $P_{\oplus}$, CSZ, Patterson (16)
5. $P_{\ominus}$, CSZ, Patterson (16)
6. $P_{\oplus}$, YDT, Lasker and Rapp (10)
7. $P_{\ominus}$, YDT, Hardaway (15)
8. $P_{\oplus}$, Gd_2O_3, Tare and Schmalzried (21)
9. $P_{\oplus}$, Sm_2O_3, Tare and Schmalzried (21)
10. $P_{\ominus}$, Sm_2O_3, Tare and Schmalzried (21)
11. $P_{\oplus}$, Dy_2O_3, Tare and Schmalzried (21)
12. $P_{\oplus}$, Dy_2O_3, Macki (65)

∇ $P_{\oplus}$, YSH, this research

$\diamond$ $P_{\ominus}$, YSH, this research

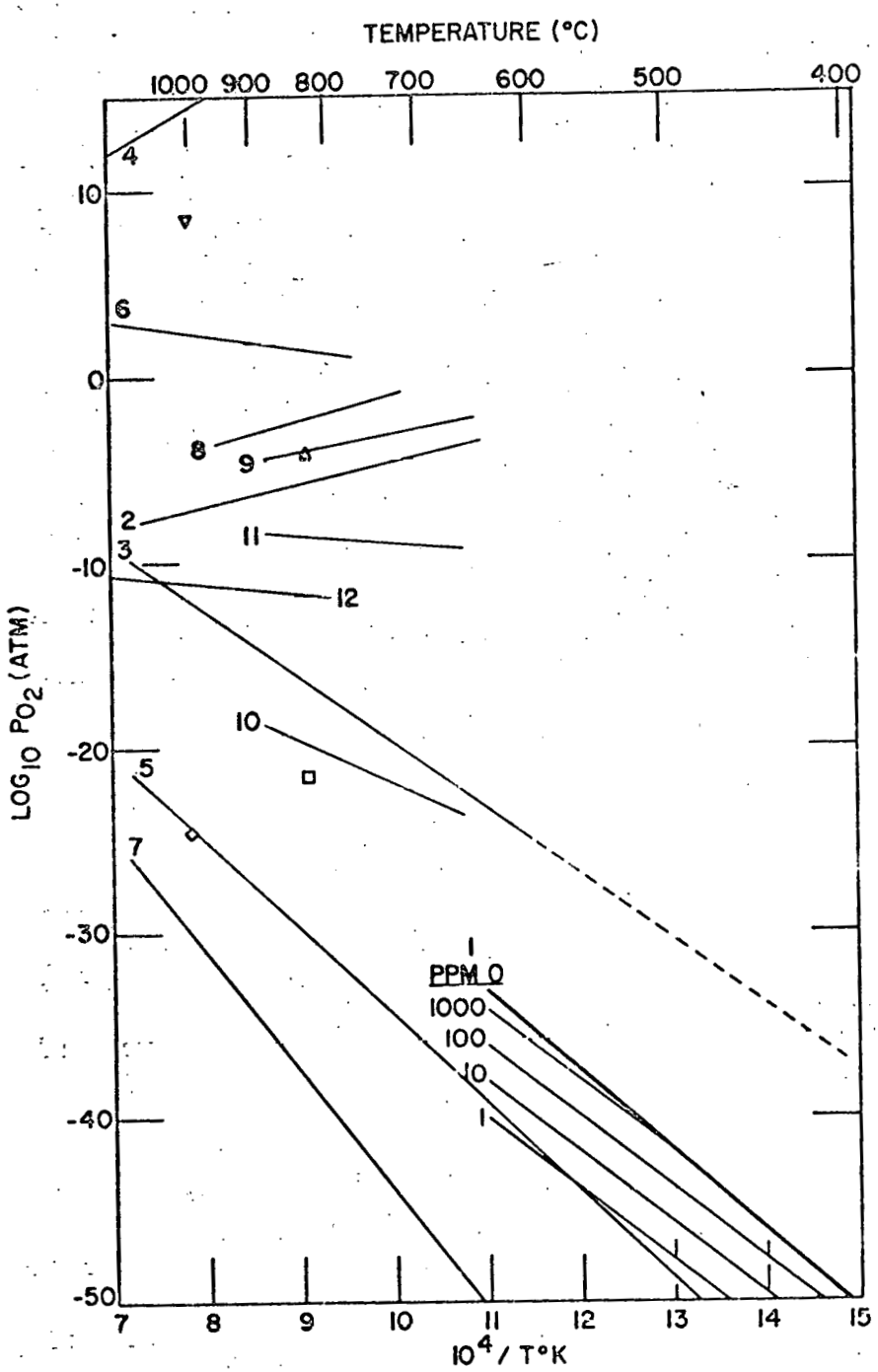
TEMPERATURE (°C)
1000 900 800 700 600 500 400
10
0
-10
-20
-30
-40
-50
LOG10 PO2 (ATM)
4
6
8
9
2
11
3
12
10
5
7
1
PPM O
1000
100
10
1
7 8 9 10 11 12 13 14 15
10^4 / T°K

CONCLUSIONS

1. Undoped Y_2O_3 is a mixed conductor showing a narrow ionic conduction domain ($t_{ion} \geq 0.5$) but no electrolytic domain ($t_{ion} \geq 0.99$) within the temperature range (700-1000°C) studied. The ionic domain boundaries for Y_2O_3 may be represented by

$$\log P_{\Theta} = \frac{11,030}{T(^{o}K)} - 15.84$$

and

$$\log P_{\Theta} = \frac{-35,300}{T(^{o}K)} + 15.59.$$

2. At high oxygen partial pressures, the total conductivity behavior for undoped Y_2O_3 was indicative of positive hole conduction.

3. Previous claims regarding the use of pure Y_2O_3 as a solid electrolyte to obtain an accurate electrochemical measurement of oxygen potentials in liquid sodium are exaggerated.

4. The cubic fluorite phase of yttria stabilized hafnia remains stable from about 7 m/o Y_2O_3 to compositions greater than 20 m/o Y_2O_3 which was the highest composition used in this investigation.

5. The fluorite phase is an anion defective structure with substitutional replacement of hafnium with yttrium.

Charge neutrality is maintained by fully ionized anion vacancies.

6. All yttria-hafnia solid solutions between 6 and 20 m/o Y_2O_3 exhibit a predominant ionic conductivity at elevated temperatures as evidenced by the oxygen pressure independence of the total conductivity.

7. Within the yttria stabilized hafnia fluorite phase, activation energies increase and total conductivities decrease with increasing Y_2O_3 content. These trends suggest a tendency toward anion vacancy ordering.

8. The 8 m/o Y_2O_3-HfO_2 composition is a solid electrolyte over finite oxygen pressure and temperature ranges. The electrolytic domain width ($t_{ion} \geq 0.99$) for this composition at 1000°C is from log P_{O_2}(atm) = -16.6 to +0.4 and is very similar to that of calcia stabilized zirconia.

LITERATURE CITED

1. Nernst, W. Über die elektrolytische leitung fester körper bei sehr hohen temperaturen. Zeitschrift für Elektrochemie 6(2): 41-43. 1899.

2. Wagner, C. Contribution to the theory of the oxidation process. Zietschrift für Physikalische Chemie 21(1-2): 25-41. 1933.

3. Kiukkola, K. and Wagner, C. Galvanic cells for determination of the standard molar free energy of formation of metal halides, oxides, and sulfides at elevated temperatures. Electrochemical Society Journal 104(5): 308-316. 1957.

4. Kiukkola, K. and Wagner, C. Measurements on galvanic cells involving solid electrolytes. Electrochemical Society Journal 104(5): 379-387. 1957.

5. Peters, H. and Mann, G. Elektrochemische untersuchung des gleichgewichtes $Fe + CO_2 \rightleftarrows FeO + CO$. Zeitschrift für Elektrochemie, Bunsengesellschaft für Physikalische Chemie 63(2): 244-248. 1959.

6. Peters, H. and Möbius, H. Elektrochemische untersuchung der gleichgewichte $CO + \frac{1}{2}O_2 \rightleftarrows CO_2$ und $C + CO_2 \rightleftarrows 2CO$. Zeitschrift für Physikalische Chemie (Leipzig) 209(5/6): 298-309. 1958.

7. Diness, A. M. and Roy, R. Experimental confirmation of major change of defect type with temperature and composition in ionic solids. Solid State Communications 3(6): 123-125. 1965.

8. Carter, R. E. and Roth, W. L. Conductivity and structure in calcia-stabilized zirconia. In Alcock, C. B., ed. Electromotive force measurements in high-temperature systems. Pp. 125-144. New York, New York, American Elsevier Publishing Company, Inc. 1968.

9. Subbarao, E. C., Sutter, P. H., and Hrizo, J. Defect structure and electrical conductivity of ThO_2-Y_2O_3 solid

solutions. American Ceramic Society Journal 48(9): 443-446. 1965.

10. Lasker, M. F. and Rapp, R. A. Mixed conduction in ThO_2 and ThO_2-Y_2O_3 solutions. Zeitschrift für Physikalische Chemie Neue Folge. 49(3/4): 198-211. 1966.

11. Kingery, W. D., Pappis, J., Doty, M. E., and Hill, D. C. Oxygen ion mobility in cubic $Zr_{0.85}Ca_{0.15}O_{1.85}$. American Ceramic Society Journal 42(8): 393-398. 11959.

12. Buckley, J. D. Deterioration of calcia-stabilized zirconia. NASA TN (Technical Note) D-1595 [National Aeronautics and Space Administration, Washington, D.C.]. 1962.

13. Alcock, C. B. and Steele, B. C. H. Solid oxide electrolytes. In Stewart, G. H., ed. Science of Ceramics. Vol. 2. Pp. 397-406. New York, New York, Academic Press. 1965.

14. Patterson, J. W., Bogren, E. C., and Rapp, R. A. Mixed conduction in $Zr_{0.85}Ca_{0.15}O_{1.85}$ and $Th_{0.85}Y_{0.15}O_{1.925}$ solid electrolytes. Electrochemical Society Journal 114 (7): 752-758. 1967.

15. Hardaway, J. B. The ionic domain for yttria doped thoria at low oxygen potentials. Unpublished M.S. thesis. Ames, Iowa, Library, Iowa State University of Science and Technology. 1969.

16. Patterson, J. W. Conduction domains in solid mixed conductors and electrolytic domain of calcia stabilized zirconia. Special Report on Contract No. F33615-68-C-1034. Ames, Iowa, Engineering Research Institute, Iowa State University of Science and Technology. 1969.

17. Smith, A. W., Meszaros, F. W., and Amata, C. D. Permeability of zirconia, hafnia, and thoria to oxygen. American Ceramic Society Journal 49(5): 240-244. 1966.

18. Besson, J., Deportes, C., and Robert, G. Conductibilite electrique dans le systeme oxyde de hafnium-oxyde d'yttrium a haute temperature. Academie des Sciences

Paris, Serie C, 262(7): 527-530. 1966.

19. Johansen, H. A. and Cleary, J. G. High-temperature electrical conductivity in the systems $CaO-ZrO_2$ and $CaO-HfO_2$. Elèctrochemical Society Journal 111(1): 100-103. 1964.

20. Aleshin, E. and Roy, R. Crystal chemistry of pyrochlore. American Ceramic Society Journal 45(1): 18-25. 1962.

21. Tare, V. B. and Schmalzried, H. Ionen-und elektronenleitung in einigen seltenen erdoxiden. Zeitschrift für Physikalische Chemie Neue Folge 43(1/2): 30-32. 1964.

22. Hyde, B. G., Bevan, D. J. M. and Eyring, L. A structural model of the rare-earth oxides. In International Conference on Electron Diffraction and the Nature of Defects in Crystals. Pp. II C-4-5. New York, New York, Pergamon Press. 1965.

23. Eyring, L. On the fluorite-related oxide phases of the rare earth and actinide elements. U.S. Atomic Energy Commission Report COO-1109-26 [Chicago Operations Office, AEC]. 1966.

24. Alcock, C. B., ed. Electromotive force measurements in high-temperature systems. New York, New York, American Elsevier Publishing Company, Inc. 1968.

25. Raleigh, D. O. Solid state electrochemistry. In Riess, H., ed. Progress in Solid State Chemistry. Volume 3. Pp. 83-134. New York, New York, Pergamon Press. 1966.

26. Rapp, R. A. and Maak, F. Thermodynamic properties of solid copper-nickel alloys. Acta Metallurgica 10(1): 63-69. 1962.

27. Darken, L. S. and Gurry, R. W. The system iron-oxygen. I. The wüstite field and related equilibria. American Chemical Society Journal 67(8): 1398-1412. 1945.

28. Rapp, R. A. Free energy of formation of molybdenum dioxide. Metallurgical Society of the American Institute of Mining, Metallurgical, and Petroleum Engineers Transactions 227(4): 371-374. 1963.

29. Alcock, C. B. and Zador, S. Thermodynamic study of the manganese/manganous-oxide system by the use of solid oxide electrolytes. Electrochimica Acta 12(6): 673-677. 1967.

30. Ignatowicz, S. and Davies, M. W. The free energy of formation of NbO and Ta_2O_5. Journal of the Less-Common Metals 15(1): 100-102. 1968.

31. Worrell, W. L. Measurements of the thermodynamic stabilities of the niobium and tantalum oxides using a high-temperature galvanic cell. In Thermodynamics. Vol. 1. Pp. 131-143. Vienna, Austria, International Atomic Energy Agency. 1966.

32. Steele, B. C. H. and Alcock, C. B. Factors influencing the performance of solid electrolytes in high-temperature thermodynamic measurements. Metallurgical Society of the American Institute of Mining, Metallurgical, and Petroleum Engineers Transactions 233(7): 1359-1367. 1965.

33. Blumenthal, R. N., Moser, J. B., and Whitmore, D. H. Thermodynamic study of nonstoichiometric niobium pentoxide. American Ceramic Society Journal 48(12): 617-622. 1965.

34. Newns, G. R. and Pelmore, J. M. Thermodynamics of indium oxide from measurements of electromotive force. Journal of the Chemical Society (London) Series A, pp. 360-362. 1968.

35. Bidwell, L. R. Free energy of formation of cupric oxide. Electrochemical Society Journal 114(1): 30-31. 1967.

36. Rizzo, F. E., Bidwell, L. R., and Frank, D. E. The standard free energy of formation of cuprous oxide. Metallurgical Society of the American Institute of Mining, Metallurgical, and Petroleum Engineers Transactions 239(4): 593-596. 1967.

37. Schmalzried, H. Zur messung der freien reaktionsenthalpie bei der bildung von spinnellphasen aus den einzeloxyden mit hilfe galvanischer festkörperkitten. Zeitschrift für Physikalische Chemie Neue Folge 25(3/4): 178-192. 1960.

38. Benz, R. and Wagner, C. Thermodynamics of the solid system $CaO-SiO_2$ from electromotive force data. Journal of Physical Chemistry 65(8): 1308-1311. 1961.

39. Levine, S. R. and Kolodney, M. The free energy of formation of tantalum silicides using solid oxide electrolytes. Electrochemical Society Journal 116(10): 1420-1424. 1969.

40. Carter, R. E. Dissociation pressures of solid solutions from Fe_3O_4 to 0.4 $Fe_3O_4 \cdot 0.6$ $CoFe_2O_4$. American Ceramic Society Journal 43(9): 448-452. 1960.

41. Kubik, A. and Alcock, C. B. Activities in solid binary alloy systems. In Alcock, C. B., ed. Electromotive force measurements in high-temperature systems. Pp. 43-49. New York, New York, American Elsevier Publishing Company, Inc. 1968.

42. Bidwell, L. R. and Speiser, R. The relative thermodynamic properties of solid nickel-palladium alloys. Acta Metallurgica 13(2): 61-70. 1965.

43. Weissbart, J. and Ruka, R. Oxygen gauge. Review of Scientific Instruments 32(5): 593-595. 1961.

44. Schmalzried, H. Über zirkondioxyd als elektrolyt für elektrochemische untersuchungen bei höheren temperaturen. Zeitschrift für Electrochemie 66(7): 572-576. 1962.

45. Fruehan, R. J., Martonik, L. J., and Turkdogan, E. T. Development of a galvanic cell for the determination of oxygen in liquid steel. Metallurgical Society of the American Institute of Mining, Metallurgical and Petroleum Engineers Transactions 245(7): 1501-1509. 1969.

46. Schwerdtferger, K. Measurement of oxygen activity in iron, iron-silicon, manganese, and iron-manganese melts using solid electrolyte galvanic cells. Metallurgical Society of the American Institute of Mining, Metallurgical, and Petroleum Engineers Transactions 239(9): 1276-1281. 1967.

47. Pargeter, J. K. A method for direct oxygen determination in molten metals. Journal of Metals 20(10): 27-31. 1968.

48. Fitterer, G. R., Cassler, C. D., and Vierbicky, V. L. Oxygen in steel refining as determined by solid electrolyte techniques. Journal of Metals 21(8): 46-52. 1969.

49. Aronson, S. and Belle, J. Nonstoichiometry in uranium dioxide. Journal of Chemical Physics 29(1): 151-158. 1958.

50. Markin, T. L., Bones, R. J., and Wheeler, V. J. Galvanic cells and gas equilibration techniques. British Ceramic Society Proceedings 8(6): 51-67. 1966.

51. Steele, B. C. H. Measurement of high-temperature thermodynamic properties of nonstoichiometric oxides using solid state emf and coulometric techniques. In Wachtman, J. B. and Franklin, A. D., eds. Mass transport in oxides. National Bureau of Standards Special Publication 296: 165-172. 1968.

52. Rizzo, H. F., Gordon, R. S., and Cutler, I. B. The determination of thermodynamic properties in single phase wüstite by coulometric titration in a high temperature galvanic cell. In Wachtman, J. B. and Franklin, A. D., eds. Mass transport in oxides. National Bureau of Standards Special Publication 296: 129-142. 1968.

53. Yuan, D. and Kröger, F. A. Stabilized zirconia as an oxygen pump. Electrochemical Society Journal 116(5): 594-600. 1969.

54. Tretyakov, J. D. and Muan, A. A new cell for electrochemical studies at elevated temperatures: Design and properties of a cell involving a combination of thorium oxide-yttrium oxide and zirconium oxide-calcium oxide electrolytes. Electrochemical Society Journal 116(3): 331-334. 1969.

55. Weissbart, J. and Ruka, R. A solid electrolyte fuel cell. Electrochemical Society Journal 109(8): 723-726. 1962.

56. Rickert, H. Kinetic measurements with solid electrolytes. In Alcock, C. B., ed. Electromotive force measurements in high-temperature systems. Pp. 59-90. New York, New York, American Elsevier Publishing Company, Inc. 1968.

57. Tare, V. B. and Schmalzried, H. The use of a ZrO_2(+CaO) solid electrolyte galvanic cell for the determination of rate constants for gas-solid reactions involving oxygen. Metallurgical Society of the American Institute of Mining, Metallurgical, and Petroleum Engineers Transactions 236(4): 444-446. 1966.

58. Foex, M. and Traverse, J. Remarques sur les transformations cristallines presentees a haute temperature par les sesquioxydes de terres rares. Revue Internationale des Hautes Temperatures et des Refractaires 3(4): 429-453. 1966.

59. Roth, R. S. and Schneider, S. J. Phase equilibria in systems involving the rare earth oxides. Part 2: Polymorphism of the oxides of the trivalent rare earth ions. National Bureau Standards Journal of Research 64A: 309-316. 1960.

60. Noddack, W., Walch, H., and Dobner, W. Leitfähigkeitsmessungen an oxyden der seltenen erden I. Zeitschrift für Physikalische Chemie 211(3/4): 180-193. 1959.

61. Noddack, W. and Walch, H. Über einige eigenschaften der oxyde der seltenen erden II. Zeitschrift für Physikalische Chemie 211(3/4): 194-207. 1959.

62. Noddack, W. and Walch, H. Über die elektrische leitfähigkeit van oxyden. Zeitschrift für Elektrochemie 63(2): 269-274. 1959.

63. Tallan, N. M. and Vest, R. W. Electrical properties and defect structure of Y_2O_3. American Ceramic Society Journal 49(8): 401-404. 1966.

64. Schmalzried, H. Ionen-und elektronenleitung in binären oxyden und ihre untersuchung mittels emk-messungen. Zeitschrift für Physikalische Chemie Neue Folge 38(1/2): 87-102. 1963.

65. Macki, J. M. The electrical conductivity of pure and doped Dy_2O_3 and Gd_2O_3. Unpublished Ph.D. thesis. Columbus, Ohio, Library, Ohio State University. 1968.

66. Bhattacharyya, A. L. A study of some electrical properties of Er_2O_3. Dissertation Abstracts 28B(11): 4719. 1968.

67. McPheeters, C. C., McGuire, J. C., and Tercovich, R. Solid electrolyte electrochemical cell. U.S. Patent 3,309,233. March 14, 1967.

68. Komissarova, L. N., Ken-shih, W., Spitsyn, V. I., and Simanov, Y. P. The HfO_2-La_2O_3 system. Russian Journal of Inorganic Chemistry 9(3): 383-386. 1964.

69. Spiridinov, F. M., Stepanov, V. A., Komissarova, L. N., and Spitsyn, V. I. The binary system HfO_2-Gd_2O_3. Journal of the Less-Common Metals 14(4): 435-443. 1968.

70. Caillet, M., Deportes, C., Robert, G., and Vitter, G. Etude structurale dans le systeme HfO_2-Y_2O_3. Revue Internationale des Hautes Temperatures et des Refractaires 4(4): 269-271. 1967.

71. Richardson, F. D. and Jeffes, J. H. E. The thermodynamics of substances of interest in iron and steel making from 0°C to 2400°C, Part I-Oxides. Iron and Steel Institute Journal 160(1): 261-270. 1948.

72. Kröger, F. A. and Vink, H. J. Imperfections in crystalline solids. In Seitz, F. and Turnbull, D., eds. Solid State Physics. Volume 3. Pp. 307-435. New York, New York, Academic Press. 1956.

73. Eyring, L. and Baenziger, N. C. On the structure and related properties of the oxides of praseodynium. Journal of Applied Physics Supplement 33(1): 428-433. 1962.

74. Miller, A. E. and Daane, A. H. Preparation of a new type nonstoichiometric rare earth oxide. Journal of Inorganic and Nuclear Chemistry 27(9): 1955-1960. 1965.

75. Berard, M. F., Wirkus, C. D., and Wilder, D. R. Diffusion of oxygen in selected monocrystalline rare earth oxides. American Ceramic Society Journal 51(11): 643-647. 1968.

76. Barrett, M. F. and Barry, T. I. Non-stoichiometry in neodynium and europium oxides in relation to their interaction with oxygen and hydrogen. Journal of Inorganic and Nuclear Chemistry 27(7): 1483-1487. 1965.

77. Wagner, C. Galvanic cells with solid electrolytes involving ionic and electronic conduction. International Committee of Electrochemical Thermodynamics and Kinetics (CITCE) Proceedings 7: 361-377. 1957.

78. Bauerle, J. E. Electrical conduction in thoria and thoria-yttria as a function of oxygen pressure. Journal of Chemical Physics 45(11): 4162-4166. 1966.

79. Wimmer, J. M., Bidwell, L. R., and Tallan, N. M. Electrical properties and defect structure of a ($0.13YO_{1.5}$ $0.87ThO_2$) electrolyte. American Ceramic Society Journal 50(4): 198-201. 1967.

80. Wagner, C. The electromotive force of galvanic cells involving phases of locally variable composition. In Delahay, P., ed. Advances in Electrochemistry and Electrochemical Engineering. Volume 4. Pp. 1-46. New York, New York, Interscience Publishers. 1966.

81. Hebb, M. H. Electrical conductivity of silver nitrate. Journal of Chemical Physics 67(1): 185-190. 1952.

82. Furlong, L. R. and Domingues, L. P. Sintering of yttrium oxide. American Ceramic Society Bulletin 45(12): 1051-1054. 1966.

83. Vogel, R. E. and Kempter, C. P. A mathematical technique for the precision determination of lattice parameters. Acta Crystallographica 14(11): 1130-1135. 1961.

84. Coughlin, J. P. Contributions to the data on theoretical metallurgy. XII. Heats and free energies of formation of inorganic oxides. U.S. Bureau of Mines Bulletin 542. 1954.

85. Charette, G. G. and Flengas, S. N. Thermodynamic properties of the oxides of Fe, Ni, Pb, Cu, and Mn by emf measurements. Electrochemical Society Journal 115(8): 796-804. 1968.

86. Steele, B. C. H. High-temperature thermodynamic measurements involving solid electrolyte systems. In Alcock, C. B., ed. Electromotive Force Measurements in High-temperature Systems. Pp. 3-27. New York, New York, American Elsevier Publishing Company, Inc. 1968.

87. Vest, R. W. The electrical conductivity of ceramics; its measurement and interpretation. U.S. Atomic Energy Commission Report ARL-67-0010 [Aerospace Research Laboratories, Wright-Patterson AFB, Ohio]. 1966.

88. Wicks, C. E. and Block, F. E. Thermodynamic properties of 65 elements. U.S. Bureau of Mines Bulletin 605. 1963.

89. Shannon, R. D. and Prewitt, C. T. Effective ionic radii in oxides and fluorides. Acta Crystallographica B25(5): 925-946. 1969.

90. Robert, G., Besson, J., and Deportes, C. Selection d'oxydes refractaires pour piles a combustible a haute temperature. Revue Energie Primaire 2(1): 5-9. 1966.

APPENDICES

Appendix A. Derivation of the Open Circuit Emf Across a Mixed Conductor

Consider a binary oxide scale, M_aO_b, formed on a metal, M, subjected to an oxidizing atmosphere as shown in Figure 25. The most general case of conduction behavior for the scale is assumed; it exhibits significant ionic and electronic conductivity under constant temperature and the prevailing chemical potentials of the metal and gas phase during the oxidation process.

An expression for the open circuit emf of a cell involving phases of locally variable composition may be derived with the aid of irreversible thermodynamics. The equation for the total current assuming a system at constant temperature is:

$$I_T = A \sum_{i=1}^{4} q_i J_i \qquad (1A)$$

where J_i is the flux of the ith component expressed in particles/cm^2 and q_i is the total charge carried by the ith type particle. The index i represents the type of charge carriers as specified in Table 6. A is the cross-sectional area expressed in cm^2.

At any general location x, the flux J_i of the ith type

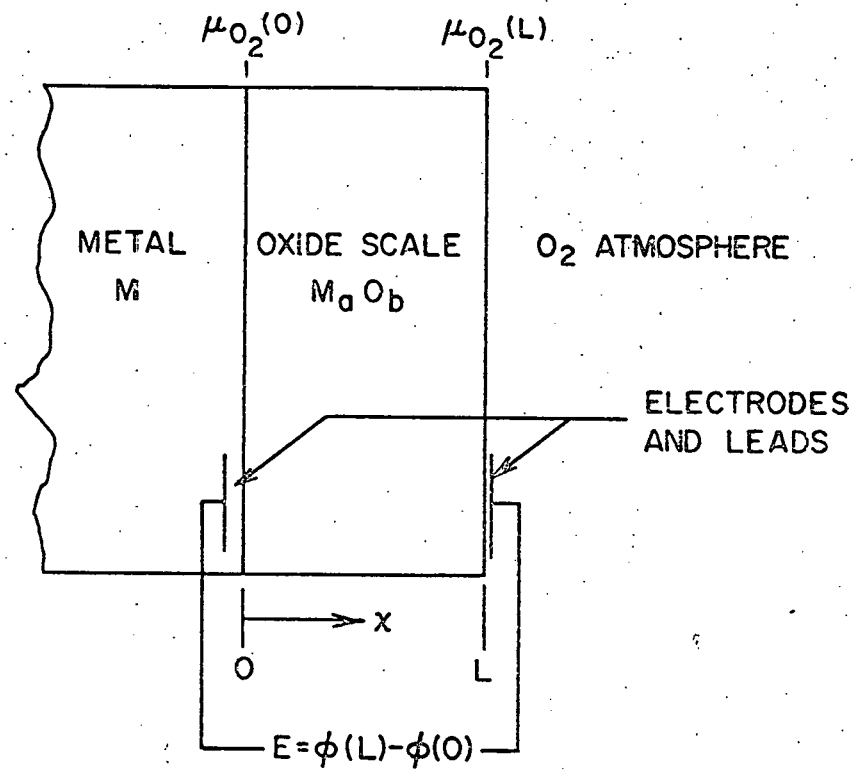

Figure 25. Schematic diagram representing the oxidation of a metal which can be thought of as a galvanic cell with a mixed oxide conductor placed between two unlike reversible electrodes

particle is given by the viscous medium description of diffusional fluxes,

$$J_i = - \frac{c_i B_i}{N} \nabla \eta_i \qquad (2A)$$

where c_i is the concentration of the ith species in particles/cm^3, N is Avagadro's number, B_i is the absolute mobility expressed in particles-cm^2/cal-sec., and η_i is the electrochemical potential and is defined as follows:

$$\eta_i = \mu_i + q_i N \emptyset \qquad (3A)$$

where μ_i is the chemical potential in cal/mole and $\emptyset$ is the electrostatic potential usually expressed in volts. If the term involving the electrostatic potential is divided by the constant 4.186, then the term has the same units as μ_i.

One of the macroscopic variables that can be measured is the electrical conductivity.

$$\sigma_i = - \left[\frac{q_i J_i}{\nabla \emptyset} \right]_{\nabla \mu_i = 0} \qquad (4A)$$

Substitution of Equations 2A and 4A into 1A leads to a new expression for the total current.

$$I_T = - \frac{A}{N} \sum_{i=1}^{4} \frac{\sigma_i}{q_i} \nabla \eta_i \qquad (5A)$$

Since most solid oxide electrolytes derive their unique

property from the presence of a defective anion sublattice, only those equilibria involving the anion lattice will be considered, however defects on the cation lattice can also be accounted for if required.

Table 6. Index notation

Index	Species	Symbol
1	ionized oxygen vacancy	$V_O^{\cdot\cdot}$
2	ionized oxygen interstitial	O_i''
3	electron	$\ominus$
4	hole	$\oplus$

The intrinsic equilibria influencing the defect structure of the mixed conductor are

$$\ominus_e^x \rightleftarrows \ominus^c + \oplus^v \qquad (6A)$$

$$O_o^x \rightleftarrows O_i'' + V_O^{\cdot\cdot} . \qquad (7A)$$

Equation 6A represents an electron in the valence band that has been excited into the conduction band and leaves a resultant positive hole in the valence band. Equation 7A represents the formation of antiFrenkel defect. The incorporation equilibria that control the formation of holes, excess electrons, and anion defects, and allows the crystal to change

stoichiometry are

$$\tfrac{1}{2}O_2 \rightleftarrows O_i'' + \frac{q_2}{q_3}\,\oplus \tag{8A}$$

$$O_o^x \rightleftarrows \tfrac{1}{2}O_2 + V_O^{\cdot\cdot} - \frac{q_1}{q_3}\,\ominus\ . \tag{9A}$$

Equation 8A normally predominates in high oxygen pressure regions, while Equation 9A applies to the low oxygen pressure regions. The above equilibria allow certain electrochemical potentials to be rewritten in terms of other more desirable electrochemical potentials and/or chemical potentials, such as

$$\begin{aligned}
\nabla\eta_4 &= -\nabla\eta_3 \\
\nabla\eta_1 &= -\nabla\eta_2 \\
\nabla\eta_2 &= \tfrac{1}{2}\nabla\mu_{O_2} - \frac{q_2}{q_3}\ \nabla\eta_4 \\
\nabla\eta_1 &= -\tfrac{1}{2}\nabla\mu_{O_2} + \frac{q_1}{q_3}\ \nabla\eta_3\ .
\end{aligned} \tag{10A}$$

Using the results of the equilibrium conditions, Equations 10A can be substituted into Equation 5A to yield the total current at a location x

$$I_T = -\frac{A}{N}\left[\frac{\sigma_{ion}}{q_2}\ \nabla\mu_{O_2} + \frac{\sigma_T}{q_3}\ \nabla\eta_3\right], \tag{11A}$$

where the ionic and total conductivity are defined as

$$\sigma_{ion} = \sigma_1 + \sigma_2$$

$$\sigma_T = \sigma_1 + \sigma_2 + \sigma_3 + \sigma_4 \cdot \qquad (12A)$$

Under open circuit conditions the total current through the mixed conductor is zero. The ionic transference number is defined as the fraction of the total conductivity which results from ionic movement.

$$t_{ion} = \frac{\sigma_{ion}}{\sigma_T} \qquad (13A)$$

Setting Equation 11A equal to zero and inserting the definition given by Equation 13A, the resulting equation is

$$\frac{-t_{ion}}{2q_2/q_3} \nabla \mu_{O_2} = \nabla \eta_3 \cdot \qquad (14A)$$

Considering a unidimensional flow of fluxes between two reversible electrodes on either side of the mixed conductor located at x = 0 and x = L as shown in Figure 25, Equation 14A can now be integrated.

$$\frac{-1}{2q_2/q_3} \int_{\mu_{O_2}(0)}^{\mu_{O_2}(L)} t_{ion}\, d\mu_{O_2} = q_3 N[\phi^{Pt}(L) - \phi^{Pt}(0)] = FE \qquad (15A)$$

where $\phi^{Pt}(L)$ and $\phi^{Pt}(0)$ are the electrostatic potentials in the platinum leads, $\mu_{O_2}(L)$ and $\mu_{O_2}(0)$ are the oxygen chemical potentials at the appropriate interfaces, F is Faraday's constant and in this case is equal to 23,080 cal/volt-mole,

so that the open circuit emf, E, will be given in volts.

Equation 15A assumes that there are no reactions or polarization effects occurring at the electrode/mixed conductor interfaces. Rearrangement of Equation 15A leads to the more common form,

$$E = \frac{-1}{2F\ q_2/q_3} \int_{\mu_{O_2}(O)}^{\mu_{O_2}(L)} t_{ion}\ d\mu_{O_2}. \qquad (16A)$$

From Equation 16A it can be seen that the open circuit emf across the oxide scale of a mixed conductor is sensitive to the amount of current carried by the ions and to the chemical potential gradient of the neutral species across the scale. Equation 16A can be expressed in terms of oxygen partial pressures, which are more measurable quantities.

$$E = \frac{-RT}{2F\ q_2/q_3} \int_{\ln P_{O_2}(O)}^{\ln P_{O_2}(L)} t_{ion}\ d\ \ln\ P_{O_2} \qquad (17A)$$

The above derivation is based on the scaling rate theory as proposed by Wagner (2,80).

Appendix B. Electrical Conductivity Data for Undoped Yttria

Run 1. Air induction Y_2O_3

^oC T	-Logσ $(ohm\text{-}cm)^{-1}$	-Log P_{O_2} (atm)
1006	6.08	6.15
958	6.29	6.68
905	6.54	7.33
852	6.80	8.03
801	7.05	8.78
742	7.33	9.72
691	7.59	10.64
994	6.10	6.27
953	6.29	6.74
902	6.52	7.36
855	6.75	7.98
796	7.05	8.84
746	7.29	9.64
698	7.53	10.50

Run 2. Hot pressed Y_2O_3

1003	6.28	11.6
958	6.44	11.6
913	6.62	11.6
860	6.89	11.6
801	7.09	11.6
697	7.57	11.6

Run 3. Hot pressed Y_2O_3

1001	4.80	0.00
1001	4.90	0.68
1002	5.06	2.00
1002	6.32	9.79
1004	6.27	11.76
1003	6.19	13.78
1006	5.96	15.73

Run 4. Air induction Y_2O_3

991	4.74	0.00
991	4.86	0.68
992	5.21	2.00
992	6.26	9.98
991	4.86	0.68
950	5.07	0.68
907	5.30	0.68
851	5.65	0.68
794	6.02	0.68
744	6.39	0.68
698	6.77	0.68
994	6.23	9.95
951	6.50	10.76
903	6.74	11.73
850	7.00	12.92
801	7.22	14.13
748	7.45	15.55
702	7.65	16.93
997	6.20	9.88
993	6.25	11.96
994	6.25	13.95
993	6.07	15.96
993	4.61	0.00

Run 5. Slip cast Y_2O_3

993	6.10	13.95
994	6.21	11.95
994	6.24	9.94
995	6.20	11.93
995	6.08	13.92
995	5.84	15.93
997	6.08	13.90
997	5.87	15.88

$^{o}C^{T}$	-Logσ $(ohm\text{-}cm)^{-1}$	-Log P_{O_2} (atm)
Run 6. Slip cast Y_2O_3		
992	4.75	0.00
897	5.51	0.00
796	6.39	0.00
701	7.24	0.00
Run 7. Slip cast Y_2O_3		
992	4.94	0.00
896	5.60	0.00
802	6.34	0.00
707	7.15	0.00
995	5.40	2.00
896	6.05	2.00
796	6.74	2.00
701	7.43	2.00
Run 8. Slip cast Y_2O_3		
1002	6.28	10.31
905	6.70	11.89
808	7.25	13.76
708	7.86	16.07
756	7.62	14.89
858	7.09	12.76
953	6.01	11.08
Run 9. Slip cast Y_2O_3		
994	4.76	0.00
894	5.48	0.00
805	6.18	0.00
705	7.02	0.00
756	6.60	0.00
852	5.81	0.00
947	5.09	0.00
995	4.76	0.00

$^{o}C^{T}$	-Logσ $(ohm\text{-}cm)^{-1}$	-Log P_{O_2} (atm)
Run 10. Hot pressed Y_2O_3		
998	6.29	9.87
998	6.27	11.87
998	6.18	13.87
998	6.23	15.87

Appendix C. Open Circuit Emf Data for Undoped Yttria

Cell: Ni,NiO/Y_2O_3/Y,Y_2O_3

T °C	Measured emf (mv)	Thermodynamic emf (mv) (86,84)
993	152	1713
946	162	1717
859	180	1722
807	201	1724
755	214	1728
697	229	1733
1003	173	1712
950	169	1717
902	164	1720
858	168	1724
802	165	1729

Cell: Co,CoO/Y_2O_3/Y,Y_2O_3

T °C	Measured emf (mv)	Thermodynamic emf (mv) (4,84)
1007	26.5	1615
953	36.6	1623
901	44.7	1631

Cell: Ni,NiO/Y_2O_3/Co,CoO

T °C	Measured emf (mv)	Thermodynamic emf (mv) (86,4)
1016	96.8	98.0
1008	90.5	97.5
957	73.5	94.0
905	67.5	90.6
852	72.9	87.0
996	70.9	96.7
953	50.2	93.8
906	47.0	90.6

Cell: $Ni,NiO/Y_2O_3/Co,CoO$ (continued)

T °C	Measured emf (mv)	Thermodynamic emf (mv) (86,4)
849	65.0	86.8
879	75.9	88.8
930	51.9	92.2
972	50.1	95.0
996	56.0	96.7

Cell: $Cu,Cu_2O/Y_2O_3/Ni,NiO$

T °C	Measured emf (mv)	Thermodynamic emf (mv) (36,86)
1006	137.5	258.9
958	166.2	262.2
904	197.8	265.9
852	226.1	269.6
801	248.8	273.2
742	264.3	277.2
691	271.7	280.8
994	144.9	259.7
953	171.0	262.6
902	202.5	266.1
855	226.4	269.3
796	250.6	273.5
746	263.8	276.9
698	268.2	280.3
1016	157.8	258.2
1008	162.3	258.7
957	184.4	262.3
905	216.7	265.9

Appendix D. Electrical Conductivity Data for Yttria Doped Hafnia in Dry Air

T_C	-Log σ $(ohm\text{-}cm)^{-1}$
6 m/o Y_2O_3 - 94 m/o HfO_2	
1001	1.99
996	2.00
971	2.05
948	2.10
925	2.16
901	2.21
876	2.29
849	2.36
826	2.45
798	2.54
8 m/o Y_2O_3 - 92 m/o HfO_2	
1007	1.57
978	1.64
957	1.67
935	1.73
911	1.79
883	1.88
852	1.96
829	2.04
801	2.14
999	1.60
998	1.58
967	1.66
946	1.70
921	1.77
905	1.80
877	1.88
852	1.95
822	2.05
801	2.12

T_C	-Log σ $(ohm\text{-}cm)^{-1}$
10 m/o Y_2O_3 - 90 m/o HfO_2	
997	1.73
996	1.68
963	1.78
948	1.79
928	1.86
906	1.90
879	2.00
852	2.08
826	2.18
801	2.28
994	1.69
950	1.77
906	1.90
858	2.05
799	2.25
12 m/o Y_2O_3 - 88 m/o HfO_2	
998	1.74
948	1.85
907	1.97
855	2.13
797	2.34
14 m/o Y_2O_3 - 86 m/o HfO_2	
996	1.88
999	1.87
967	1.96
946	2.01
926	2.09
904	2.16
880	2.26
856	2.34
830	2.45

14 m/o Y_2O_3 - 86 m/o HfO_2 (continued)

797	2.58
995	1.85
996	1.88
948	1.99
948	2.02
904	2.15
905	2.15
851	2.34
850	2.35
800	2.57

16 m/o Y_2O_3 - 84 m/o HfO_2

994	2.05
996	2.05
948	2.20
951	2.21
906	2.37
907	2.38
854	2.60
854	2.61
801	2.87

18 m/o Y_2O_3 - 82 m/o HfO_2

1001	2.19
977	2.30
954	2.38
930	2.49
910	2.57
885	2.70
856	2.83
830	2.97
801	3.13

20 m/o Y_2O_3 - 80 m/o HfO_2

1002	2.25
973	2.38
952	2.46
923	2.60
907	2.68
877	2.82
852	2.95
826	3.09
798	3.25

Appendix E. Open Circuit Emf Data for 8 m/o Y_2O_3 - 92 m/o HfO_2

Cell: $Cu,Cu_2O/8\text{-}92$ YSH/Ni,NiO

T °C	Measured emf (mv)	Thermodynamic emf (mv) (36,86)
1001	258.0	259.2
1001	257.9	259.2
994	258.3	259.7
994	258.3	259.7
954	261.0	262.5
954	261.3	262.5
896	264.4	266.5
896	264.9	266.5
894	264.8	266.7
894	264.8	266.7
854	266.9	269.5
854	267.2	269.5
806	270.2	272.8
806	269.9	272.8
753	273.8	276.5
753	273.5	276.5
704	276.6	279.9
704	276.2	279.9

Cell: Ni,NiO-8-92 YSH/Co,CoO

T °C	Measured emf (mv)	Thermodynamic emf (mv) (86, 4)
980	93.9	95.6
950	91.3	93.6
895	87.0	89.9
849	83.2	86.8
798	79.4	83.4
745	76.2	79.7
695	69.6	76.4

Cell: $Cu,Cu_2O/8\text{-}92$ YSH/Fe,FeO

T °C	Measured emf (mv)	Thermodynamic emf (mv) (36,86)
1003	543.0	545.7
1000	541.5	545.6
950	542.2	544.1
900	542.0	542.5
851	539.5	540.9
803	538.0	539.4
758	534.3	538.0
707	532.6	536.4

Appendix F. Polarization data for 8 m/o Y_2O_3 - 92 m/o HfO_2

Applied voltage E_A (mv)	Current I_∞ (μA)	Applied voltage E_A (mv)	Current I_∞ (μA)
Run 1P* Cu,Cu_2O/YSH/Au,Pt 1000°C		Run 1P* Cu,Cu_2O/YSH/Au,Pt 850°C	
143	4.6	430	8.70
440	31.5	425	8.40
494	48.5	413	8.00
384	18.3	401	7.45
301	10.4	385	6.90
200	6.1	365	6.22
102	4.0	342	5.65
61	2.5	310	4.93
196	6.4	260	4.17
252	8.4	294	4.50
342	14.6	361	5.90
420	27.0	395	7.05
469	41.7	184	3.22
484	46.1	132	2.95
473	42.7		
464	39.7		
454	36.4		
432	30.2		
406	23.9		
394	21.5		
360	16.4		
321	12.4		
283	9.8		
192	6.7		
332	14.2		
372	19.0		

*$A(cm^2)/L(cm)$ = 7.59(cm) for Run 1P.

Applied voltage E_A (mv)	Current I_∞ (μA)	Applied voltage E_A (mv)	Current I_∞ (μA)
Run 2P** $Cu,Cu_2O/YSH/Au,Pt$ 1000°C		Run 2P** $Cu,Cu_2O/YSH/Au,Pt$ 850°C	
101	3.90	424	7.24
125	4.41	412	6.95
142	4.91	396	6.50
173	5.72	380	6.24
201	6.60	360	5.71
226	7.52	331	5.13
252	8.73	290	4.52
279	10.18	193	3.60
298	11.50	158	3.32
333	14.52	164	3.38
354	16.82	222	3.86
394	22.28	262	4.20
421	26.95	311	4.74
441	31.00	346	5.28
482	40.20	370	5.72
463	36.38	389	6.13
452	33.99	405	6.50
432	29.76		
409	25.72		
372	20.01		

**$A(cm^2)/L(cm) = 7.56(cm)$ for Run 2P.

Appendix G. Lattice Parameter and Density Data for Yttria Doped Hafnia

Composition m/o Y_2O_3	Lattice parameter a_o (Å)	Theoretical density Vacancy model gm/cm^3	Theoretical density Interstitial model gm/cm^3	Apparent density gm/cm^3
2	5.121_5			
4	5.116_2			
5	5.122_1			
6	5.123_3			
8	5.124_2	9.676	10.048	9.555
10	5.128_6	9.490	9.941	9.437
12	5.131_3	9.319	9.846	9.230
14	5.134_0	9.154	9.753	8.916
16	5.139_8	8.979	9.644	8.832
18	5.145_9	8.808	9.535	8.710
20	5.149_7	8.654	9.441	8.524

Appendix H. Coulometric Titration-Open Circuit Emf Cell Data

Cell: $Cu,Cu_2O/CSZ/(Pt)^{/YSH/Cu,Cu_2O}_{/CSZ/Cu,Cu_2O}$ $T = 995^{o}C$

Trial 1

Applied voltage E_A (mv)	Open circuit emf YSH E_H (mv)	Open circuit emf CSZ E_Z (mv)
0	60	60
100	76	75
200	160	148
100	89	88
- 96	- 75	- 74
-204	-175	-173
-295	-259	-258
-395	-343	-342
-492	-422	-417
-602	-522	-504
-198	-173	-172

Trial 2

-113	-122	-137
-100	-116	-131
- 97	-112	-126
-200	-152	-154
-226	-179	-184
-300	-216	-215
-395	-279	-267
-499	-343	-315
-695	-475	-404
-200	-189	-192
- 75	- 84	- 92
195	81	41
400	164	81

ACKNOWLEDGEMENT

The author expresses sincere gratitude to Dr. John W. Patterson for his encouragement, guidance, and helpful discussions during the course of this investigation. A note of thanks is extended to Dr. David R. Wilder for his considerations. The author is indebted to Messrs. J. K. Johnstone and D. W. Stacy for their assistance in performing the x-ray analysis and interpretation of the data. Gratitude is extended Dr. Michael F. Berard for his assistance during the preparation of this dissertation. Thanks are also due Miss Verna Thompson for her patience and suggestions during the typing of this dissertation. The author is also thankful for the patience and support of his wife, Jane, and his children, David and Paul, who also had to endure the existence of a graduate student.